NTNU
Norwegian University of
Science and Technology

The Effect of Donor Doping with Ti^{4+} on the Oxygen Absorption Properties of h-$YMnO_3$

Nikolai Helth Gaukås

Chemical Engineering and Biotechnology
Submission date: June 2016
Supervisor: Sverre Magnus Selbach, IMTE

Norwegian University of Science and Technology
Department of Materials Science and Engineering

Declaration

This master's thesis has been performed at:
Norwegian University of Science and Technology (NTNU)
Department of Materials Science and Engineering
Sem Sælands vei 12 N-7034 Trondheim Norway

Supervisor:

Assoc. Professor Sverre Magnus Selbach	NTNU Trondheim

Co-supervisors:

Professor Tor Grande	NTNU Trondheim
Ph.D. candidate Sandra Skjærvø	NTNU Trondheim
Ph.D. candidate Didrik Småbråten	NTNU Trondheim

M.Sc. candidate:
Nikolai Helth Gaukås

I hereby declare that the work in this study has been conducted honestly and independently, and all used references are denoted.

Trondheim June 15, 2016

Nikolai Helth Gaukås

Preface

This thesis is a result of the subject TMT4900 Materials Technology at the Norwegian University of Science and Technology, performed at the Department of Materials Science and Engineering the spring of 2016. My main supervisor has been Assoc. Professor Sverre Magnus Selbach and my co-supervisors have been Professor Tor Grande, Ph.D. candidate Sandra Skjærvø and Ph.D. candidate Didrik Småbråten. All of the work presented in this paper is performed by the author, unless other is specified. The idea behind the thesis is attributed to Assoc. Professor Sverre Magnus Selbach.

Acknowledgments

The work behind this thesis has been quite comprehensive, and several people deserve recognition for their contributions to the project.

First of all, I would like to give a special thank to my supervisor, Assoc. Professor Sverre Magnus Selbach. His endless support, guidance, patience and knowledge has inspired me throughout the project, making me take those extra steps when reaching for success.

My co-supervisors also deserve acknowledgments: Professor Grande for his helpful input, support and contagious smiles. Ph.D. candidate Skjærvø for her technical guidance and frequent motivational boosts. Ph.D. candidate Småbråten for our valuable discussions regarding the simple and the complex, the important and the trivial.

A huge thanks to the technical staff at the department. Their help regarding the use of equipment was crucial for this thesis. Thanks to Ph.D. candidate Sathya Prakash Singh for helping out with the electrochemical measurements. A loud shout out for Ph.D. candidate Trond Brandvik for always having time to discuss the endless dimensions of my work, or for serving dinner in busy times.

Finally, I would like to thank my family and friends for love and support.

Abstract

In this thesis, the effect of donor doping with Ti^{4+} on the oxygen absorption properties in the hexagonal rare-earth magnanite h−$YMnO_3$ was studied and compared to undoped compounds of the same material class.

Bulk-sized h−$YMnO_3$ and h−$YMn_{0.85}Ti_{0.15}O_3$ (2-17 µm), synthesized through solid state synthesis from binary oxides, and nano-sized h−$YMnO_3$, h−$YMn_{0.85}Ti_{0.15}O_3$ and h−$DyMnO_3$ (18.7-25.5 nm), synthesized through a sol-gel synthesis with citric acid, were analyzed *in situ* in oxidizing and reducing conditions investigating at the changes in structural, gravimetric and electrochemical properties.

The structural changes were measured using HT-XRD, where the change in a and c lattice parameters were analyzed both at varying and constant temperature. The gravimetric changes were measured using TGA, where the change in mass was analyzed during heating and cooling in O_2. The electrochemical changes were analyzed using DC conductivity and Seebeck coefficient measurements during heating and cooling in O_2 and N_2.

The results in the study show a thermal stabilization of interstitial/absorbed oxygen with increasing a parameter and decreasing c parameter. Substitution of Y^{3+} with Dy^{3+} expands both the a and c parameter, increasing the thermal stabilization of O_i by around 100 °C. Donor doping of h−$YMnO_3$ with 15% Ti^{4+} expands the a parameter and contracts the c parameter, increasing the thermal stabilization of O_i by 300 °C for the nano-sized compounds and around 500 °C for the bulk-sized compounds.

Donor doping with 15% Ti^{4+} did not increase the oxygen absorption capacity in h−$YMnO_3$, but the kinetic properties of h−$YMnO_3$ were greatly increased with Ti-doping. The electrochemical measurements showed that it was possible to tune the type of conductivity (n, p) in h−$YMn_{0.85}Ti_{0.15}O_3$ by the thermal and atmospheric history of the material.

Sammendrag

I denne avhandlingen har effekten av donor-doping med Ti^{4+} på oksygenabsorpsjonsegenskapene til den heksagonale sjelden jordart-manganitten h$-YMnO_3$ blitt studert og sammenlignet med udopede forbindelser i samme materialklasse.

Endringene i de strukturelle, gravimetriske og elektrokjemiske egenskapene til h$-YMnO_3$ og h$-YMn_{0.85}Ti_{0.15}O_3$ i bulkstørrelse (2-17 µm), syntetisert med faststoffsyntese fra binære oksider, og h$-YMnO_3$, h$-YMn_{0.85}Ti_{0.15}O_3$ og h$-DyMnO_3$ i nanostørrelse (18.7-25.5 nm), syntetisert gjennom sol-gel-syntese med sitronsyre, ble analysert *in situ* under oksiderende og reduserende forhold.

Endringen i enhetscelleparameterne a og c i materialene målt med høytemperaturrøntgendiffraksjon (HT-XRD), både med varierende og konstant temperatur. Endring i masse under oppvarming og avkjøling i O_2 ble målt med TGA. Endring i likestrømledningsevne og endring i Seebeck koeffisient målt under oppvarmning og avkjøling i O_2 og N_2.

Resultatene i avhandlingen viser en termisk stabilisering av interstitielt/absorbert oksygen ved økende a-parameter og synkende c-parameter. Subtitusjon av Y^{3+} med Dy^{3+} gir en ekspansjon av både a- og c-parameter, og fører til en termisk stabilisasjonsøkning for O_i på rundt 100 °C. Donor-doping av h$-YMnO_3$ med 15% Ti^{4+} gir en ekspansjon av a-parameteren og en kontraksjon av c-parameteren, og fører til en termisk stabilisasjonsøkning for O_i på rundt 300 °C for forbindelene med nanostørrelse og rundt 500 °C for forbindelsene med bulkstørrelse.

Donor-doping av med 15% Ti^{4+} ga ikke en økt kapasitet i oksygenabsorpsjon i h$-YMnO_3$, men kinetikkegenskapene til h$-YMnO_3$ ble kraftig forbedret med Ti-doping. De elektrokjemiske målingene viste at typen ledningsevne (n, p) i h$-YMn_{0.85}Ti_{0.15}O_3$ kan endres med den termiske og atmosfæriske historien til materialet.

List of Abbreviations

Bulk R Bulk-sized h−$RMnO_3$

DC Direct Current

DFT Density Functional Theory

DOS Density of States

h−$RMnO_3$ Hexagonal $RMnO_3$

HT-XRD High Temperature X-Ray Diffraction

Nano R Nano-sized h−$RMnO_3$

o−$RMnO_3$ Orthorhombic $RMnO_3$

SEM Scanning Electron Microscope

TGA Thermogravimetric Analysis

VESTA Visualisation for Electronic ans Structural Analysis (software)

XRD X-Ray Diffraction

Contents

Chapter 1

Introduction

Probably the biggest challenge our modern society face is the quickly escalating climate change. To meet tomorrow's demand for more efficient, more energy saving and less polluting processes, more advanced technology must be implemented in our daily lives. This chapter will point out the main motivations for why a new class of materials for oxygen storage and -conductivity is an important topic in today's society.

1.1 The Big Picture

In their report "The Way Forward" [1] from 2014, the International Energy Agency (IEA) states that 26% of the man-made CO_2 emissions is generated in the industrial sector, 20% in the transport sector and 39% in the power sector. These numbers should not surprise anyone; the world's growing population is demanding more energy and more industrial products delivered at our door steps, and combined these sectors are responsible for 85% of the total man made emission of CO_2. The report also states that the two biggest key actions to reduce the emission of CO_2 are to rise the efficiency in existing sectors (49%) and to reduce the emissions from ineffective coal-fired power generation (21%).

Thus, the challenge today is how to meet the growing demand for energy and at the same time reduce the emission of CO_2. The key factor is increased efficiency by new technology. If one looks at the coal-fired power generation sector, the average power plant has an efficiency of just 33% [2]. This is due to the inefficient technology that most coal-fired power plants utilizes, where the heat from the air-burnt coal is used to produce steam, which in turn is converted to electrical power by a generator. A much more efficient design is combustion of the coal in pure oxygen, the so-called oxy-fuel combustion technology, which leads to less emission and a higher efficiency [3].

The problem with todays oxy-fuel combustion technology, however, is that the oxygen permeable materials used in the membranes for the separation of oxygen from air just are not good enough. The oxygen permeable materials have a low oxygen flux and need high operating temperatures, leading to energy waste and degradation of the materials. This leads to higher costs than a regular coal-fired power plant, and thus the oxy-fuel combustion technology is still not a real challenger to the established and inefficient coal-firing technology [4].

The best motivation for companies' will to change to a greener profile is to find solutions that can economically compete with the alternatives [5]. If one can find technology that is both economically and environmentally superior to the present alternatives, the implementation in society and industry will go naturally. This basic principle is confirmed throughout the last century, and includes for example pesticides in the agricultural section and new refrigerator gases in the appliances industry [6, 7]. If such a break-through can be made in the oxygen storing and -conducting area, the environmentally footprint from coal-combustion, exhaust pollution and simply high-purity oxygen production could revolutionize our every-day CO_2 emissions.

1.2 The Little Stroke

Hexagnoal rare-earth manganites, h$-RMnO_3$ (R = Er, Ho, Y, Dy), have a vast field of functional properties that are interesting in modern technology. Since the late 1990s, the interest for the multiferroic properties of h$-YMnO_3$ has lead to a lot of research on the material, both at Department of Materials Science and Engineering at NTNU [8–15] and in the rest of the world [16–20]. Recently, the excellent oxygen conducting and -storing properties in the hexagonal rare-earth manganites have been recognized, placing them as a serious competitor to the existing materials on the marked [21–24].

Solid oxygen conducting materials are already utilized in membrane technology and for solid oxygen storage, but high operating temperatures is preventing the materials from reaching their enormous potential [4]. The state-of-the-art perovskite materials used today rely on oxygen vacancies as the mobile point defect, which requires operating temperatures around 600-800 °C [25, 26]. In addition to the high energy requirement for a system running at such temperatures, the oxygen conducting materials suffer from various forms of degradation due to mobilization of cations at elevated

temperatures. A new class of oxygen conducting materials that could operate at significantly lower temperatures would form a small paradigm shift within the field, and countless industrial sectors could utilize the benefits from cheap pure-oxygen supply.

The hexagonal rare-earth manganites have shown promising results in terms of chemical absorption of oxygen at temperatures below 500 °C [21, 22, 27]. They are hence an enormous challenger to the oxygen permeable materials on the marked. If the hexagonal rare-earth manganites are as good as the preliminary results show, they could truly revolutionize the way the world produces and stores oxygen. And, they could help mankind overcome the threatening global warming.

1.3 Research Objectives

The primary goal of this study is to investigate the effect of donor doping of hexagonal rare-earth manganites in terms of oxygen absorption. The study will look at synthesis of bulk and nano sized h$-RMnO_3$ powders with and without doping, and characterize these materials' properties at elevated temperatures in oxygen rich and poor atmospheres. The *in situ* measurements performed in this study will investigate the changes in (i) the crystal structure, (ii) the gravimetric properties and (iii) the electrochemical properties as a function of oxygen absorption/desorption.

The observed changes in properties for each material will be compared with the change in properties in the other materials. Based on the observed properties, the study will try to understand *what* effect donor doping with Ti^{4+} has on the thermodynamical and kinetic properties of hexagonal yttrium manganite during oxidation and reduction. The study will also try to answer *why* donor doping with Ti^{4+} has the observed effects, and ultimately try to conclude which material requirements are most important when optimizing the oxygen absorption/desorption performance in hexagonal rare-earth manganites.

Chapter 2

Literature Review on h−$RMnO_3$

The rare-earth manganites are a well-studied class of materials in terms of structural geometries, phase stabilities and multiferroic properties. Their two competing structures, the orthorhombic and the hexagonal crystal structure, are characterized with their 6 folded and 5 folded coordinated Mn^{3+}, respectively. Although both structures exhibit mulitferroic properties in form of ferroelectricity and antiferromagnetism, the hexagonal structures seem to possess no critical thin film thickness [28], making them promising for making multiferroic devices in nano scale.

In recent years, however, the robustness of the hexagonal rare-earth manganites to form stable non-stoichiometric compounds with excess of oxygen or R cation deficiency has been a hot topic. Studies has shown that these structures are stable at δ values of 0.35 [22] and x values of -0.28 [29] in h−$R_{1+x}MnO_{3+\delta}$ at temperatures well below the average operation temperatures of state-of-the-art non-stoichiometric perovskite materials. It is believed that the combination of the spacious crystal structure and the multivalent properties of the manganese ion allow the non-stoichiometry to reach such high values.

2.1 Crystal Structure of h−$RMnO_3$

The ABO_3 perovskite/orthorhombic structure is built up by corner sharing octahedra of oxygen with the B cation centered in the middle, and the A cations located in the cubic holes between the octahedra. The octahedra are corner sharing in all directions of the structure, giving the perovskite structure an isotropic appearance, see Figure 2.1.

Hexagonal $RMnO_3$, however, has a layered crystal structure, built up by alternating

planes of trivalent manganese ions in MnO_5 trigonal bipyramids, and planes of rare-earth trivalent R cations, see Figure 2.1. The trigonal bipyramids are corner sharing in the ab-plane, but not in the c-direction as in the perovskite structure. The ordering in these layers depend on temperature, and thus several symmetries with independent space groups are possible for the h−$RMnO_3$.

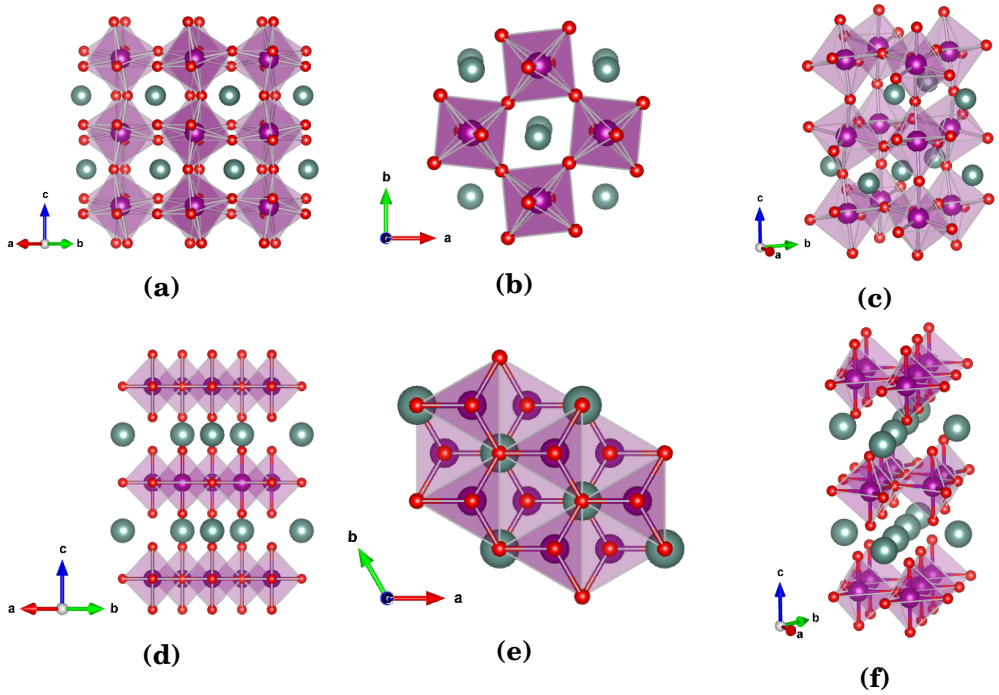

Figure 2.1: Figure (a), (b) and (c) show the perovskite crystal structure with space group $Pnma$, the symmetry found in o−$RMnO_3$. Figure (d), (e) and (f) show the hexagonal crystal structure with space group $P6_3/mmc$, found in h−$RMnO_3$ at high temperatures. While the perovskite structure is built up of all-corner sharing octahedra, the hexagonal structure is a layered structure with 5 folded manganite polyhedra. Worth noting is the difference in spacing in the two structures, where the hexagonal phase has a much open structure compared to the closed perovskite structure. The structures are created with the VESTA software [30] using atomic positions from Gibbs *et al.* [31].

At high temperatures, the trigonal bipyramids align in identical positions and with no tilt in their planes, and the R cations align in perfect planes. This symmetry is found in space group $P6_3/mmc$, and in this state the h−$RMnO_3$ exhibit paraelectricity. Below a certain temperature, the trimerisation temperature, the otherwise planar and ordered layers of MnO_5 trigonal bipyramids and R cations switch into a pattern with lower symmetry. Here, the MnO_5 trigonal bipyramids are ordered in a trimerization tilting pattern, with a tilt $\sim 8°$ with respect to the ab-plane and a tilt $\sim 5°$ to the polar c-axis [32]. The direction of the bipyramids are also consecutive rotated 180° along

the c-axis in each plane. The trivalent rare-earth cations, R^{3+}, are located in two anti-parallel sites along the polar c-axis, i.e. 2/3 in negative direction and 1/3 in positive direction compared to the high temperature sites. This symmetry is found in space group $P6_3cm$, and in this state the h−$RMnO_3$ exhibit ferroelectricity. The trimerisation temperature, which is also the Curie temperature, for h−$YMnO_3$ is reported to be around 1250 K [31], although some studies are suggesting the phase transition to be more complex and to take place at lower or several temperatures [8, 33–35]. A comparison of the high and low symmetry hexagonal phases is given in Figure 2.2.

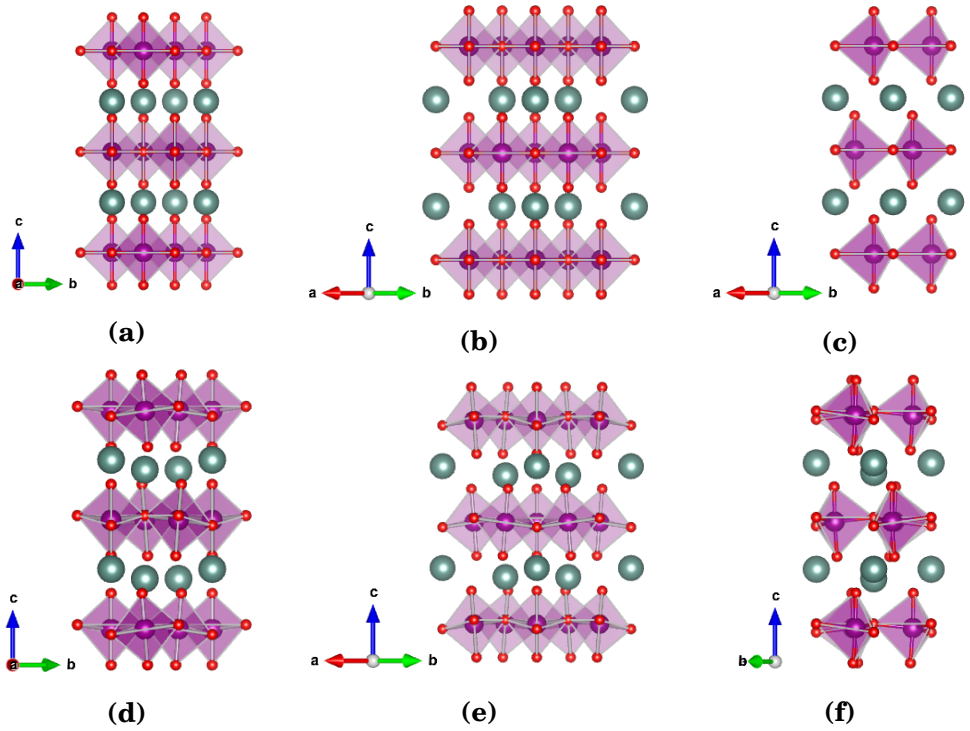

Figure 2.2: Figure (a), (b) and (c) show the high symmetry hexagonal $RMnO_3$ structure with space group $P6_3/mmc$. Figure (d), (e) and (f) show the lower symmetry hexagonal $RMnO_3$ structure with space group $P6_3cm$. Structure (a) and (d) visualize well the identical sites and the two anti-parallel sites for the trivalent R cations, respectively. The trimerization tilting pattern of the MnO_5 trigonal bipyramids, characteristic for the $P6_3cm$ polymorph, are easily recognized in (d), (e) and (f). The red atoms displays O^{2-}, green atoms Y^{3+} and the purple trigonal bipyramids indicates MnO_5 with dark purple Mn^{3+} in the middle. The structures are created with the VESTA software [30] using atomic positions from Gibbs et al [31].

The perovskites have cubic unit cells, while the hexagonal manganites have hexagonal unit cells, see Figure 2.3. This means that the hexagonal manganites can be described by only two lattice parameters, i.e. a and c, unlike the perovskites which are described by three, i.e. a, b and c. Thus, the unit cell volume of h−$RMnO_3$ is only dependent on

these two variables, see Equation 2.1.

$$V = \frac{\sqrt{3}}{2} a^2 c \tag{2.1}$$

The planar spacing, d, in the hexagonal rare-earth manganites between the different crystallographic planes (hkl) is given by the d-spacing equation for hexagonal crystal structures and Bragg's law, see Equation 2.2 and 2.3, respectively.

$$d^{-2} = \frac{4}{3}\left(\frac{h^2 + hk + k^2}{a^2}\right) + \frac{l^2}{c^2} \tag{2.2}$$

$$d = \frac{\lambda}{2\sin\theta} \tag{2.3}$$

λ represents the wavelength of the applied radiation (1.5406 Å in this study), θ the peak positions measured, d the planar spacing in the crystals, h, k and l the Miller indices of the planes the peaks represent and a and c the lattice parameters of the crystal.

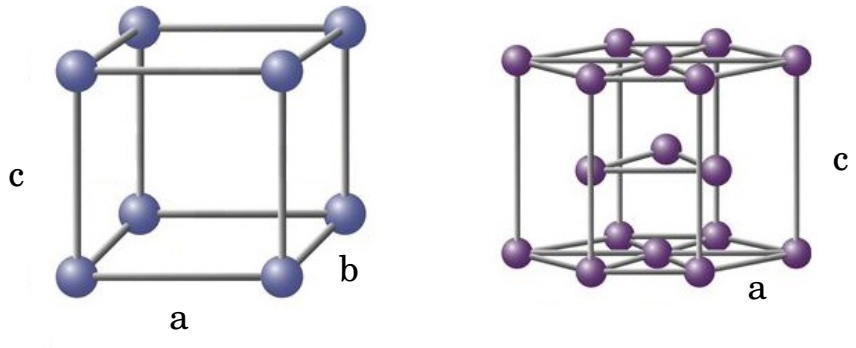

Figure 2.3: Simple illustrations of the cubic (left) and the hexagonal (right) unit cells. The cubic unit cell is described by three lattice parameters, a, b and c. The hexagonal unit cell is described by two lattice parameters, a and b.

2.2 Phase Stability

Reactions that only involves solids are expected to have an entropy close to zero, making the Gibbs energy for the reaction primarily dependent on the enthalpies of formation, see Equation 2.5.

$$\Delta G = \Delta H - T\Delta S \tag{2.4}$$

$$\Delta G_{0\mathrm{K}} = \Delta H_{0\mathrm{K}} \tag{2.5}$$

Yokokawa *et al.* [36] were the first to report the empirical relationship between the enthalpy of formation and the Goldschmidt's tolerance factor, t, for perovskites made by their binary oxides. This relationship is also valid for manganites, and thus the relative stability between the hexagonal structures and the perovskitic, orthorhombic structures depends on the Goldschmidt's tolerance factor [32]. The Goldschmidt's tolerance factor indicates in which structure an ABX_3-composed material will be stable. The value of the tolerance factor is only dependent on the ionic radii of the two cations, A and B, and the anion, here O (oxygen), in the material. The formula for the tolerance factor is given below [37]:

$$t = \frac{r_\mathrm{A} + r_\mathrm{X}}{\sqrt{2}(r_\mathrm{B} + r_\mathrm{X})} \tag{2.6}$$

In Equation 2.6, r_A, r_B and r_X are the ionic radii of ion A, B and X, respectively.

If one uses radii for 4 coordinated anions, 7 coordinated A cations and 5 coordinated B cations, $t \approx 0.855$ serves as threshold limit between the hexagonal phase and the perovskite structures. Values below this indicate that the material will favor the hexagonal phase, while values above indicate favoritism of the perovskites up to a new limit of t = 1.

Structure prediction phase diagrams for the ABX_3 structures can be composed by plotting the size of the A-cation divided by the size of the anion, $\frac{r_A}{r_X}$, with respect to the size

on the B-cation divided by the size of the anion, $\frac{r_B}{r_X}$. Such phase diagrams are helpful to understand the phase stabilities of perovskite composed materials in terms of ionic radii. Figure 2.4 shows the structural regions in the ABO_3 phase diagram.

For the rare-earth manganites, $RMnO_3$, the R cation is the only variable. In the structure prediction diagrams this translates to only have the A-cation as a changing variable, giving only the option to move along a horizontal line across the diagram.

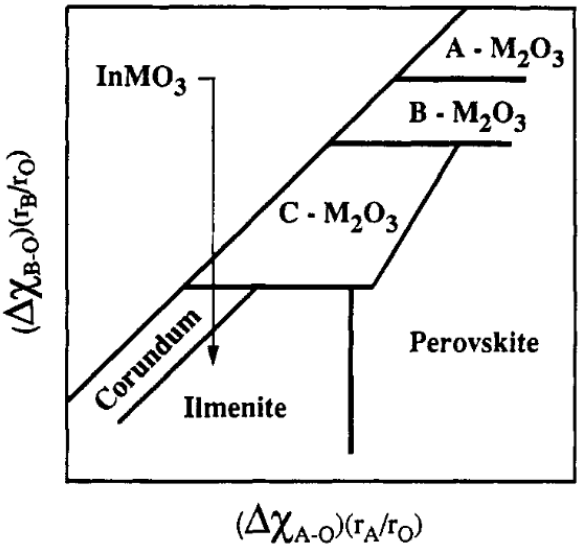

Figure 2.4: The structural regions in ABO_3, illustrating the relationship between $\frac{r_A}{r_O}$ and $\frac{r_B}{r_O}$ and the phases in which the ABO_3 compound result. The hexagonal structures of ABO_3 are located in the ilmenite region, and the vertical line between the ilmenite region and the perovskite region concludes that the transition is only dependent on the radius of the A cation. The figure is taken from Giaquint and zur Loye [38].

As Figure 2.4 shows, the tuning towards the hexagonal phase for the rare-earth manganites is only dependent on the size of the A-cation, i.e. the rare-earth ions. If these are sufficiently small, the tolerance factors, t, will become smaller than the limit of $t \approx 0.855$, and hence the hexagonal phases are favored. In Table 2.1 the tolerance factors for a selection of rare-earth manganites are listed.

From the values of the tolerance factors in Table 2.1, manganites with gandolinium (Gd) and lanthanum (La) are correctly expected to be stable in the perovskite structure [39, 40], while erbium (Er) is correctly expected to form a hexagonal manganite [38]. $RMnO_3$ materials with R = Ho, Y, Dy and Tb are expected to be stable as hexagonal structures based on the tolerance factor criteria with $t \approx 0.855$, but studies has shown that Y and Dy are slightly metastable in the hexagonal phase and that Ho is slightly

Table 2.1: Shannon radii, tolerance factors and stable polymorphs of R cations in $RMnO_3$. The Shannon radius of Ho^{3+} marked with * is an interpolation between the values with coordination number 6 and 8. Note that an enlargement in size of the A cation (R) corresponds to an enlargement of the tolerance factor.

R^{3+}	Shannon radius [Å]	$RMnO_3$	Tolerance factor, t [-]	Stable polymorph
Er^{3+}	0.945	$ErMnO_3$	0.839	Hexagonal
Ho^{3+}	0.958*	$HoMnO_3$	0.843	Hex./meta.orthorh.
Y^{3+}	0.960	$YMnO_3$	0.844	Orthorh./meta.hex.
Dy^{3+}	0.970	$DyMnO_3$	0.848	Orthorh./meta.hex.
Tb^{3+}	0.98	$TbMnO_3$	0.851	Orthorhombic
Gd^{3+}	1.00	$GdMnO_3$	0.859	Orthorhombic
La^{3+}	1.10	$LaMnO_3$	0.894	Orthorhombic

metastable in the perovskite phase [41, 42]. Tb has been shown to be stable in the orthorhombic perovskite phase [40].

The trivalent manganite ions are further stabilized by the crystal-field splitting in the hexagonal phase, see Figure 2.5. Mn^{3+} is a d^4 transition metal, meaning it has 4 valence electrons to fill in the d-orbitals. By placing all the 4 electrons in low-energy orbitals, such as in the hexagonal splitting, the manganite ions are stabilized in a low-energy coordination. In an octahedral crystal splitting, one of the 4 electrons will have to occupy a higher energy state, or pair up with another electron in one of the low-energy orbitals. For manganese ions octahedral complexed by oxygen ions, the crystal field splitting is weak, resulting in a high-spin electron configuration seen in Figure 2.5. This high-spin configuration acquires more energy to sustain than the hexagonal configuration, resulting in a crystal field stabilization for the hexagonal phase.

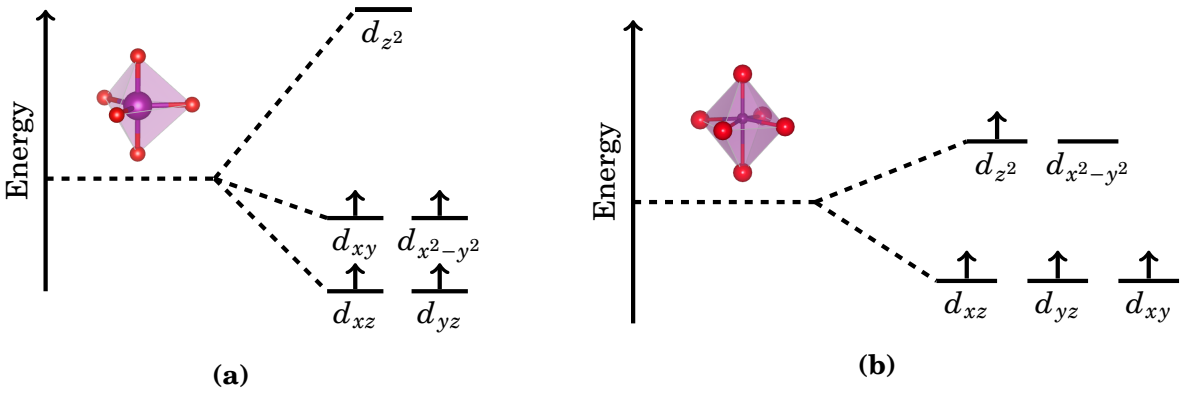

Figure 2.5: (a) The crystal-field splitting for the hexagonal manganite structure, with trigonal bipyramidal coordination of the manganese ions. The d_{z^2} orbital of the manganese ions point directly at the oxygen ligands in the trigonal bipyramids, resulting in a much higher energy than the other orbitals. For the d^4 ion Mn^{3+}, the d_{xy}, $d_{x^2-y^2}$, d_{xz} and d_{yz} orbitals are occupied by 1 electron each, whereas the d_{z^2} orbital is empty. (b) The crystal-field splitting for the perovskite structure, with octahedral coordination of the manganese ions in a weak field, giving a high-spin configuration of the electrons. Mn^{3+} is energetically more stable in the hexagonal crystal splitting due to electrons being in lower energy states.

2.3 Defect Chemistry and Non-Stoichiometry

As mentioned, the hexagonal rare-earth manganites are extremely robust in terms of R-cation deficiency and excess of oxygen. The large non-stoichiometries is obtained by high concentrations of point defects in the materials, and the manganese ions play a crucial role as charge stabilizers in the materials as they can change oxidation state, see Equation 2.7 and 2.8.

$$Mn_{Mn}^{x} + e^{-} \rightarrow Mn_{Mn}^{'} \tag{2.7}$$

$$Mn_{Mn}^{x} + h^{\bullet} \rightarrow Mn_{Mn}^{\bullet} \tag{2.8}$$

2.3.1 Point Defects and Non-stoichiometry

In crystal chemistry, point defects are the simplest form of defects present in a crystal structure of a material. In pure crystals there are two types of point defects; (i) vacant atom sites, vacancies, or (ii) interstitial atoms occupying lattice sites which are normally not occupied in the crystal, interstitials. A visualization of the two types of point defects are given in Figure 2.6. Such defects in pure materials are called intrinsic defects, and they always appear in couples.

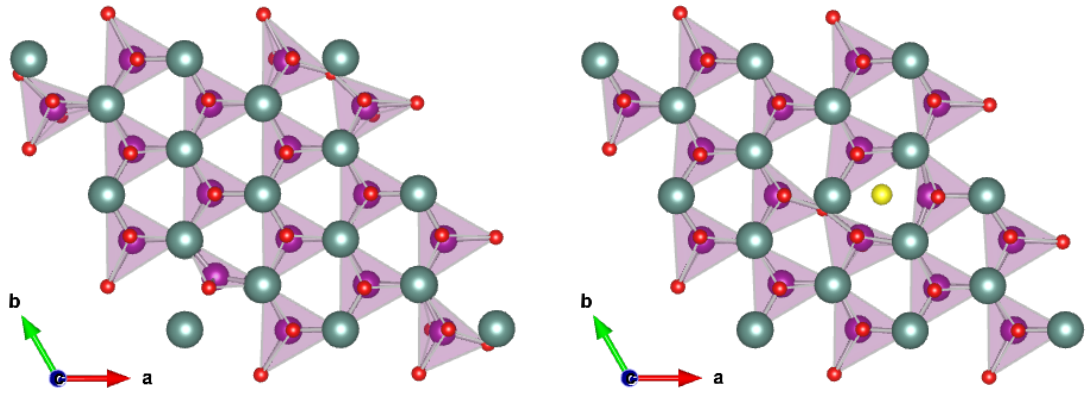

(a) Vacant oxygen. **(b)** Interstitial oxygen.

Figure 2.6: (a) Crystal structure of h−$RMnO_3$ with a vacant oxygen site in the bottom left corner. (b) Crystal structure of h−$RMnO_3$ with an interstitial oxygen marked in yellow. The structures are created with the VESTA software [30].

In Kröger-Vink notations, vacancies are noted as a "V", followed by the chemical symbol of the atom that used to be present in the site in subscript. Bullets or primes are used in superscript to represent a positive or negative formal charge of the vacancy compared to the charge of the ion that used to be present on the site, respectively. For interstitials, the off-placed ions are noted with their chemical symbol followed by an "i" in subscript and the same charge notations as the vacancies. Thus, $V_O^{\bullet\bullet}$ represents a vacancy on an oxygen site with formal charge +2, and O_i'' represents an interstitial oxygen ion in the crystal structure with formal charge -2. [43]

The two most basic types of intrinsic defects are the Schottky defects and the Frenkel defects. A Schottky defect is characterized as a vacancy of anions and cations in a crystal, equivalent to removing a stoichiometric couple of anions and cations from their sites. A Frenkel/anti-Frenkel defect is characterized as an cation/anion on an interstitial site plus an cation/anion vacancy. This is equivalent to removing a cation or anion

from its site and putting it on an interstitial site. Both types of defects preserves the overall stoichiometry in the material. [44]

A third type of intrinsic defects is non-stoichiometry. Non-stoichiometry in a material must be charge compensated either by electronic or ionic defects. In pure hexagonal manganites one can obtain oxygen or R-cation non-stoichiometry by oxidizing or reducing the manganese ions, respectively. An example of oxygen excess non-stoichiometry, i.e. an ionic defect, is given in Equation 2.9 and 2.10.

$$RMnO_3 + \frac{\delta}{2}O_2 \rightarrow RMnO_{3+\delta} \tag{2.9}$$

$$2\delta Mn^{x}_{Mn} + \frac{\delta}{2}O_2 \rightarrow 2\delta Mn^{\bullet}_{Mn} + \delta O^{''}_{i} \tag{2.10}$$

In oxidizing conditions, where the partial pressure of oxygen is high, the hexagonal manganites can chemically absorb oxygen ions as interstitial point defects as described above. In reducing conditions, where the partial pressure of oxygen is low, the hexagonal manganites can reverse this effect and thus release oxygen gas and produce vacancies, see Equation 2.11 and 2.12.

$$RMnO_3 \rightarrow RMnO_{3-\delta} + \frac{\delta}{2}O_2 \tag{2.11}$$

$$2\delta Mn^{x}_{Mn} + \delta O^{x}_{O} \rightarrow 2\delta Mn^{'}_{Mn} + V^{\bullet\bullet}_{O} + \frac{\delta}{2}O_2 \tag{2.12}$$

Both the forward and reverse effect are reversible and rely on temperature, meaning that by heating and cooling the material in an oxygen rich atmosphere, the material can "breathe". In contrast to most oxygen absorbing solids, the formation of oxygen point defects in h−$RMnO_3$ is entropy controlled, not enthalpy controlled. At elevated

temperatures the oxygen vacancies or interstitials have sufficient energy to escape the structure, but at lower temperatures the oxygen point defects are locked in the material, unable to leave. An illustration of this is given in Figure 2.7. Compared to the enthalpy controlled materials, which need a sufficient temperature to overcome the enthalpy barrier of the point defect formation, the entropy controlled h$-RMnO_3$ function at drastically lower temperatures outside of the enthalpy regime. In this way the hexagonal manganites can operate at much lower temperatures than the perovskite oxygen permeable membranes on the marked today.

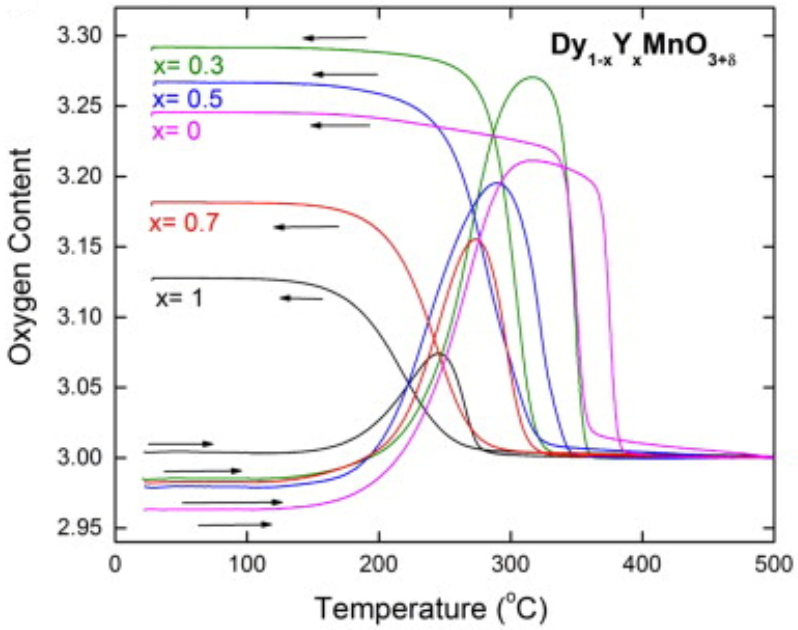

Figure 2.7: Oxygen content in different hexagonal rare-earth manganites of $Dy_{1-x}Y_xMnO_{3+\delta}$ as a function of temperature. The figure illustrates both heating and cooling in O_2, measured with a temperature rate of 0.1 °C min^{-1}. The figure is reprinted from Abughayada *et. al* [23].

2.3.2 Kinetics of Point Defect Implementation

The implementation of point defects from gaseous species is a complex process including multiple steps. Incorporation of interstitial oxygen, as in Equation 2.9, or incorporation of oxygen vacancies, as in Equation 2.11, into the hexagonal rare-earth manganites both involves a reaction where a solid interacts with the surrounding atmosphere. In this case, oxygen needs to enter or leave the structure, respectively.

If one looks at the incorporation of oxygen interstitials, following Equation 2.9, the oxygen molecules need to diffuse to the material surface, undergo a surface exchange, and then react with the material and diffuse into the particle. For generation of vacant oxygen sites, the mechanism is more or less reversed, relaying on the same steps.

Preliminary results from studies done at the department suggests that the adsorption and dissociation of oxygen is the rate determining step, scaling linearly with the crystallite size of the materials, see Equation 2.13 [9].

$$t = \frac{\rho_c R_0^2 \phi_c}{6 D_e C_{0,O_2}} \tag{2.13}$$

In Equation 2.13, t represents the time needed for oxygen to react with a spherical particle of size R_0. ρ_c is the molar density of non-porous h−$RMnO_3$, ϕ_c is the volume fraction of h−$RMnO_3$, C_{0,O_2} is the initial oxygen concentration and D_e is the effective diffusion. The equation is based on the shrinking core model, assuming equal sized particles of size R_0.

In general, the diffusion coefficient's dependence of temperature can be described by the Arrhenius equation, see Equation 2.14.

$$D_e = D_0 \exp \frac{-E_a}{k_B T} \tag{2.14}$$

Here, D_0 is a constant term referred to as the pre-exponential factor, E_a is the activation energy for diffusion, k_B is the Boltzmann constant and T is the temperature. By taking the logarithms of both sides of this equation, one obtains Equation 2.15:

$$\ln D_e = \ln D_0 - \frac{E_a}{k_B T} \tag{2.15}$$

This equation can further be rewritten to refer time, t, by subtracting $\ln D_0$ on both sides, obtaining Equation 2.16:

$$\ln \frac{1}{t} = C - \frac{E_a}{k_B T} \tag{2.16}$$

Here, C is a constant. Based on Equation 2.16, the activation energy, E_a, for diffusion can be determined from the gradient of a plot of $\ln \frac{1}{t}$ versus $1/T$, a so-called Arrhenius plot. [45]

2.3.3 Heterovalent Doping

For h−$RMnO_3$, heterovalent doping on both A and B site is possible [46]. Which of the sites the dopants occupies is simply determined by their ionic radii, since the size of the dopant and the replaced ion needs to be fairly similar. In the hexagonal rare-earth manganites the R-cation has usually a Shannon radius of 0.94 Å to 0.96 Å, while the trivalent manganese ions have a Shannon radius of 0.58 Å.

Doping could help elevate the point defect concentration limit in the hexagonal rare-earth manganites. Although the materials are quite robust towards non-stoichiometry, the structures can only tolerate so-much before a oxidation/reduction concentration limit for the manganese ions is reached. For excess of oxygen in h−$DyMnO_{3+\delta}$ and h−$YMnO_{3+\delta}$, values of $\delta = 0.35$ and $\delta = 0.24$, respectively, have been reported [21–23]. However, preliminary calculations at the department suggests $\delta = 0.333$ to be a theoretical limit of the structures [47]. A theory is that doping can elevate the structural tolerance to higher degrees of non-stoichiometry towards the theoretical limit, especially for h−$YMnO_3$.

To promote charge stabilization for energy stabilization and higher point defect concentrations, the dopants need to act as sources of electron donors or acceptors. Since both the R-cation and the manganese ions in the hexagonal manganites initially are trivalent ions, the acceptor dopants will have to be divalent to be able to stabilize the introduction of positive charges to the structure, such as oxygen vacancies. In the same way the donor dopants need to be tetravalent to be able to stabilize the introduction of negative charges to the structure. Acceptor dopants will favor stabilization of oxygen vacancies in reducing conditions, while donor dopants will favor stabilization of interstitial oxygen in oxidizing conditions.

Examples of donor and acceptor dopant on A and B sites in h−$RMnO_3$ are given in the Kröger-Vink equations below, see Equation 2.17-2.24. Note that doping can either promote point defects, i.e. interstitial oxygen or oxygen vacancies, or promote reduction/oxidization of manganese ions, depending on the partial pressure of oxygen, p_{O_2}.

Donor doping in low p_{O_2}:

$$ZrO_2 + \frac{1}{2}Mn_2O_3 \xrightarrow{h-RMnO_3} Zr_R^{\bullet} + Mn_{Mn}^{'} + 3O_O^x + \frac{1}{4}O_{2(g)} \tag{2.17}$$

$$TiO_2 + \frac{1}{2}Mn_2O_3 \xrightarrow{h-RMnO_3} Ti_{Mn}^{\bullet} + Mn_{Mn}^{'} + 3O_O^x + \frac{1}{4}O_{2(g)} \tag{2.18}$$

Donor doping in high p_{O_2}:

$$ZrO_2 + \frac{1}{2}Mn_2O_3 \xrightarrow{h-RMnO_3} Zr_R^{\bullet} + Mn_{Mn}^x + 3O_O^x + \frac{1}{2}O_i^{''} \tag{2.19}$$

$$TiO_2 + \frac{1}{2}R_2O_3 \xrightarrow{h-RMnO_3} R_R^x + Ti_{Mn}^{\bullet} + 3O_O^x + \frac{1}{2}O_i^{''} \tag{2.20}$$

Acceptor doping in high p_{O_2}:

$$CaO + \frac{1}{2}Mn_2O_3 + \frac{1}{4}O_{2(g)} \xrightarrow{h-RMnO_3} Ca_R^{'} + Mn_{Mn}^{\bullet} + 3O_O^x \tag{2.21}$$

$$ZnO + \frac{1}{2}Mn_2O_3 + \frac{1}{4}O_{2(g)} \xrightarrow{h-RMnO_3} Zn_{Mn}^{'} + Mn_{Mn}^{\bullet} + 3O_O^x \tag{2.22}$$

Acceptor doping in low p_{O_2}:

$$CaO + \frac{1}{2}Mn_2O_3 \xrightarrow{h-RMnO_3} Ca_R^{'} + Mn_{Mn}^{x} + \frac{5}{2}O_O^{x} + \frac{1}{2}V_O^{\bullet\bullet} \tag{2.23}$$

$$ZnO + \frac{1}{2}R_2O_3 \xrightarrow{h-RMnO_3} R_R^{x} + Zn_{Mn}^{'} + \frac{5}{2}O_O^{x} + \frac{1}{2}V_O^{\bullet\bullet} \tag{2.24}$$

According to Equation 2.17-2.24, donor doping will favor interstitial oxygen, $O_i^{''}$, in oxidizing conditions and acceptor doping will favor oxygen vacancies, $V_O^{\bullet\bullet}$, in reducing conditions. Note that $[O_i^{''}] > \frac{1}{2}[Zr/Ti_{R/Mn}^{\bullet}]$ and $[V_O^{\bullet\bullet}] > \frac{1}{2}[Ca/Zn_{R/Mn}^{'}]$ due to further oxidization and reduction of Mn^{3+}, respectively, forming more $O_i^{''}$ and $V_O^{\bullet\bullet}$.

2.4 Thermal and Chemical Expansion/Contraction of Solids

Upon heating, a solid usually expands in volume. The effect is due to increased movement of the atoms in the crystal lattice, causing a greater average atom separation. This is called thermal expansion, and is linear in terms of temperature. As the volume increases, the lattice parameters change proportionally, i.e. isotropic, or disproportionately, i.e. anisotropic. For crystals with high symmetry, one usually observe an isotropic expansion of the lattice parameters, while for less symmetric structures the change is anisotropic [45]. The latter is the case for the hexagonal rare-earth manganites [8, 48], where the a and c parameters change at different rates upon heating of the material, see Figure 2.8. The linear thermal expansion coefficient, α_l, can be calculated from Equation 2.25 [43].

$$\alpha_l = \frac{1}{l_0} \cdot \frac{l - l_0}{T - T_0} \tag{2.25}$$

Here, l_0 is the initial length at the initial temperature, T_0, and l is the new length at the new temperature, T.

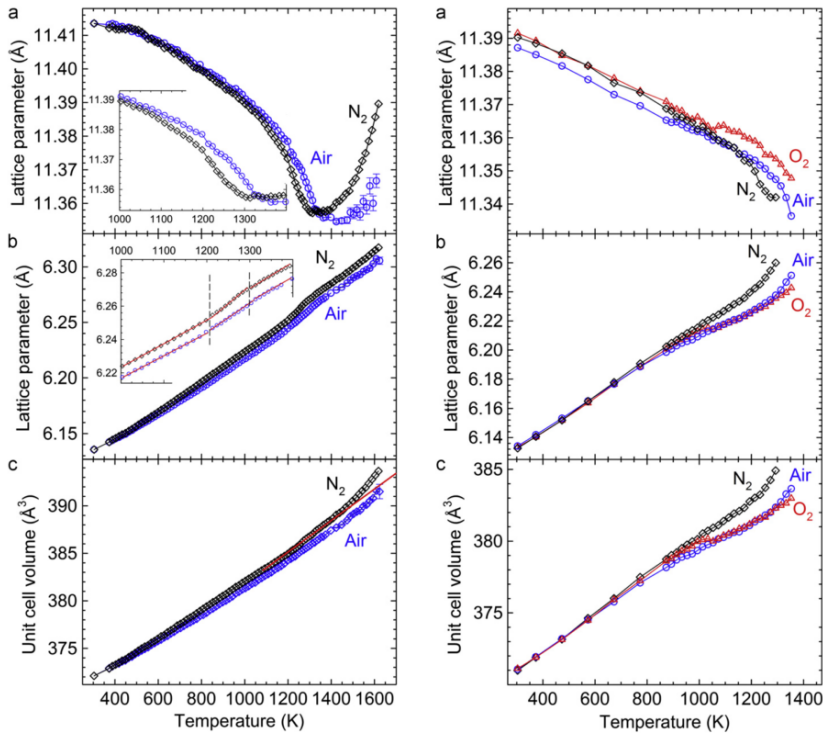

Figure 2.8: Changes in the unit cell parameters and unit cell volume in different atmospheres for h−$YMnO_3$ and h−$HoMnO_3$. (a) shows the changes for unit cell parameter c, (b) shows for lattice parameter a, and (c) shows the changes in unit cell volume. The figure is reprinted from Selbach *et al.* [8].

In addition to thermal expansion, a solid can increase or decrease in volume due to incorporation of other elements or chemical reactions in the material. This is called chemical expansion/contraction, and unlike thermal expansion the effect is no-linear. Chemical expansion or contraction also only appears after a given temperature, due to dependence on a certain activation energy to initiate the chemical reaction. Figure 2.9 illustrates thermal expansion and chemical expansion and contraction as a function of temperature.

Chemical contraction can be observed in h−$RMnO_3$ and is due to oxidization of manganese ions caused by absorption of oxygen ions in the structures. The chemical contraction is dependent on a surrounding partial pressure of oxygen [22]. Thus, chemical expansion is not possible in h−$RMnO_3$ during heat treatment in inert atmosphere.

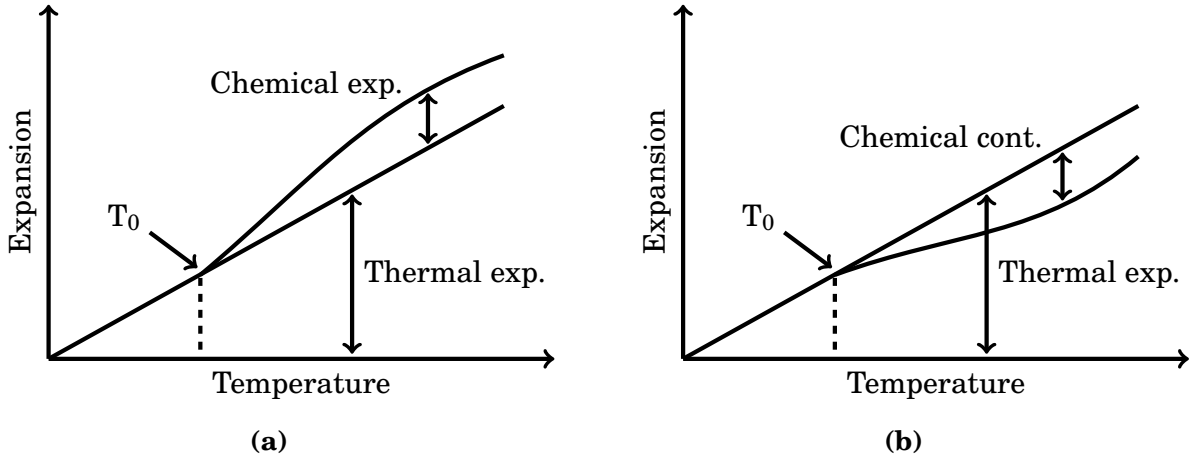

Figure 2.9: (a) Thermal expansion and chemical expansion of a solid. (b) Thermal expansion and chemical contraction of a solid. T_0 marks the onset temperature for chemical expansion/contraction.

During the reaction with oxygen, the c parameter decreases and the a parameter increases in the structure. This is due to a contraction of the MnO_5 bipyramids along the c-axis to compensate the size reduction of the oxidized manganese ions [21]. This is believed to result in an overall decrease in unit cell volume [21, 23], V, despite the squared dependence on the a parameter, see Equation 2.1.

Measuring chemical expansion in h$-RMnO_3$ can be done with HT-XRD. By choosing two peaks where at least one of them only represents one of the lattice parameters, the lattice parameters can be calculated from the change in peak position. The position of a peak is expected to increase if the lattice parameter decreases, and vice versa. This can be seen from Equation 2.2 and 2.3.

Rapid changes in unit cell volume due to anisotropic expansion can lead to microcracking on the grain boundaries, and thus destroy the mechanical and physical properties of a hexagonal manganite material. Microcracking is observed on h$-YMnO_3$ in the temperature region 600-1000 °C. This temperature range is beyond the temperature interval of chemical expansion in most hexagonal manganites, and originates in the phase transition from the low temperature $P6_3cm$ phase to the high temperature $P6_3/mmc$ phase. Lowering the crystallite size below a critical value or use dopants to stabilize the structure, e.g. Ti^{4+}, has proved to reduce the risk of microcracking [49].

2.5 Electrical Conductivity in h−$RMnO_3$

The last 20 years, a lot of studies have investigated the electrical conductivity in hexagonal $RMnO_3$ [8, 50–58]. The mechanisms are complex, since both thermal and atmospheric history affect the conductivity, and explanations for the observed values during *in situ* measurements vary.

Electrical conductivity, σ, in a solid is dependent on the number of current carriers, n or p, their charge, e, and their mobility, μ, see Equation 2.26 [43]. For semiconductors, both the number of current carriers and their mobility is dependent on temperature [45]. In short, both the number of charge carriers and their mobility will increase upon increasing temperature.

$$\sigma = ne\mu_e + pe\mu_h \tag{2.26}$$

In Equation 2.26, n and p represent the number of electrons and holes, respectively. μ_e and μ_h are the mobility of the electrons and the holes, respectively. The relationship between the concentration of n- and p-type carriers and the oxygen partial pressure can be illustrated with Brouwer diagrams, see Figure 2.10, based on the principle of net charge neutrality, see Equation 2.27. Since the net charge in a material is always neutral, the majority charge carrier will be the charged specie with the highest mobility, μ.

$$2[V_O^{\bullet\bullet}] + [D^{\bullet}] + p^{\bullet} = 2[O_i^{''}] + [A^{'}] + n^{'} \tag{2.27}$$

The pure hexagonal rare-earth manganites in this study are intrinsic semiconductors with band gaps around 1.6 eV [59, 60]. Thus, the electrical conductivity is expected to increase with temperature due to excitation of electrons from the valence band to the conduction band, increasing the number of charge carriers in the materials. In addition to the effect of excitation of electrons in the hexagonal manganites, the implementation of point defects will also affect the conductivity. As the manganites are

oxidized, $Mn_{Mn}^{\bullet}$ will contribute to the number of charge carriers, and hence increase the conductivity in form of p charge carriers.

The Seebeck coefficient, Σ, of a material is a measure of the magnitude of an induced thermoelectric voltage in response to a temperature difference across that material. The Seebeck coefficient usually has a value of $10\,\mu V\,K^{-1}$ for metals and $200\,\mu V\,K^{-1}$ for semiconductors [45], inversely depending on the conductivity. The sign of the Seebeck coefficient in semiconductors reveal what are the major charge carriers in the material: with positive holes as the majority charge carriers, the Seebeck coefficient will be positive. If the negative charge carriers' mobility exceed the mobility of the positive charge carriers, e.g. by having a larger concentration of e^- than h^+, the Seebeck coefficient in the material will go from a positive to a negative value [45]. The first is the case for undoped semiconductors, e.g. h−$YMnO_3$ with $Mn_{Mn}^{\bullet}$ as the major charge carrier. The latter is the case for donor doped semiconductors, e.g. $YMn_{0.85}Ti_{0.15}O_3$ without interstitial oxygen where electrons (from $Mn_{Mn}^{'} = Mn^{3+} + e^-$) is the major charge carrier.

Since the oxidation is limited to a certain temperature, this effect will only contribute in that temperature region. At isothermal conditions in the oxidation regime it is expected that the conductivity is largely affected by oxygen absorption and desorption in the manganites as one switches between oxidizing and reducing atmospheres [54, 56].

On top of this, donor doping with Ti^{4+} might affect the conductivity as the manganites go from intrinsic to extrinsic semiconductors. However, it is not reported if the electronic states of the $3d$ orbitals in Ti^{4+} are close enough to the Fermi levels of the manganites to affect the conductivity.

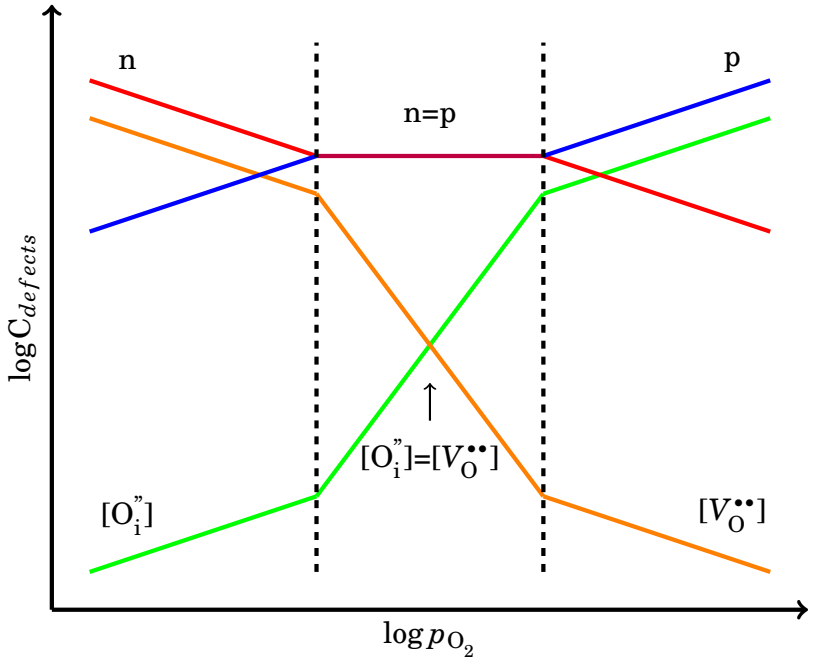

Figure 2.10: A typical Brouwer diagram where electronic defects, n and p, are dominating the ionic defects, O_i'' and $V_O^{\bullet\bullet}$. At low partial pressures of oxygen the material is an n-type conductor, while at high partial pressures it is a p-type conductor. When reduced, the h−$RMnO_3$ are expected to be n-type semiconductors. When oxidized, the h−$RMnO_3$ are expected to be p-type semiconductors.

2.6 Synthesis Methods

There are numerous ways to synthesize ceramic oxides, all with different benefits and degrees of complexity. The hexagonal rare-earth manganites are fairly easy to prepare by controlling the crystallization temperature of their precursor powders. Besides precise stoichiometry and phase purity, size control is the most important factor when investigating the hexagonal manganites during this work. Thus, the two synthesis methods used in this work were chosen based on size control of the final product and to keep the syntheses as simple as possible.

The preparation of bulk-sized powder, i.e. crystallites larger than 1 µm, of h−$RMnO_3$ was conducted using solid state synthesis. This includes mixing and mortaring of stoichiometric amounts of binary oxides, pressing the blended powders into dense pellets and then firing these at temperatures high enough to obtain cation diffusivity.

The preparation of nano crystalline powder was conducted using a sol-gel synthesis with citric acid. This includes dissolving of cations in a solution with gelling agents, boiling down the solution to a gel, drying the gel, calcining the gel to a raw powder, and then annealing the raw powder to promote nucleation of nano-sized crystals.

Above a certain firing temperature, the crystallite growth becomes kinetically dependent for both of the synthesis routes. Thus, by varying the firing time or by introducing an additional heat treatment segment in the synthesis, the crystallite size can be tuned. This is especially important for the nano crystalline powders, as the bulk powders are ground to a certain size after preparation anyways. [61]

Chapter 3

Experimental Work

The experimental work conducted in this thesis includes synthesis of hexagonal rare-earth manganites with different crystallite sizes and with different dopants, and structural, electric and gravimetric analyses of aforementioned substances at elevated temperatures and in various atmospheres.

3.1 Synthesis of h−$RMnO_3$

The hexagonal rare-earth manganites studied in this thesis were prepared by solid state synthesis and sol-gel synthesis. A complete list of all the chemicals used in the study is given in Table 3.1.

Table 3.1: List with information of all the chemicals used to prepare the materials in this study.

Chemical	Molecular formula	Purity	Manufactory
Citric acid	$C_6H_8O_7$		Sigma-Aldrich
Dysprosium(III) acetate	$Dy(CH_3COO)_3 \cdot xH_2O$	≥99.9 wt%	Sigma-Aldrich
Ethylene glycol	$C_4H_6O_2$	99 vol%	Merck
Manganese(II) carbonate	$MnCO_3 \cdot xH_2O$	≥99.9 wt%	Sigma-Aldrich
Manganese(III) oxide	Mn_2O_3	99 wt%	Aldrich
Titanium(IV) isopropoxide	$Ti(OCH(CH_3)_2)_4$	97 wt%	Sigma-Aldrich
Titanium(IV) oxide	TiO_2 (anatase)	99.8 wt%	Aldrich
Yttrium(III) acetate	$Y(CH_3COO)_3 \cdot xH_2O$	99.9 wt%	Sigma-Aldrich
Yttrium(III) oxide	Y_2O_3	99.99 wt%	Aldrich

3.1.1 Solid State Synthesis

Bulk powder of hexagonal yttrium manganites and 15% Ti-doped yttrium manganite were prepared by solid state synthesis. A list of all the samples and their precursors is given in Table 3.2.

Table 3.2: List of bulk powders prepared in this study with their precursors.

Materials	Precursors	Doping
h−$YMnO_3$	Y_2O_3, Mn_2O_3	-
h−$YMn_{0.85}Ti_{0.15}O_3$	Y_2O_3, Mn_2O_3, TiO_2	Donor, B site

In the solid state synthesis, binary oxides of the cations in the two manganites were mortared together and pressed into pellets with diameter 15 mm and height 20 mm. The pellets were then sintered in air at 1300 °C for 12 hours, crushed and mortared into a fine powder. Figure 3.1 shows the temperature program used during the solid state synthesis.

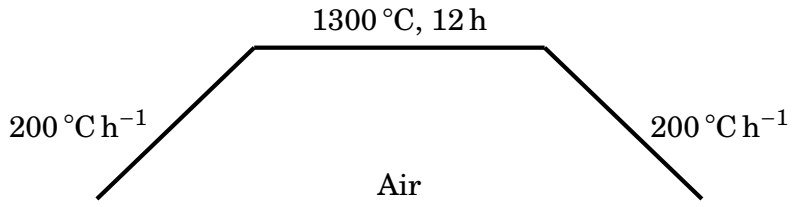

Figure 3.1: The heat treatment program used in the solid state synthesis of h−$RMnO_3$. The samples were heat treated at 1300 °C for 12 hours.

3.1.2 Sol-gel Synthesis

Nano-sized powder of three hexagonal rare-earth manganites with Y and Dy as R-cations were prepared by a sol-gel synthesis with citric acid and ethylene glycol. A complete list of the samples and their precursors is given in Table 3.3. Three of the nano powders were prepared by other master students at the department, i.e. Østmoe [9] and Hoggen [15]. The 150 nm h−$YMnO_3$ was prepared by Bergum [32] with a maleic acid sol-gel synthesis, see Appendix A.

The cation precursors were individually dissolved in distilled water with citric acid, except the Ti-precursor which was added after the blending of the Y^{3+} and Mn^{2+} solutions. The ratio between cation concentration and citric acid is given in Table 3.4.

Table 3.3: List of all nano powders used in this study with their cation precursors. Data for h−$YMnO_3$ and h−$DyMnO_3$ are taken from Østmoe [9], and data for h−$YMn_{0.85}Ti_{0.15}O_3$ are taken from Hoggen [15].

h−$RMn_{x-1}Ti_xO_3$	Precursors	Doping
h−$YMnO_3$	$Y(CH_3COO)_3$, $MnCO_3 \cdot xH_2O$	-
h−$YMn_{0.85}Ti_{0.15}O_3$	$Y(CH_3COO)_3 \cdot xH_2O$, $MnCO_3 \cdot 4H_2O$, $Ti(OCH(CH_3)_2)_4$	Donor, B site
h−$DyMnO_3$	$Dy(CH_3COO)_3 \cdot xH_2O$, $MnCO_3 \cdot xH_2O$	-

Table 3.4: List of ratios of cation precursors versus citric acid in sol-gel synthesis done by other students at the department. Data for h−$YMnO_3$ and h−$DyMnO_3$ are taken from Østmoe [9], and data for h−$YMn_{0.85}Ti_{0.15}O_3$ are taken from Hoggen [15].

h−$RMn_{1-x}Ti_xO_3$	Ratio R:citric acid	Ratio Mn:citric acid
h−$YMnO_3$	1:15	1:22
h−$YMn_{0.85}Ti_{0.15}O_3$	1:15	1:22
h−$DyMnO_3$	1:35	1:22

The solutions with all the cation precursors were then added ethylene glycol in a 1:1 ratio with the citric acid, and heated on a hotplate under vigorous stirring until a viscous gel formed. The gel was then dried in a furnace at 115 °C-150 °C, and finally calcined at 400 °C-500 °C into a amorphous raw powder. Table 3.5 gives exact heat treatment data for each compound, and a schematic overview of the sol-gel synthesis is given in Figure 3.2.

Table 3.5: Heat treatment of wet gel, dry gel and calcined raw powder to crystalline nano powder. The h−$YMn_{0.85}Ti_{0.15}O_3$ gel was dried at room temperature for 3 days before drying in a furnace. Data for h−$YMnO_3$ and h−$DyMnO_3$ are taken from Østmoe [9], and data for h−$YMn_{0.85}Ti_{0.15}O_3$ are taken from Hoggen [15].

h−$RMn_{1-x}Ti_xO_3$	Drying of gel	Calcination of gel	Annealing
h−$YMnO_3$	150 °C, 4 days	500 °C, 12 hours	850 °C, 2 hours
h−$YMn_{0.85}Ti_{0.15}O_3$	115 °C, 3 days	400 °C, 6 hours	800 °C, 1 hour
h−$DyMnO_3$	150 °C, 4 days	500 °C, 12 hours	850 °C, 2 hours

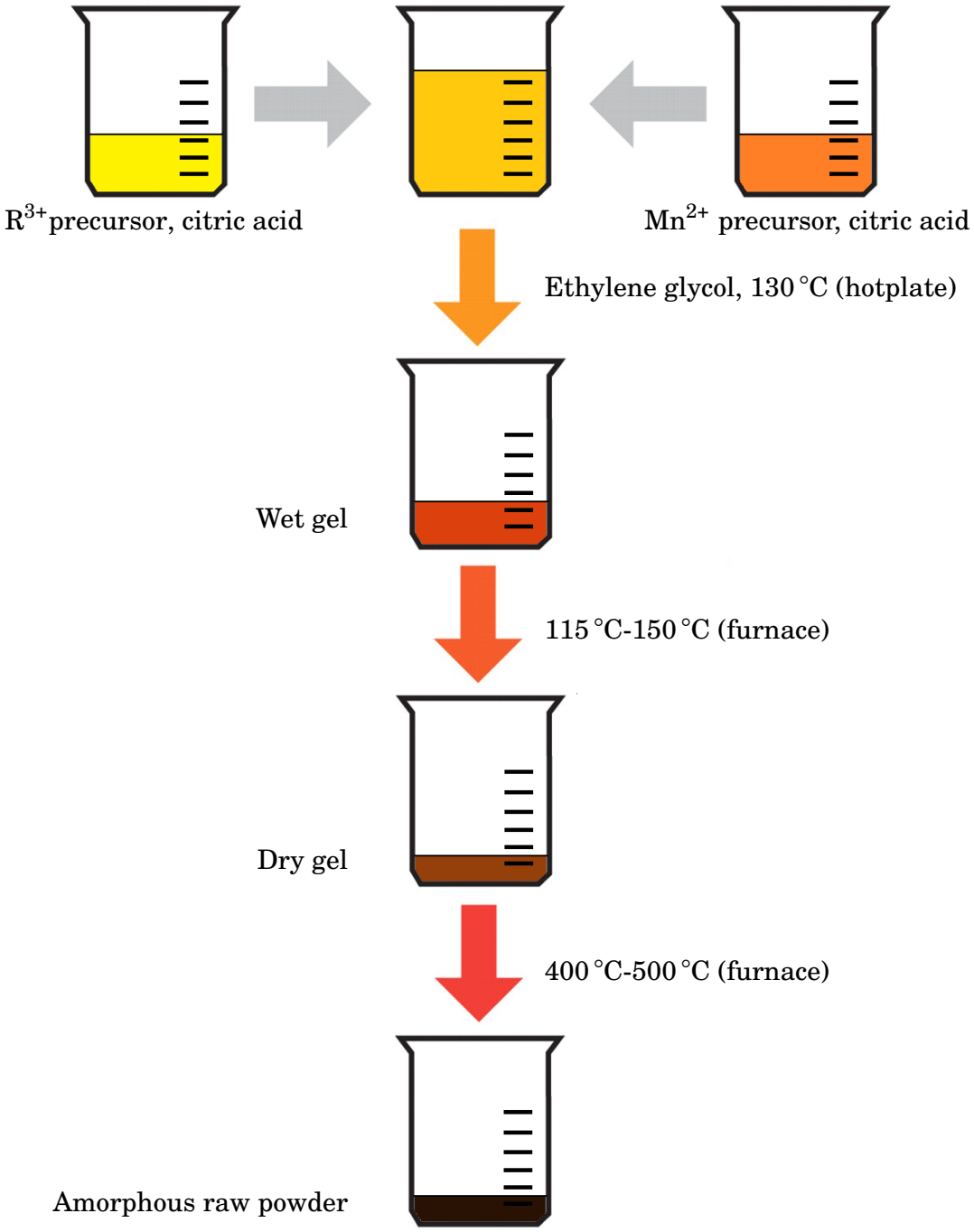

Figure 3.2: Schematic overview of the sol-gel synthesis route. Stoichiometric amounts of metal ion precursors dissolved with citric acid in distilled water were mixed with ethylene glycol, and then heated on a hotplate at 130 °C until gelling. The gel was then dried at 115 °C or 150 °C, and further calcined at 400 °C-500 °C to form an amorphous raw powder.

3.2 Characterization and Analysis

The phase purity of the prepared powders was determined by XRD. The crystallite sizes for the nano-sized powders were found by Rietveld refinement based on the XRD scans, and the crystallite sizes for the bulk-sized powders were determined by SEM imaging.

The oxygen absorption in the prepared powders was analyzed in terms of structural change, using HT-XRD, gravimetric change, using TGA, and electrochemical change, using Seebeck measurements and measuring DC conductivity.

3.2.1 Structural Measurements

The powders were studied with HT-XRD in O_2 and N_2 atmosphere to analyze the structural changes during oxygen absorption and desorption at various temperatures. Both measurements of changing temperature with constant atmosphere and isotherm measurements with switching atmospheres were conducted, investigating thermodynamical behavior and system kinetics, respectively. Figure 3.3 illustrates the measurements.

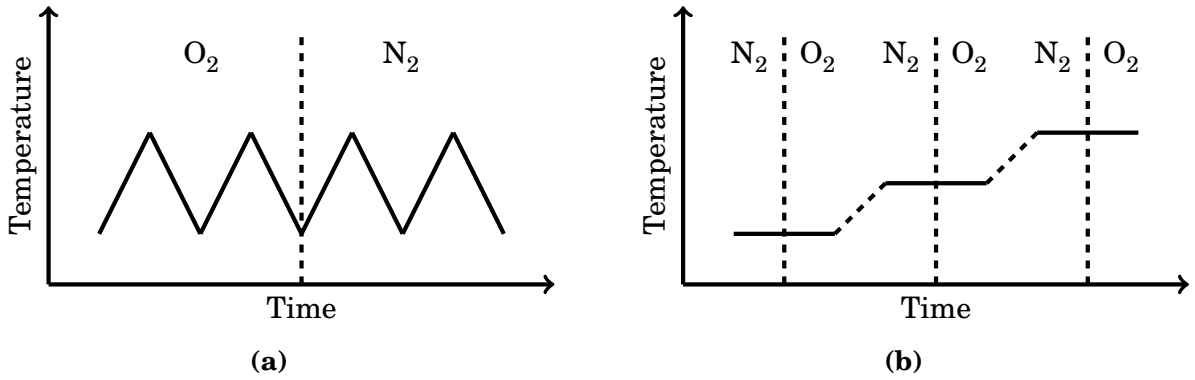

Figure 3.3: (a) HT-XRD measurement with varying temperature and constant atmosphere. After two heating-cooling cycles, the atmosphere was changed from O_2 to N_2. (b) HT-XRD measurement with constant temperature and switching atmosphere. Between each temperature segment, the materials were heated to an elevated temperature in N_2 to remove interstitial oxygen.

In the measurements with varying temperature, intervals of 20 °C and 40 °C were used, scanning a 2θ interval of 26.000°-72.012°. Table 3.6 gives the parameters used

in the measurement.

Table 3.6: Measurement parameters used in the HT-XRD structural characterization with varying temperature. The 2θ area scanned was 26.000°-72.012°, and the measurements were conducted in both O_2 and N_2.

h−$RMnO_3$	Time per step [s]	2θ step size [°]	Temp. range [°C]
Bulk h−$YMn_{0.85}Ti_{0.15}O_3$	1.0	0.03263236	50-600
Nano h−$YMn_{0.85}Ti_{0.15}O_3$	1.5	0.03263236	50-500
Nano h−$YMnO_3$	1.5	0.03263236	50-400
Nano h−$DyMnO_3$	1.25	0.03263236	50-450

In the isothermal measurements with switching atmospheres a narrower 2θ interval was examined. The interval scanned were chosen to only include the (004) peak and the (112) peak, since it is possible to can calculate the c and a parameters of the manganites based on these two peaks. Table 3.7 gives the parameters used in the measurement.

Table 3.7: Measurement parameters used in the isotherm HT-XRD structural characterization with switching atmospheres. The measurements were conducted by switching from N_2 to O_2 after "emptying" the materials at elevated temperatures in N_2. Time used per step was varied for different temperatures to ensure a sufficient amount of data. As a reference to the nano-sized powders and the Ti-doped bulk-sized powder, bulk- and 150 nm-sized h−$YMnO_3$ powder was scanned at 205 °C and 245 °C, respectively.

h−$RMnO_3$	2θ interval [°]	2θ resolution [°]	Temp. range [°C]
Bulk h−$YMn_{0.85}Ti_{0.15}O_3$	31.300-33.307	0.04894854	165-405
Nano h−$YMn_{0.85}Ti_{0.15}O_3$	30.750-33.491	0.04894854	165-245
Bulk h−$YMnO_3$	31.050-33.889	0.04894854	205
150 nm h−$YMnO_3$	31.050-33.889	0.04894854	245
Nano h−$YMnO_3$	31.050-33.889	0.04894854	145-245
Nano h−$DyMnO_3$	31.050-33.497	0.04894854	225-305

3.2.2 Thermogravimetric Measurements

TGA was used to quantitatively determining the oxygen absorption and desorption for bulk- and nano-sized $YMn_{0.85}Ti_{0.15}O_3$ in O_2. The measurements were conducted during both heating and cooling of the powders. The measurement were performed at a slow heating and cooling rate of $1\,°C\,min^{-1}$ to ensure that the materials could reach

equilibrium at every measuring point. A gas flow of 30 mL min^{-1} was used to ensure an atmosphere with excess of O_2. Table 3.8 gives an overview of temperature intervals used for the different materials.

Table 3.8: Temperature rate, temperature range and O_2 gas flow for the TGA measurements.

h−$RMnO_3$	Temp. rate [°C s^{-1}]	Temp. range [°C]	Gas flow [mL min^{-1}]
Bulk $YMn_{0.85}Ti_{0.15}O_3$	1.0/−1.0	30-900	30
Nano $YMn_{0.85}Ti_{0.15}O_3$	1.0/−1.0	30-600	30

Although a heating and cooling rate of 1 °C min^{-1} is slow, the maximal potential of the powders in terms of oxygen absorption is not reached with this value. To find the true peak in oxygen absorption, a heating rate around 0.1 °C min^{-1} should be used, as seen in Remsen *et. al* [21]. Such measurements takes weeks to perform, and for the sake of relative comparisons between the hexagonal rare-earth manganites a temperature rate of 1 °C min^{-1} is sufficient.

3.2.3 Electrochemical Measurements

The electrochemical measurements were performed on solid bodies in form of prisms. Porous, square prisms with length 20 mm, width 5 mm and height 3 mm were prepared by uniaxial pressing of bulk-sized h−$YMnO_3$ and bulk-sized h−$YMn_{0.85}Ti_{0.15}O_3$ powder. The prisms were sintered in air at 1300 °C for 6 hours. Only bulk powder was used due to coarsening of nano powder at the sintering temperatures used.

DC Conductivity Measurements

DC conductivity measurements was performed one the aforementioned prisms in two manners: First the samples were heated and cooled in N_2 and O_2 to measure the conductivity as a function of temperature. The cycling measurement in N_2 serves as a reference for the conductivity measured when cycling in O_2. Two cycles in O_2 were performed, see Figure 3.5a. Then, conductivity relaxations were measured at different temperatures, switching gas from O_2 to N_2 and than back to O_2, see Figure 3.5b. Cycling temperature range and conductivity relaxation temperatures are given in Table 3.9.

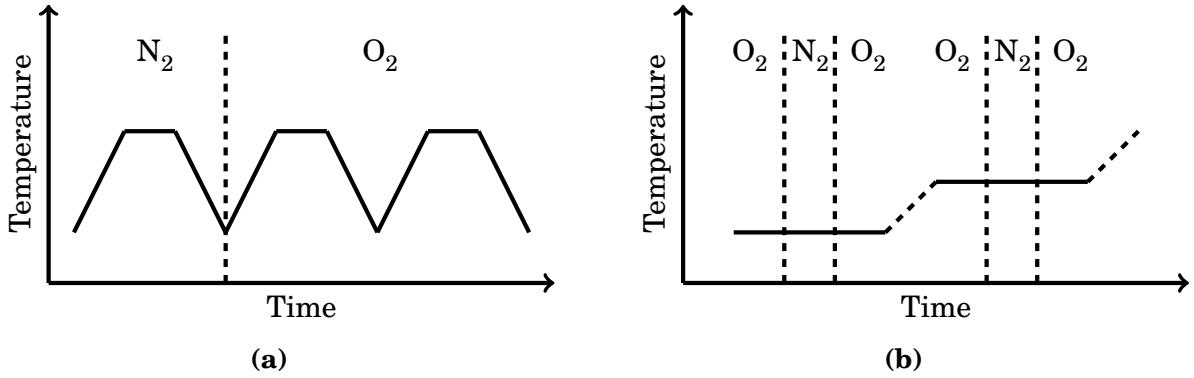

Figure 3.4: (a) DC measurement during heating and cooling in N_2 and O_2. The cycle in N_2 serves as a reference for the conductivity measured in O_2. The heating and cooling rate was 60 °C h^{-1}, and the holding time at maximum temperature was 30 min. (b) Conductivity relaxation measurements at constant temperature and switching atmosphere. The materials were heat treated at elevated temperatures in O_2 before each relaxation measurement.

Table 3.9: Cycling temperature range, conductivity relaxation temperatures and heating/cooling rate for the DC measurements.

h−$RMnO_3$	Temp. range [°C]	Temp. rate [°C h^{-1}]	Relaxation temp. [°C]
h−$YMn_{0.85}Ti_{0.15}O_3$	100-800	60	315, 365
h−$YMnO_3$	100-500	60	275

Seebeck Coefficient Measurements

The same prisms as in the DC conductivity measurement were used in the measurements of the Seebeck coefficient. The Seebeck coefficient was determined at various temperatures, first during heating and cooling in N_2 and then during heating and cooling in O_2, see Figure 3.5. The temperatures at which each measurement was performed were the same during heating and cooling and the same in both N_2 and O_2. For h−$YMn_{0.85}Ti_{0.15}O_3$, measurements were done at every 50 °C between 200 °C and 400 °C, and then every 100 °C from 400 °C to 800 °C. For h−$YMnO_3$, measurements were done at every 25 °C between 200 °C and 300 °C, and then every 100 °C from 300 °C to 800 °C. Table 3.10 summarizes the measurement parameters.

Table 3.10: Temperature steps, holding time per step and measuring frequency used in the Seebeck measurements. The temperature steps were the same upon heating and cooling, both in N_2 and O_2.

h−$RMnO_3$	Temp. [°C]	Hold time [h]	Freq. [min^{-1}]
h−$YMn_{0.85}Ti_{0.15}O_3$	200, 250, 300, 350, 400, 500, 600, 700, 800	3	1
h−$YMnO_3$	200, 225, 250, 275, 300, 400, 500, 600, 700, 800	3	1

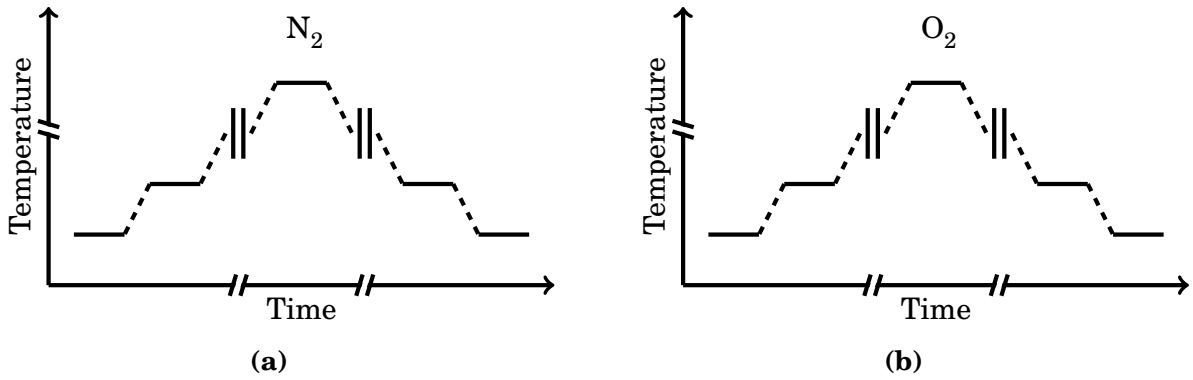

Figure 3.5: Temperature program for measuring Seebeck coefficient at various temperatures, first (a) in N_2, then (b) in O_2. The temperature program is identical for both atmospheres. The temperature steps, however, are different between h−$YMn_{0.85}Ti_{0.15}O_3$ and h−$YMnO_3$, see Table 3.10.

Chapter 4

Results

Except from the bulk-sized Ti-doped h−$YMnO_3$, all of the results presented are measured on materials from a single synthesis batch. The bulk-sized h−$YMn_{0.85}Ti_{0.15}O_3$ first prepared was used up during the analysis, and thus a second batch was synthesized to measure the electrochemical properties.

The following abbreviations are used for the materials on the figures in this chapter: Bulk Y (bulk-sized h−$YMnO_3$), 150 nm Y (150 nm-sized h−$YMnO_3$), Nano Y (nano-sized h−$YMnO_3$), Bulk $Y_{Ti\text{-}dop.}$ (bulk-sized h−$YMn_{0.85}Ti_{0.15}O_3$), Nano $Y_{Ti\text{-}dop.}$ (nano-sized h−$YMn_{0.85}Ti_{0.15}O_3$), Nano Dy (nano-sized h−$DyMnO_3$).

4.1 Structure Characterization

The synthesized hexagonal manganite powders were characterized with XRD to confirm phase purity, see Figure 4.1. Based on mentioned X-ray diffraction data, the crystallite sizes of the nano-sized powders were determined by Rietveld refinement. The crystallite size of the bulk powders were determined by SEM imaging, see Appendix B. The crystallite sizes are given in Table 4.1.

Table 4.1: List of crystallite sizes of hexagonal manganite powders analyzed in this study.

h−$RMnO_3$	Crystallite size	Measuring method
Bulk h−$YMnO_3$	2-14 µm	SEM
Bulk h−$YMn_{0.85}Ti_{0.15}O_3$	2-17 µm	SEM
Nano h−$YMn_{0.85}Ti_{0.15}O_3$	18.7 nm	Rietveld, XRD
Nano h−$DyMnO_3$	22.6 nm	Rietveld, XRD
Nano h−$YMnO_3$	25.5 nm	Riedveld, XRD

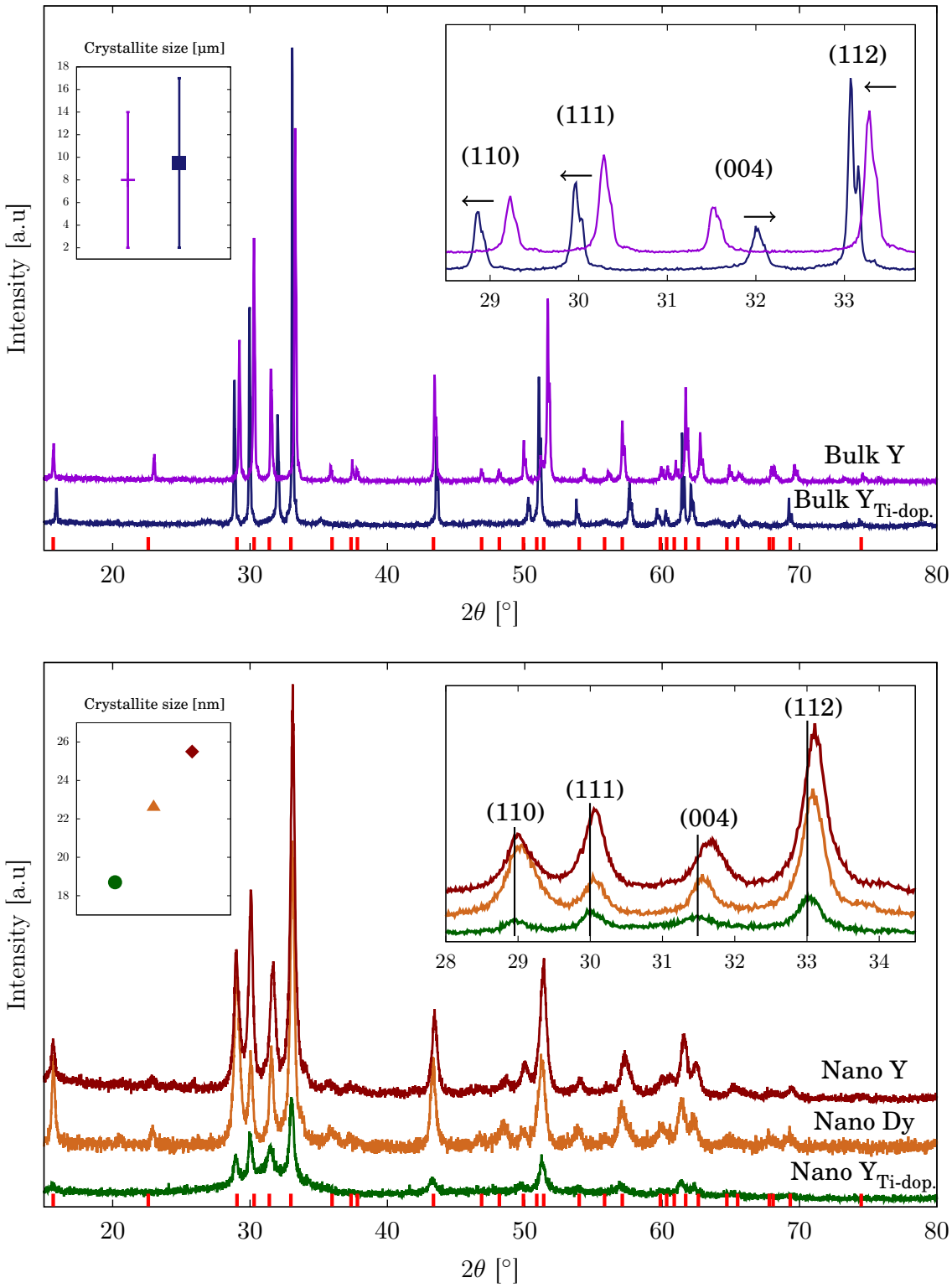

Figure 4.1: X-ray diffractogram of bulk-sized h−$YMnO_3$ and h−$YMn_{0.85}Ti_{0.15}O_3$ (top) and nano-sized h−$YMnO_3$, h−$DyMnO_3$ and h−$YMn_{0.85}Ti_{0.15}O_3$ (bottom). The relative differences in intensity between the nano-sized powders are due to the difference in crystallite size.

4.1.1 HT-XRD Characterization

Lattice Parameters During Heating and Cooling

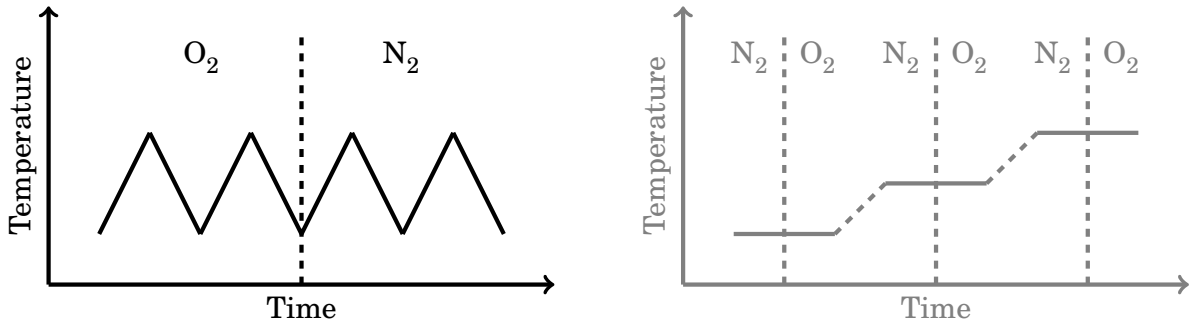

Based on the HT-XRD scans during heating and cooling in O_2 and N_2, the a and c parameter of the materials were determined by the Pawley Method [62] in TOPAS. Space group 185, i.e. $P6_3cm$, was used as *hkl* phase, and a background order of 1 was used for all refinements. Two corrections were used; sample displacement and LP-Factor, both fixed to 0. The nano-sized powders were refined on Lorentzian crystallite size, while the bulk powders were refined on both Lorentzian crystallite size and Lorentzian crystallite strain. Table 4.2 shows all refinement settings for the Pawley Method refinement.

Table 4.2: Refinement settings for Pawley Method refinement of HT-XRD measurements.

Settings	Bulk powder	Nano powder
Background order	1	1
Corrections:		
2th, sample displacement	0 (fixed)	0 (fixed)
Intensity, LP-Factor [°]	0 (fixed)	0 (fixed)
Refining	L size, L strain	L size

The results from the Pawley Method refinement are plotted as a function of temperature, see Figure 4.3 and 4.4, and Figure C.1 and C.2 in Appendix C. Figure 4.3 and 4.4 show the a and c parameter as a function of temperature during heating/cooling in O_2 and N_2, respectively. The y-axes are kept equal in these two figures for comparison. Figure C.1 shows c/a as a function of temperature in both O_2 and N_2. Figure C.2 show the unit cell volume, V, as a function of temperature in both O_2 and N_2.

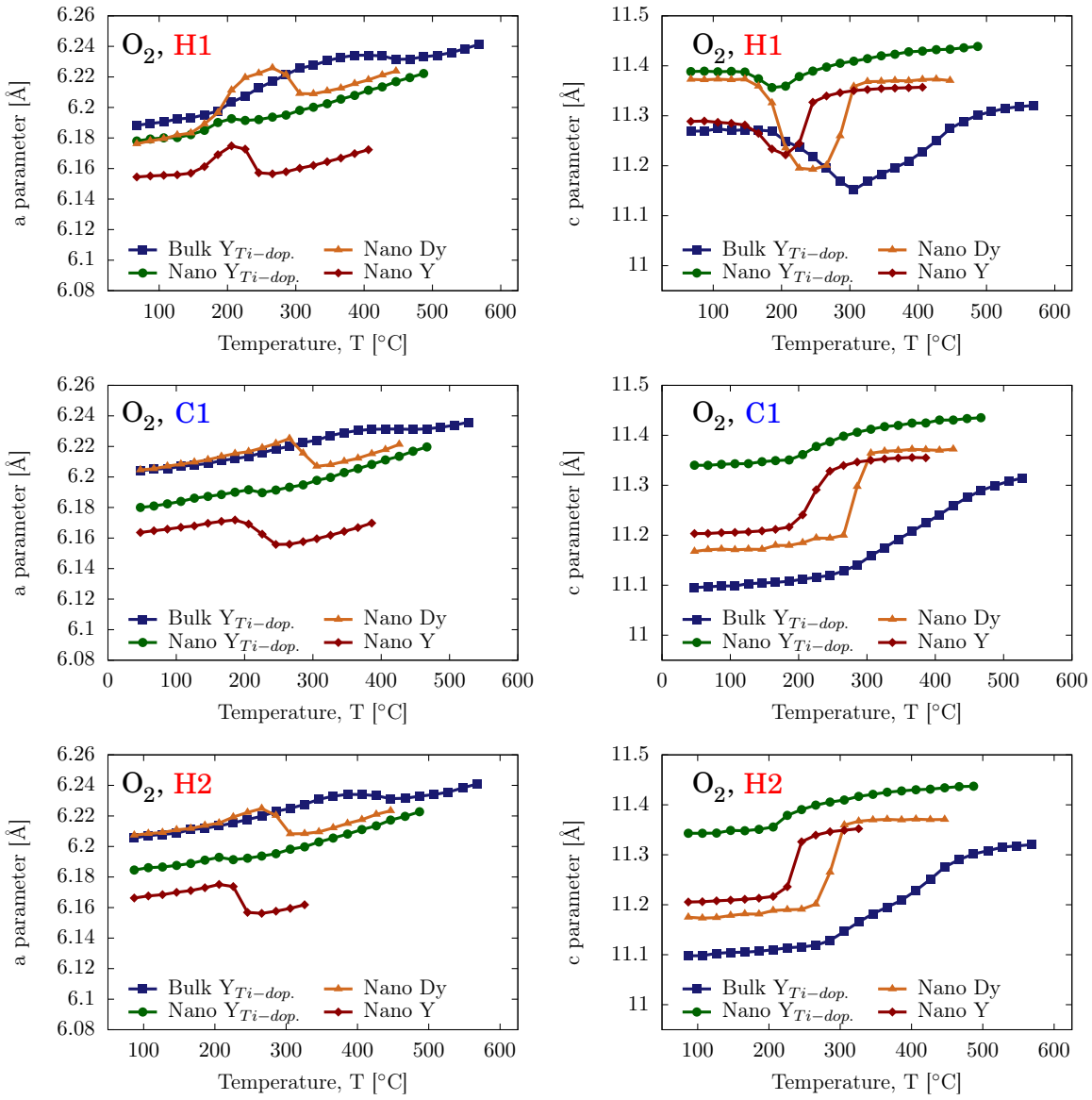

Figure 4.3: HT-XRD measurements of the a and c parameter from heating and cooling in O_2. The top row represents heating 1 (H1), the middle row cooling 1 (C1), and the bottom row is from heating 2 (H2). The left column includes graphs of the a parameter, while the right column includes graphs of the c parameter.

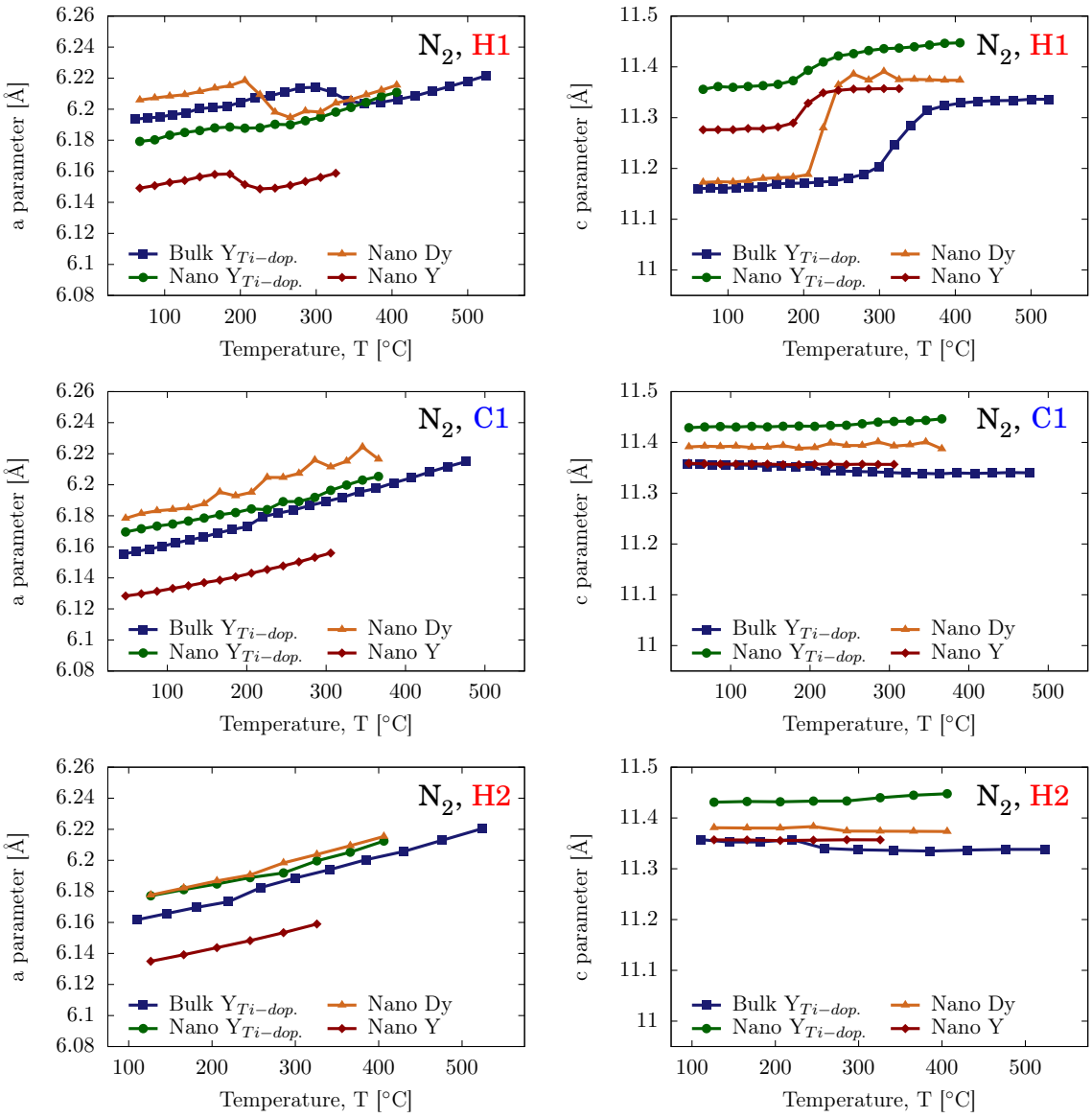

Figure 4.4: HT-XRD measurements of the a and c parameter from heating and cooling in N_2. The top row represents heating 1 (H1), the middle row cooling 1 (C1), and the bottom row is from heating 2 (H2). The left column includes graphs of the a parameter, while the right column includes graphs of the c parameter.

Lattice Parameters During Switching Atmosphere

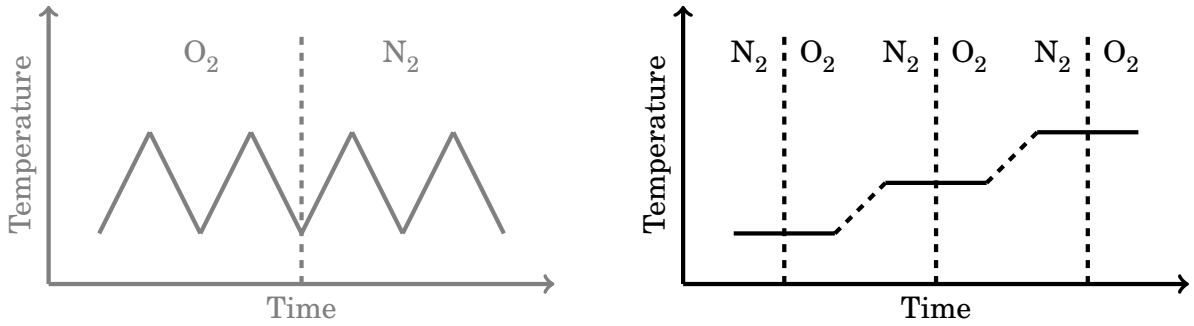

Based on the isothermal HT-XRD scans with switching atmospheres, the (004) and (112) peak positions, see Figure 4.1, of the materials were determined by Single Peak Fitting refinement in TOPAS. Initial peak positions were manually placed on each scan on the (004) peak and the (112) peak. The peak fitting was then refined on Lorentzian crystallite size for the nano-sized powders, and Lorentzian crystallite size and Lorentzian crystallite strain for the bulk-sized powders. The other refinement parameters were identical to the Pawley Method refinement, see Table 4.2.

From the peak positions found by the Single Peak Fitting refinement the a and c parameter were calculated. This was obtained by using the d-spacing equation for hexagonal crystal structures and Bragg's Law, see Equation 2.2 and 2.3. The a and c parameters calculated from the Single Peak Fitting refinement are plotted as a function of time, see Figure 4.6-4.8. The y-axes are kept equal in Figure 4.6 and 4.7 for comparison.

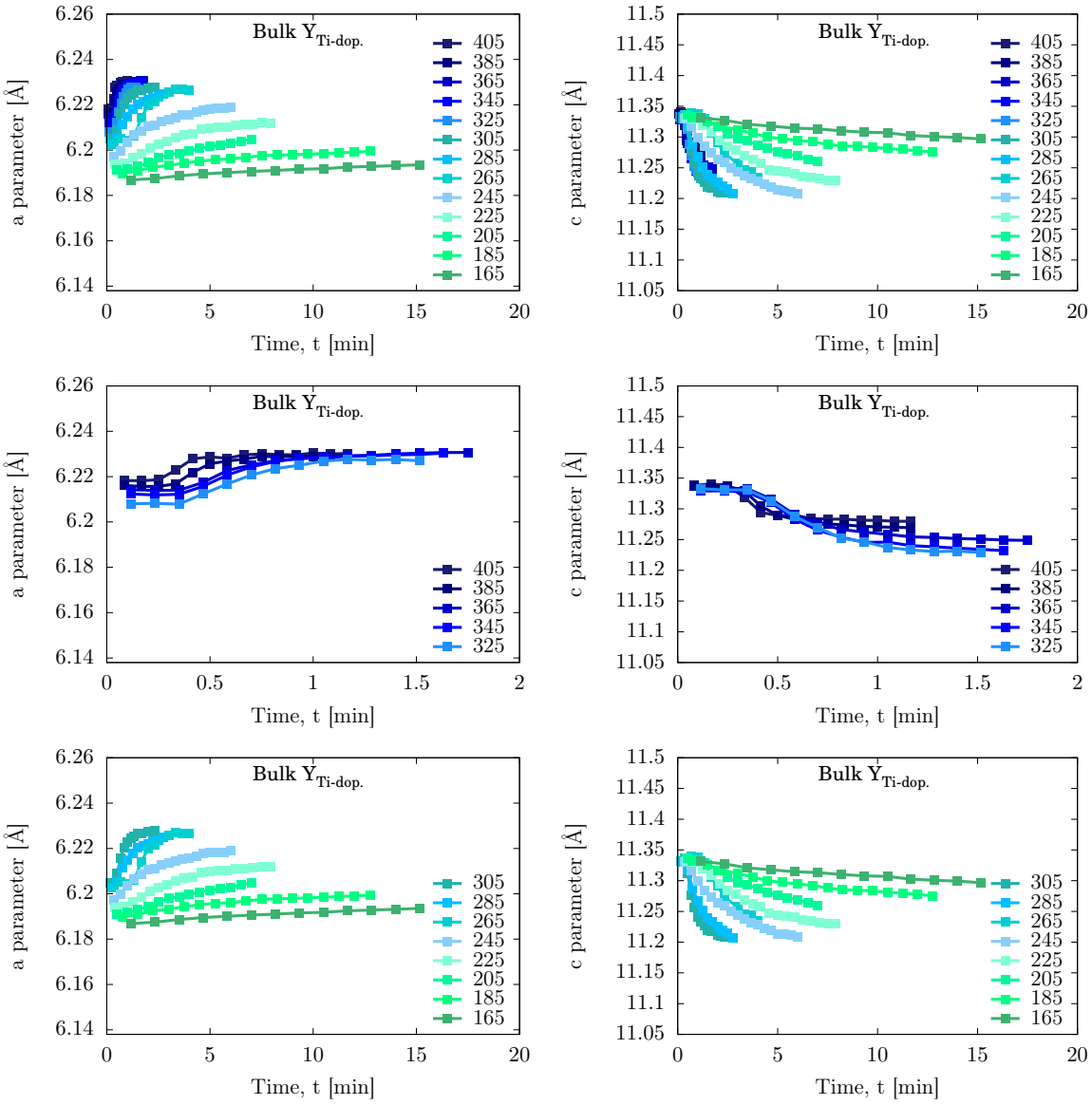

Figure 4.6: Change in lattice parameter a (left) and c (right) in bulk-sized h−$YMn_{0.85}Ti_{0.15}O_3$ when switching from N_2 to O_2 at different temperatures. The two upper plots show all temperatures, while the four lower show narrower temperature regions.

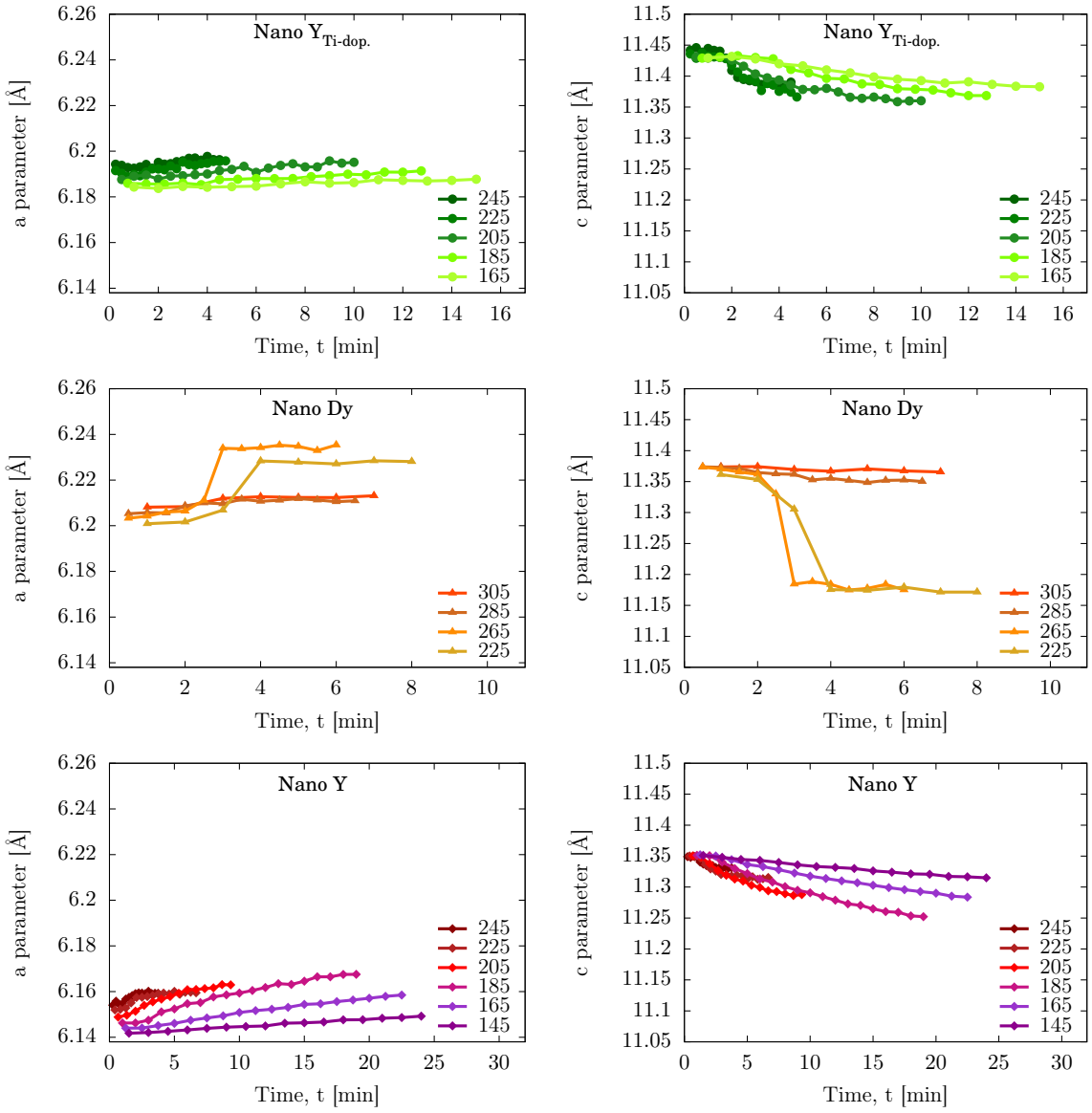

Figure 4.7: Change in lattice parameter a (left) and c (right) for nano-sized h−$YMn_{0.85}Ti_{0.15}O_3$ (top), nano-sized h−$DyMnO_3$ (center) and nano-sized h−$YMnO_3$ (bottom) when switching from N_2 to O_2 at different temperatures.

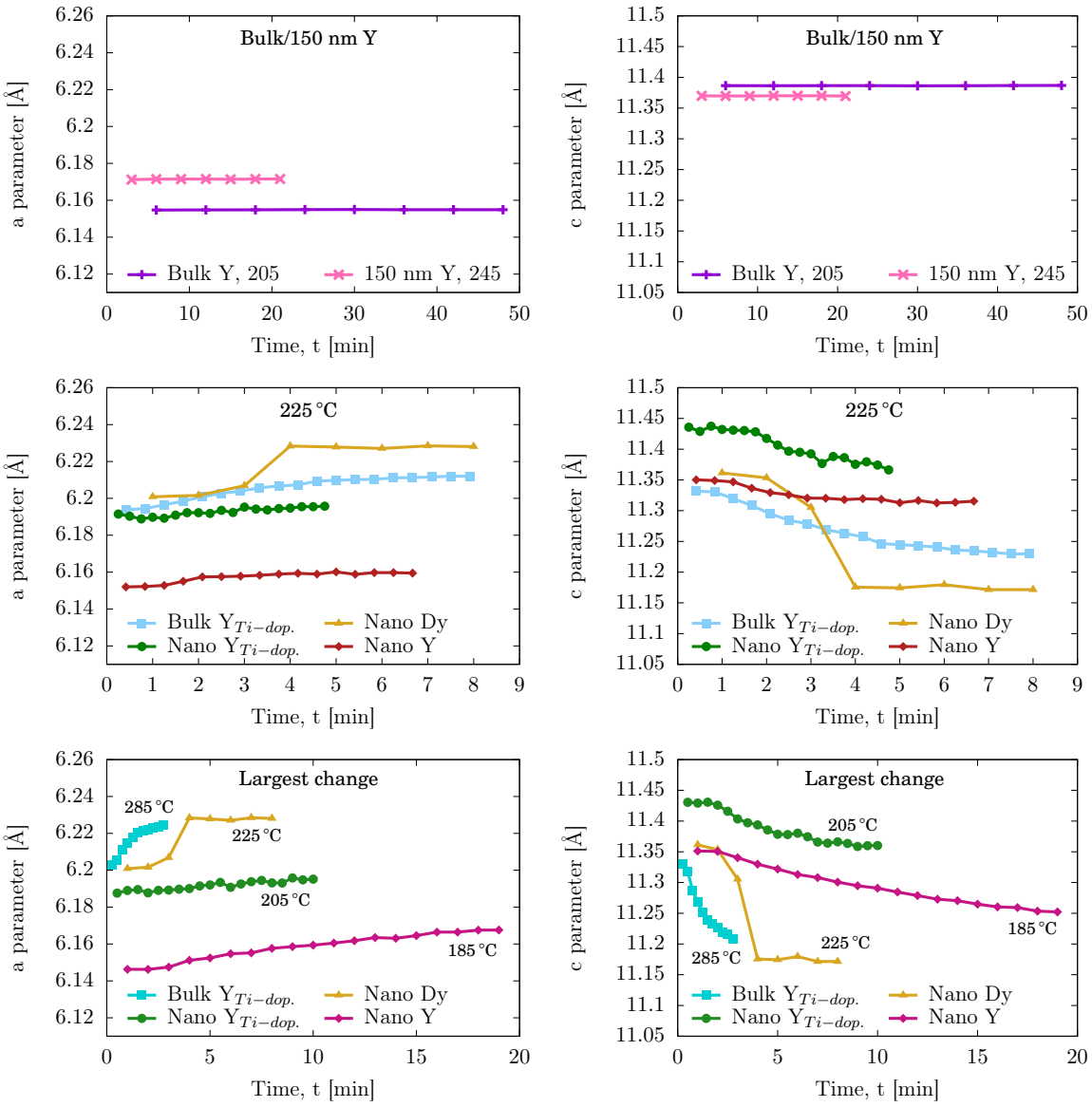

Figure 4.8: Change in lattice parameter a (left) and c (right) when switching from N_2 to O_2 at different temperatures. The top plots show bulk- and 150 nm-sized h−$YMnO_3$. The center plots show all materials at 225 °C. The bottom plots show all materials at the temperature where their lattice parameter change is highest. Note that the time at which the atmosphere was switched can vary from material to material.

4.2 Thermogravimetric Analysis

The out-put measurements from the TGA are given in weight percent of initial sample weight. From this, δ-values (h$-RMnO_{3+\delta}$) were calculated, assuming the lowest measured weight percent values for each material corresponded to a stoichiometric compound with $\delta = 0$.

The changes in mass, plotted as $3+\delta$, during heating and cooling in O_2 found by TGA are given in Figure 4.9 and 4.10. Figure 4.9 also includes smaller plots where the change in weight percent is given.

In addition to the measurements performed on bulk- and nano-sized h$-YMn_{0.85}Ti_{0.15}O_3$, data for nano-sized h$-YMnO_3$ and nano-sized h$-DyMnO_3$ measured by Østmoe [9] are included. The latter data was obtained by using the exact same measuring parameters as in this study, i.e. a temperature rate of $1\,^{\circ}\mathrm{C\,min^{-1}}$ and an O_2 flow of $30\,\mathrm{mL\,min^{-1}}$. The powders used for these measurements are also from the same batch as the powders used in this study.

The highest observed oxygen absorption from the TGA measurements for the different compounds are given in Table 4.3. The oxygen uptake is both given as change in weight percent and as δ-values.

Table 4.3: Highest observed wt% change and δ-values of excess oxygen in h$-RMnO_{3+\delta}$. The δ-values were calculated assuming the lowest measured weight percent values for each material corresponded to a stoichiometric compound with $\delta = 0$.

h$-RMnO_3$	Change, mass [wt%]	Change, $3+\delta$ [-]
Bulk-sized h$-YMn_{0.85}Ti_{0.15}O_3$	1.4726	3.177
Nano-sized h$-YMn_{0.85}Ti_{0.15}O_3$	1.2675	3.150
Nano-sized h$-DyMnO_3$	1.6155	3.264
Nano-sized h$-YMnO_3$	1.4918	3.180

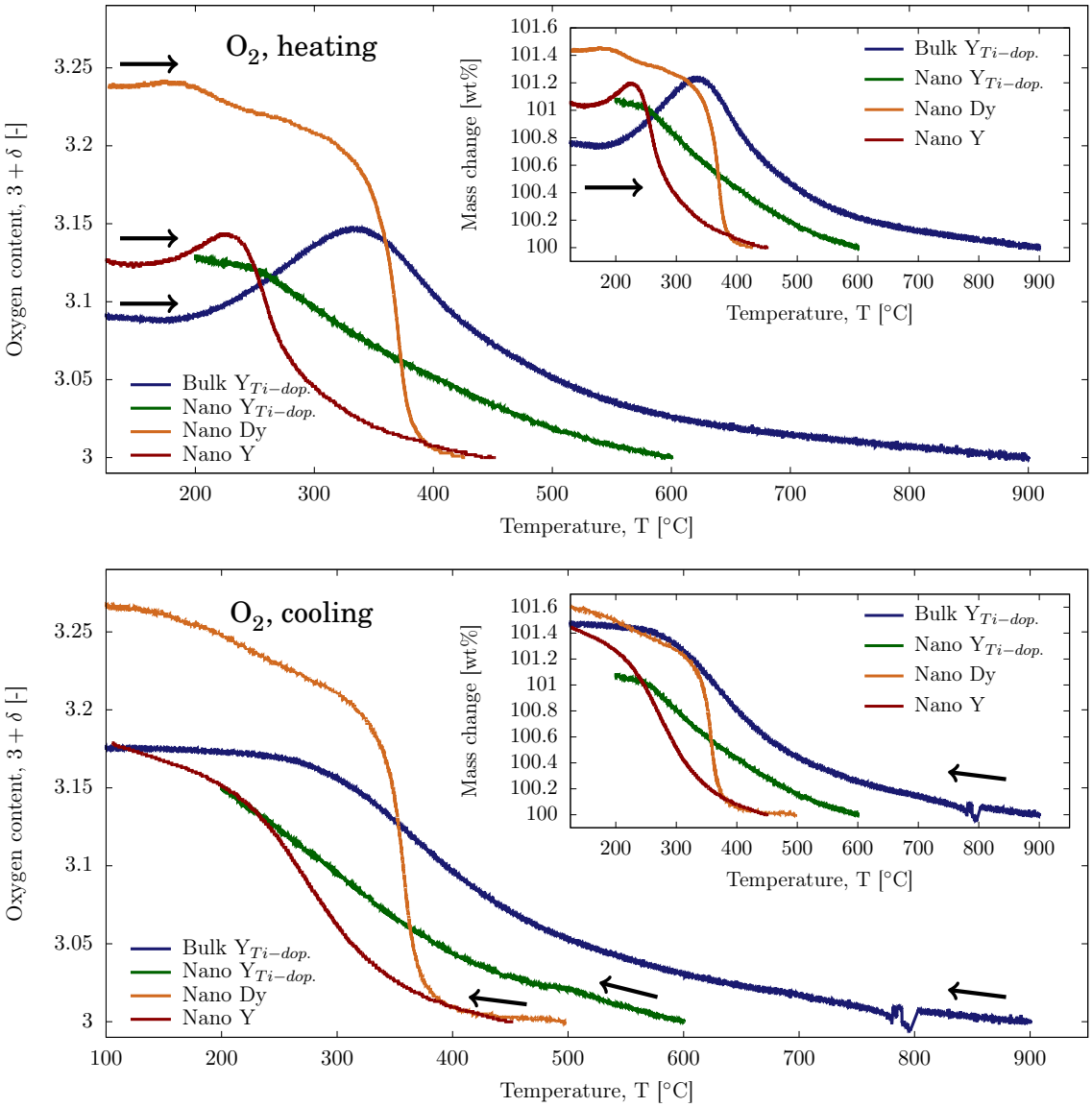

Figure 4.9: Calculated change of oxygen content in h−$RMnO_{3+\delta}$ from the TGA measurement data as a function of temperature. The top plot compares values upon heating, and the bottom plot compare values upon cooling. The smaller plots show mass change in weight percent. The data used to calculate the oxygen change in h−$DyMnO_3$ and h−$YMnO_3$ were measured by Østmoe [9].

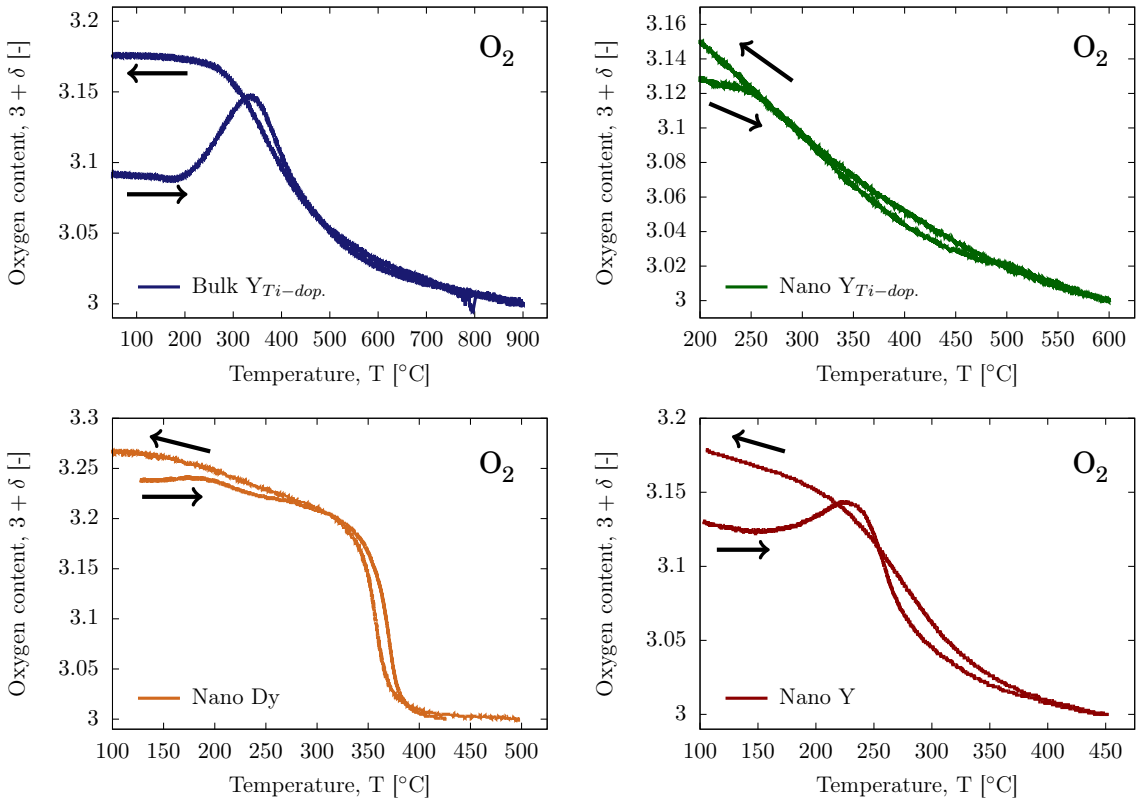

Figure 4.10: Calculated change of oxygen content in h−$RMnO_{3+\delta}$ from the TGA measurement data as a function of temperature. The arrows point in the direction of heating and cooling. The data used to calculate the oxygen change in h−$DyMnO_3$ and h−$YMnO_3$ were measured by Østmoe [9].

4.3 Electrochemical Analysis

4.3.1 DC Conductivity

For the DC conductivity measurements, platinum wire was carefully wrapped around the prepared prisms, forming electrodes. Platinum paste was cured on the contact points between the wires and the prisms to optimize the contact area. The curing was carried out at 850 °C for 1 h.

Conductivity During Heating and Cooling

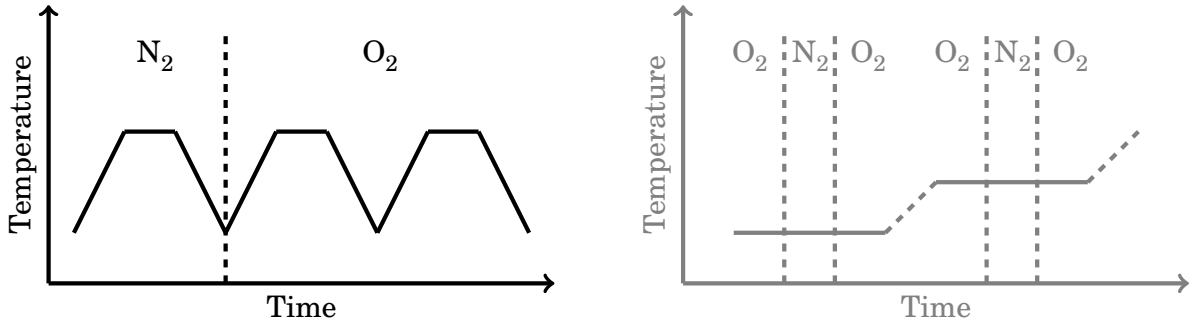

Conductivity measurements during heating and cooling were carried out once in N_2 and twice in O_2. The conductivity measurements from the two materials are plotted together as a function of temperature, see Figure 4.12. The y-axis is scaled logarithmic to better visualize the conductivity effect of oxygen absorption/desorption. In Appendix D these measurements are also plotted in a semi logarithmic plot as a function of time, see Figure D.1, and with y-axes linearly scaled, see Figure D.2 and D.3. Table 4.4 gives the conductivity for each sample at 500 °C.

Table 4.4: DC conductivity at 500 °C for the two samples through the measurements in N_2 and O_2. Conductivity values for both heating (H) and cooling (C) are given for the Ti^{4+} doped sample.

h−$RMnO_3$	N_2 [µS cm^{-1}]	O_2, 1 [µS cm^{-1}]	O_2, 2 [µS cm^{-1}]
Bulk h−$YMn_{0.85}Ti_{0.15}O_3$	291.13 (H), 718.81 (C)	135.95 (H), 162.15 (C)	144.57 (H), 161.73 (C)
Bulk h−$YMnO_3$	81.00	199.30	200.33

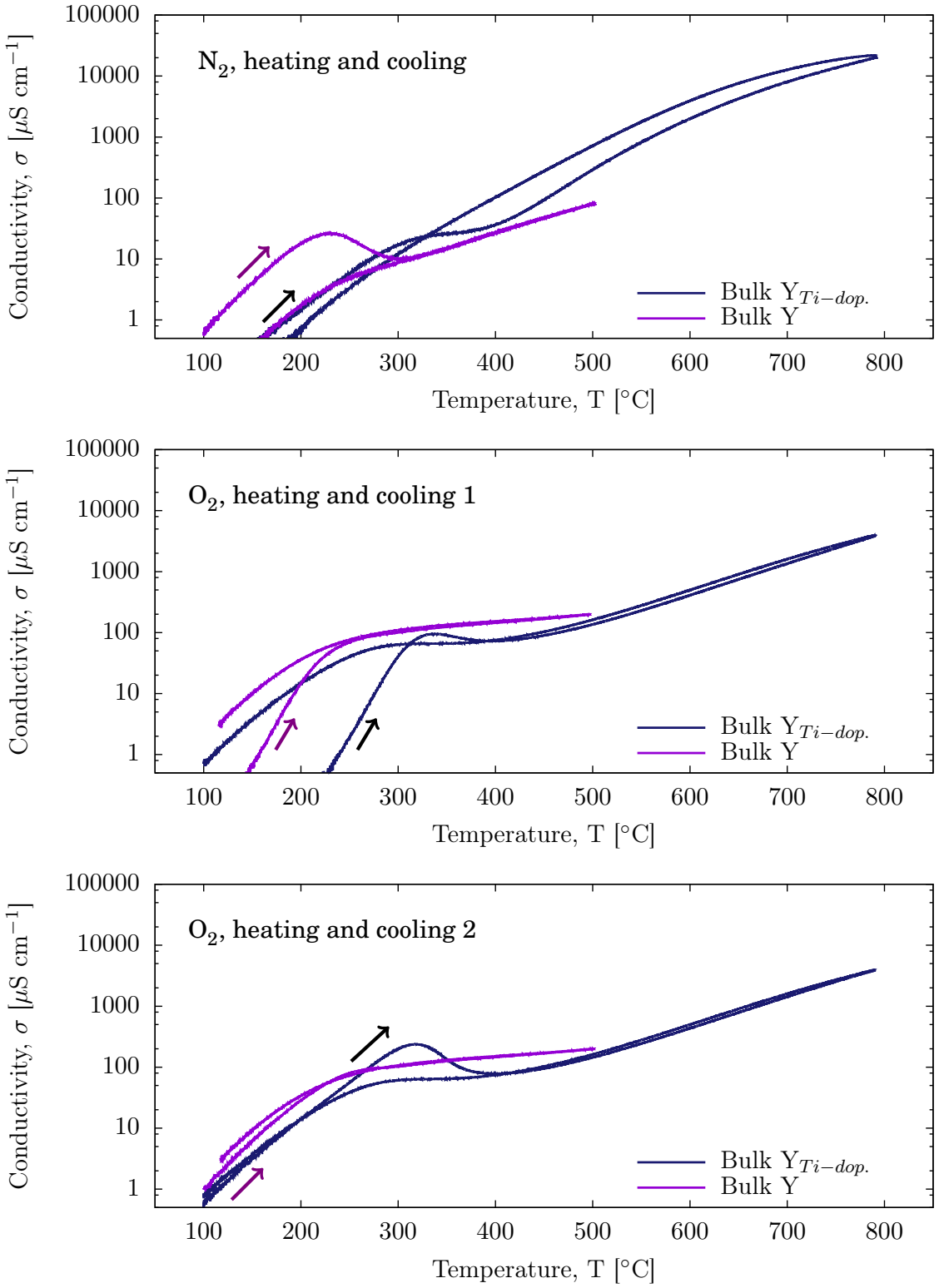

Figure 4.12: Conductivity during heating and cooling in N_2 (top) and O_2 (center and bottom) as a function of temperature. The arrows point in the direction of heating.

Relaxation Conductivity

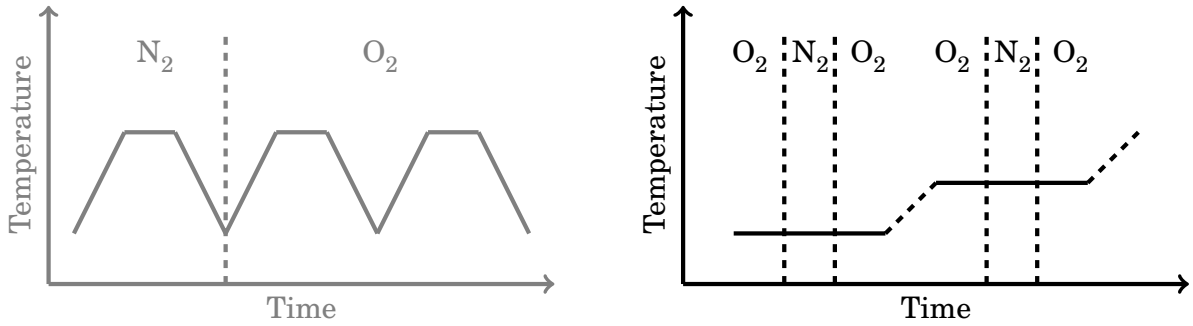

The conductivity relaxation measurements obtained at 275 °C for h−$YMnO_3$ and at 315 °C and 365 °C for h−$YMn_{0.85}Ti_{0.15}O_3$ are plotted in Figure 4.14. In addition to the aforementioned, measurements done by Nesdal [11] at 250 °C and 300 °C for h−$YMnO_3$ are included. In Figure 4.14 the y-axes are linear and kept equal for comparison. The x-axes are given in minutes, and the point when switching from O_2 to N_2 is given as point zero.

As seen from Figure 4.14, Nesdal's measurements do not fit the conductivity values of the measurement at 275 °C performed in this study, and may originate from sample differences in terms of dimension, density and crystallite size. The kinetic aspect and the relative conductivity changes, however, are comparable.

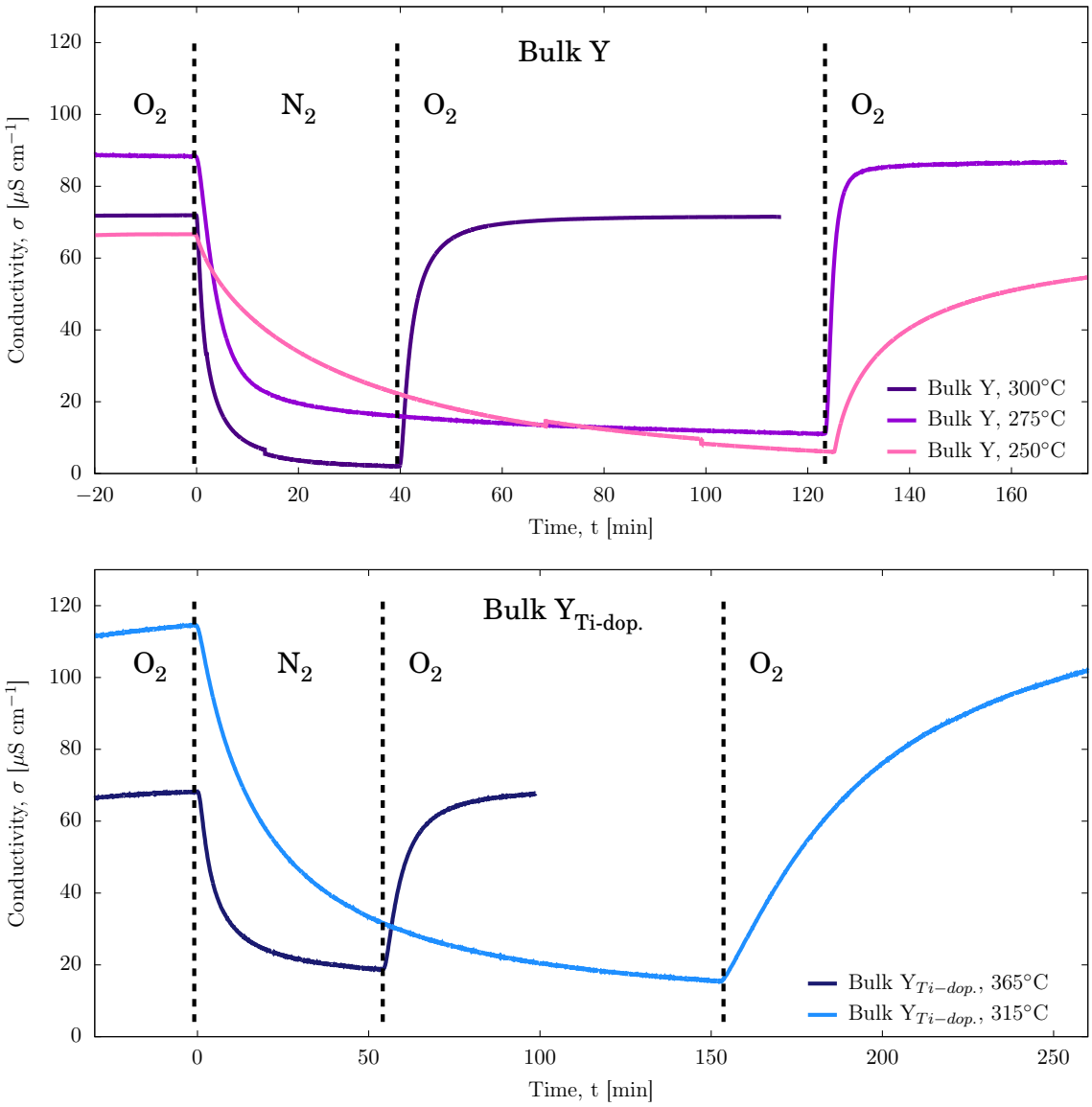

Figure 4.14: Conductivity relaxation measurements of bulk-sized h−$YMnO_3$ (top) and bulk-sized h−$YMn_{0.85}Ti_{0.15}O_3$ (bottom). The samples used were the same as in the conductivity measurements with varying temperature. The y-axes are linear and equal in range, and the x-axes have t = 0 min as the time where the atmosphere is switched from O_2 to N_2. The measurements for h−$YMnO_3$ at 250 °C and 300 °C were performed by Nesdal [11].

4.3.2 Seebeck Coefficient

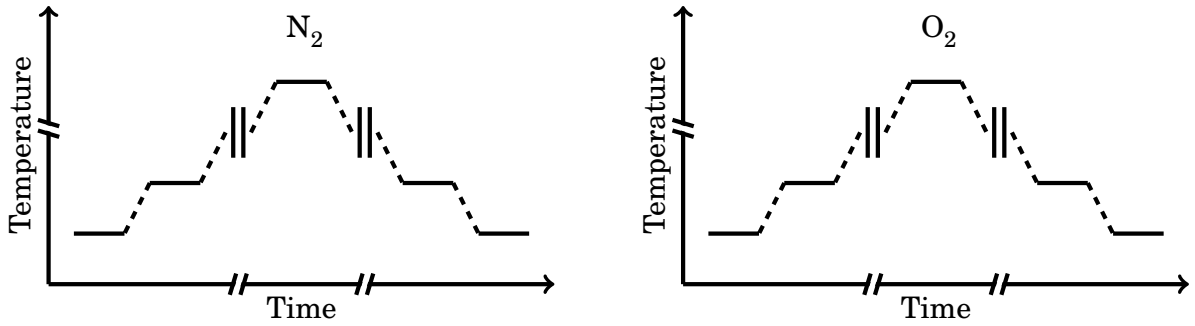

For each isotherm step in the Seebeck measurements, an average value of the Seebeck coefficient was calculated. At low temperatures for h−$YMnO_3$ it was difficult to obtain stable values during the 3 hours holding time. Thus, some values upon heating in N_2 and cooling in O_2 have been neglected.

The Seebeck coefficients measured as a function of temperature upon heating and cooling in N_2 and O_2 are given in Figure 4.16 and 4.17. Figure 4.16 shows the Seebeck coefficient for h−$YMnO_3$ and Figure 4.17 shows the Seebeck coefficient for h−$YMn_{0.85}Ti_{0.15}O_3$. The y-axes for each material are kept equal. Although few values were obtained from each measuring, plot lines are included in the figures to show the trends. In both figures the measurements during heating are plotted in red, while the measurements during cooling are plotted in blue. In addition to this, a dotted line representing the limit between positive and negative Seebeck values is included in both plots.

Note that the samples had been heated in O_2 during the DC measurements before the Seebeck measurements in N_2. Thus, h−$YMnO_3$ and h−$YMn_{0.85}Ti_{0.15}O_3$ were oxidized as the measurements in N_2 started, leading to a reduction as the samples were heated in N_2.

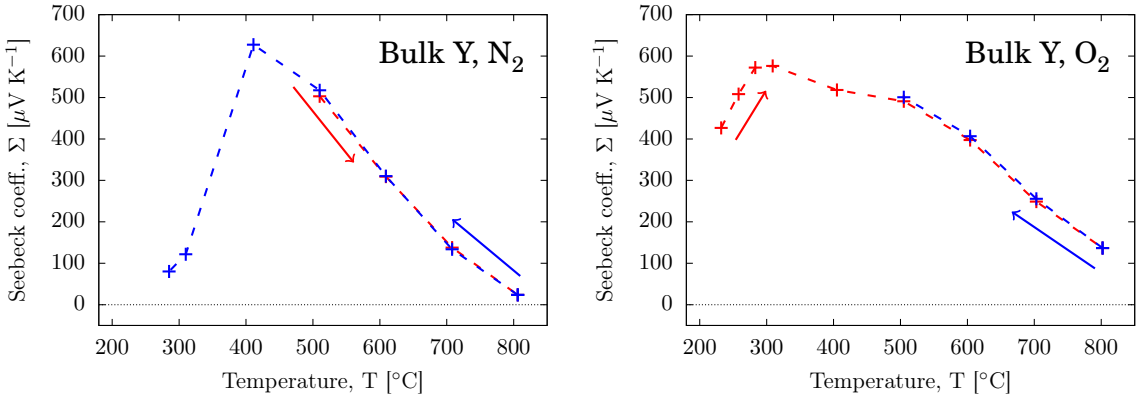

Figure 4.16: Seebeck coefficient as a function of temperature in N_2 (left) and O_2 (right) for h−$YMnO_3$. The red values are measured during heating, and the blue values are measured during cooling. All values are positive, indicating that h−$YMnO_3$ is a p-type conductor for all temperatures and all partial pressures of O_2.

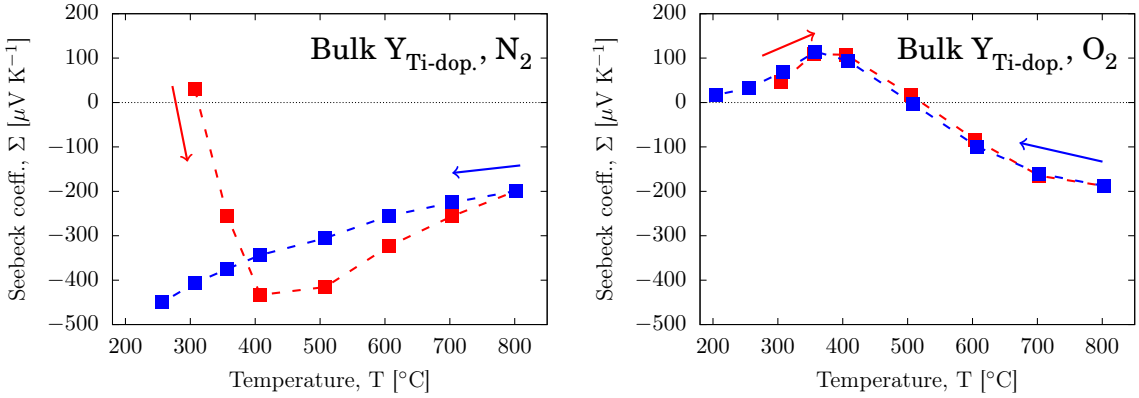

Figure 4.17: Seebeck coefficient as a function of temperature in N_2 (left) and O_2 (right) for h−$YMn_{0.85}Ti_{0.15}O_3$. The red values are measured during heating, and the blue values are measured during cooling. When oxidized at low temperatures, h−$YMn_{0.85}Ti_{0.15}O_3$ is a p-type conductor with positive Seebeck coefficients. When reduced at elevated temperatures, the material becomes an n-type conductor with negative Seebeck coefficients.

Chapter 5

Discussion

Based on the results in this study and work done in similar studies, the effect of donor doping with Ti^{4+} in hexagonal rare-earth manganites will now be evaluated and tried explained. As seen from the results presented in Chapter 4, doping with Ti^{4+} affect several dimensions in the oxygen absorption process in $h-RMnO_3$. However, crystallite size and type of R-cation in $h-RMnO_3$ also seem to have a strong effect on the oxygen absorption properties of the hexagonal manganites. To ultimately determine which properties donor doping with Ti^{4+} introduce in $h-RMnO_3$, the effects of the microstructure and the R-cation must first be isolated and understood.

Since there are so many parameters affecting the performance of oxygen absorption/ desorption in the hexagonal manganites, the risk of falsely ascribing certain properties to e.g. doping is high when evaluating the results. Most of the measurements in this study were only performed once, and with marginal support from the literature, the chance of making wrong conclusions is high. However, the three measuring methods used in this study, i.e. HT-XRD, TGA and DC-conductivity, give a broad view of the same phenomenon.

5.1 General Observations

The two most important aspects of oxygen absorption/desorption performance in the hexagonal rare-earth manganites analyzed in this study are the thermodynamics and kinetics. When evaluating the thermodynamics, oxygen absorption capacity and how temperature affect the capacity are the two most important factors. When evaluation the kinetics, the absorption and desorption rates are the most important factor.

The highest observed oxygen absorption from the TGA measurements for the different

compounds are previously given in Table 4.3. Figure 5.1 summarizes observed oxygen absorption/desorption temperature regions from the different measurements in the study. Table 5.1 summarize the observed temperatures at which the peaks in oxygen absorption are found from the different measuring techniques. Figure 5.2 contains plots from the results that support the temperature regions and peak temperatures given in Figure 5.1 and Table 5.1.

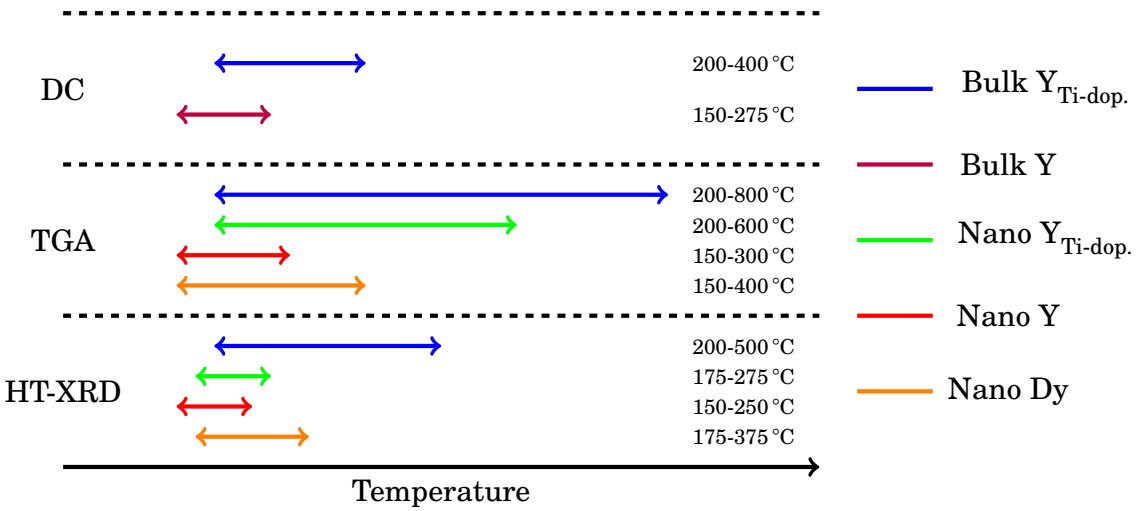

Figure 5.1: A visual representation of the observed temperature regions of oxygen absorption and desorption in various hexagonal manganites. The temperature regions are based on the values in Figure 5.1. The TGA values are most reliable as the change in mass is only due to absorption of oxygen. The DC conductivity and the lattice parameter expansions are affected by temperature, and accurate temperature regions of oxygen absorption/desorption is hence difficult to isolate from the thermal effects.

Table 5.1: Observed temperatures at which the oxygen absorption peaks in various hexagonal manganites by HT-XRD, TGA and DC measurements. HT-XRD,1 indicates the HT-XRD measurements with varying temperature, while HT-XRD,2 indicates the HT-XRD measurements with switching atmosphere.

h−$RMnO_3$	$T_{HT-XRD,1}$ [°C]	$T_{HT-XRD,2}$ [°C]	T_{TGA} [°C]	T_{DC} [°C]
Bulk h−$YMn_{0.85}Ti_{15}O_3$	300	285	340	310
Bulk h−$YMnO_3$	-	-	-	270
Nano h−$YMn_{0.85}Ti_{15}O_3$	195	205	195	-
Nano h−$YMnO_3$	205	185	225	-
Nano h−$DyMnO_3$	235	225	180	-

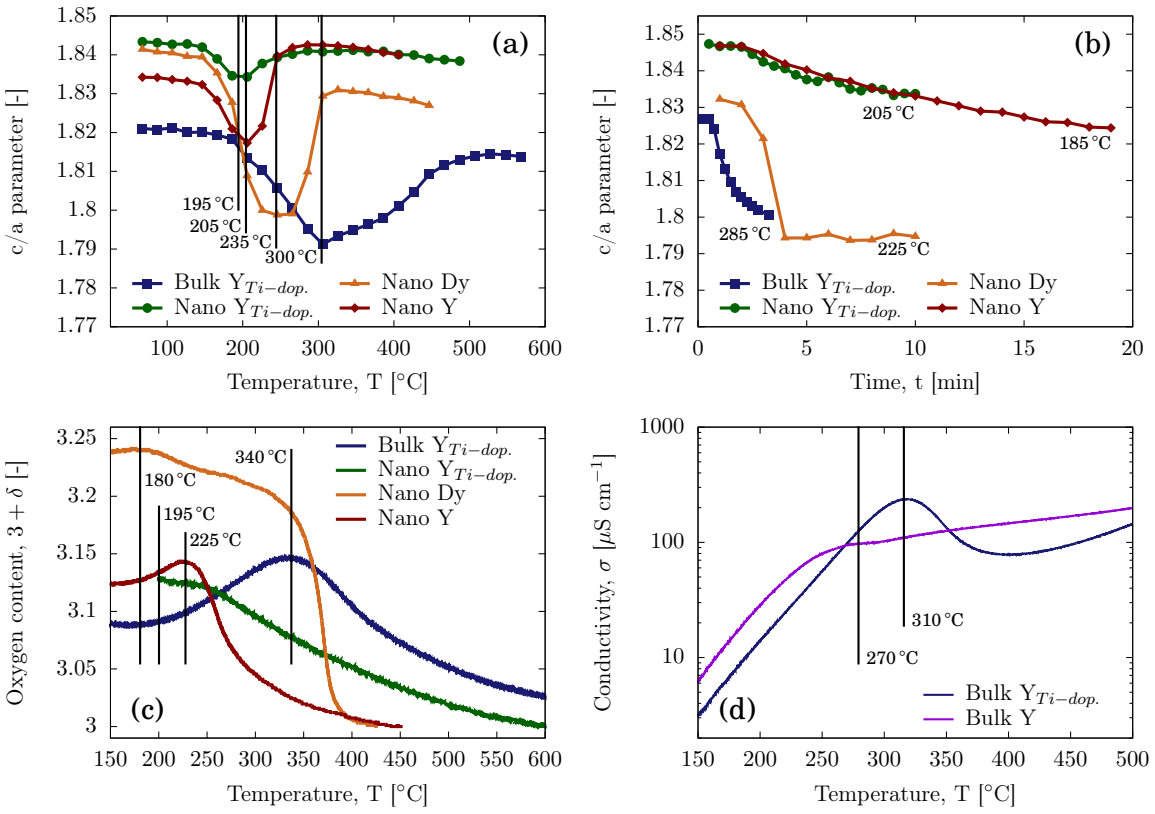

Figure 5.2: Oxygen absorption temperature regions and temperature peaks observed with (a) HT-XRD measurements with varying temperature, (b) HT-XRD measurements with constant temeprature, (c) TGA measurements and (d) DC conductivity measurements.

The kinetic observations in this study were found from the HT-XRD measurements with switching atmosphere and the DC conductivity relaxation measurements. The time to reach equilibrium as a function of temperature for the materials measured with HT-XRD is given in Figure 5.3. The data is based on the measurements given in Figure 4.6-4.8. The smaller plot in Figure 5.3 is an Arrhenius plot, and from the gradients of the regression lines the activation energy for diffusion, E_a, was calculated, see Table 5.2.

In addition to evaluating the thermodynamic and kinetic aspects, the structural change in the rare-earth manganites upon oxygen absorption and desorption is interesting. Relative chemical expansion values for the materials measured with HT-XRD are given in Table 5.3. These values are calculated from the data shown in Figure 4.6 and 4.7. The isothermal data was used to exclude all thermal expansion contributions. Only the largest expansion values for each material are given in Table 5.3.

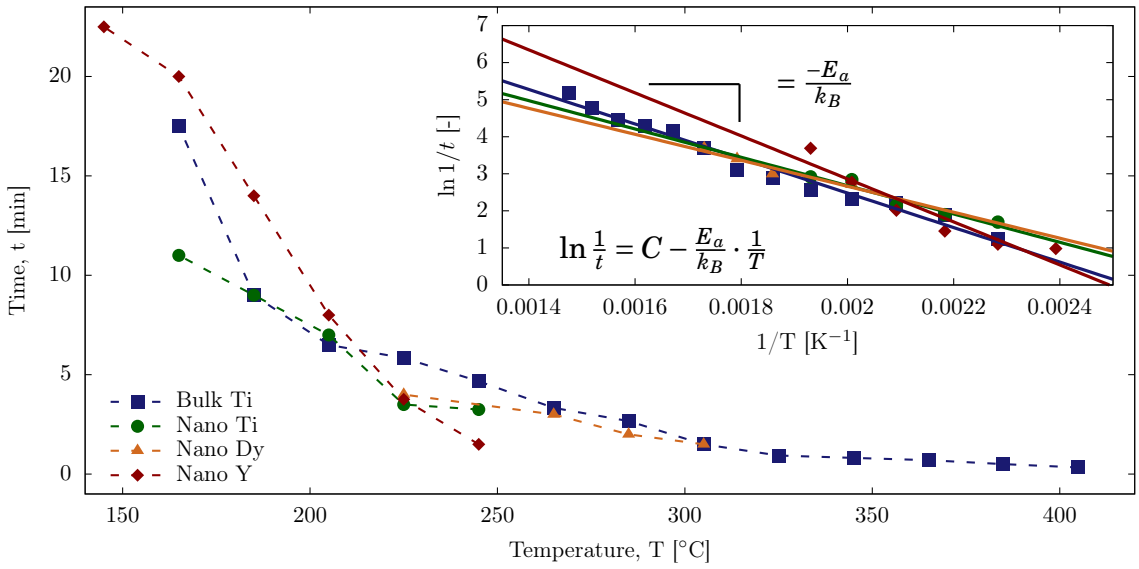

Figure 5.3: The time for various h−$RMnO_3$ powders to reach oxygen absorption equilibrium at different temperatures. The smaller plot is an Arrhenius plot, showing trend lines with gradients equal to $-E_a/k_B$.

Table 5.2: Calculated activation energies, E_a, for diffusion in h−$RMnO_3$. The values are determined from linear regression of the values in the Arrhenius plot in Figure 5.3. The error values for the regressions is included.

h−$RMnO_3$	Activation energy, E_a [eV]	Error, [%]
Bulk h−$YMn_{0.85}Ti_{0.15}O_3$	0.40±0.02	4.89
Nano h−$YMn_{0.85}Ti_{0.15}O_3$	0.33±0.05	15.94
Nano h−$DyMnO_3$	0.30±0.06	19.08
Nano h−$YMnO_3$	0.50±0.08	16.80

Table 5.3: Maximal change in lattice parameter a and c, unit cell volume V, and c/a, when oxidizing the materials. The values are calculated from the isothermal measurements with switching atmosphere from N_2 to O_2. The same values with opposite sign should be obtained if one changed the atmosphere from O_2 to N_2.

h−$RMnO_3$	a	c	c/a	V
Bulk Ti	0.36%	-1.10%	-1.45%	-0.39%
Nano Ti	0.10%	-0.58%	-0.68%	-0.38%
Nano Dy	0.46%	-1.74%	-2.19%	-0.83%
Nano Y	0.34%	-0.87%	-1.20%	-0.19%

Appendix E includes figure showing two and two properties plotted together, better visualizing the dependence of the measured data.

Based on the general trends presented here, the observed differences will be assigned to the three different variables of the compounds tested: The microstructure, the R-cation and donor doping with Ti^{4+}. Based on the evaluation of these variables, the use of h−$YMn_{0.85}Ti_{0.15}O_3$ in oxygen permeable membranes will be shortly discussed. Finally, suggestions to further work will be presented.

5.2 Effect of Microstructure in h−$RMnO_3$

Two types of microstructures were analyzed in this study; nano-sized powder and bulk-sized powder of h−$RMnO_3$. The nano-sized powders ranged from 18.7 nm to 25.5 nm, while the bulk-sized powders had crystallite sizes between 2 µm to 17 µm, see Table 4.1.

From the TGA measurements summarized in Figure 4.9 and 4.10, a larger absorption of excess oxygen is observed in the bulk-sized h−$YMn_{0.85}Ti_{0.15}O_3$ powder ($\delta = 0.177$) compared with the nano-sized h−$YMn_{0.85}Ti_{0.15}O_3$ powder ($\delta = 0.150$). The hysteresis plot of the nano-sized powder shows an almost linear trend with no distinct region of absorption/desorption of oxygen, questioning the validity of these results. However, the measured absorption of oxygen in nano-sized h−$DyMnO_3$ ($\delta = 0.264$) in this study is below reported values of bulk-sized h−$DyMnO_3$, with results well above $\delta = 0.3$ [22]. A comparison of these δ-values are given in Figure 5.4.

Although the value for the bulk-sized h−$DyMnO_3$ was measured using a lower cooling rate, i.e. 0.1 °C min^{-1} compared with 1.0 °C min^{-1} in this study, it is plausible that larger crystallite grains have more tolerance towards non-stoichiometry. Incorporation of oxygen interstitials give a tensile strain in the ab-plane and a compressive strain along the c-axis, see Figure 4.3. As nano-sized crystallites have quite high surface energies and high surface induced strain, the sizes could explain why bulk-sized particles are more susceptible for defects causing additional strain in the crystal structure.

In his work, Østmoe [9] reported a linear relationship between the crystallite sizes of the nano-powders and oxygen absorption, where smaller crystallites gave a larger oxygen absorption capacity. This conclusion is in conflict with the findings in this

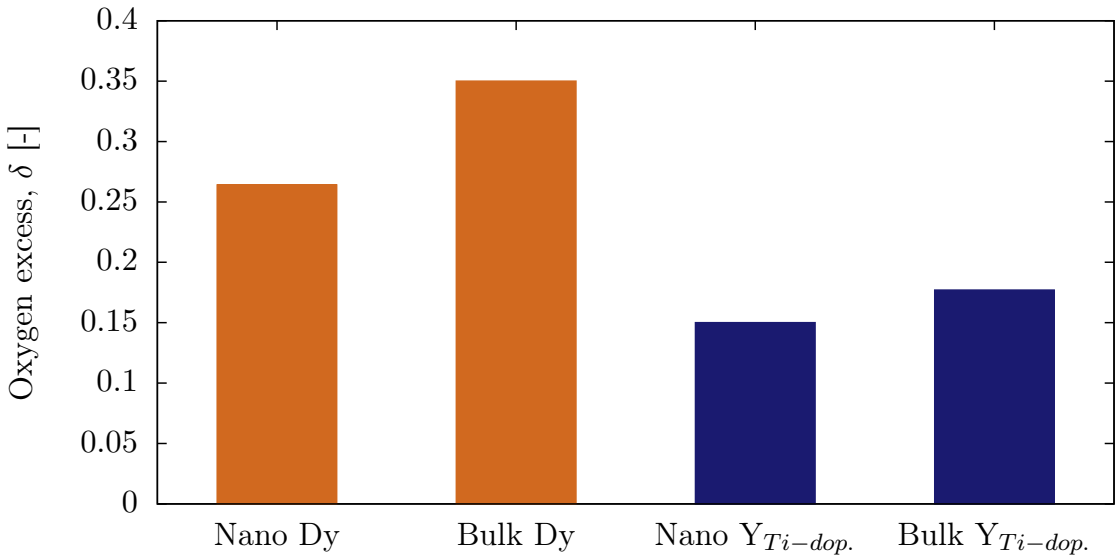

Figure 5.4: Maximal amount of excess oxygen, δ, for bulk- and nano-sized h$-DyMnO_3$ and h$-YMn_{0.85}Ti_{0.15}O_3$. The value for bulk-sized $DyMnO_3$ is taken from Remsen *et al.* [22].

study, where bulk-sized powders have larger oxygen absorption capacities than the nano-sized powders. However, only one crystallite size of each nano-sized powder were tested in this study, suggesting that at nano-scale his reported trend is somehow correct, while at bulk-scale the absorption capacity increases again.

In addition to oxygen absorption capacity differences observed between bulk- and nano-sized powders, the kinetics regarding absorption and desorption are quite different. From the HT-XRD measurements with switching atmosphere, nano-sized powders have proven to be superior to the bulk-sized powders in terms of absorption and desorption rates. The only exception here is the bulk-sized Ti-doped h$-YMnO_3$, which will be discussed later.

Both the bulk-sized and 150 nm powder of h$-YMnO_3$ had so slow absorption rates that they were unable to fully oxidize during HT-XRD measurements of 50 and 20 minutes, respectively. The nano-sized powder of h$-YMnO_3$, however, exhibited fast kinetic behavior, reaching equilibrium at all temperatures within 25 minutes. Figure 5.5 illustrates the size dependence of the kinetics, based on the measurements showed in Figure 4.7 and 4.8. The DC conductivity relaxation measurements in Figure 4.14 show a somewhat faster absorption rate of bulk-sized h$-YMnO_3$, suggesting that the change in lattice parameters during oxidation is too small to detect, see Figure 5.6.

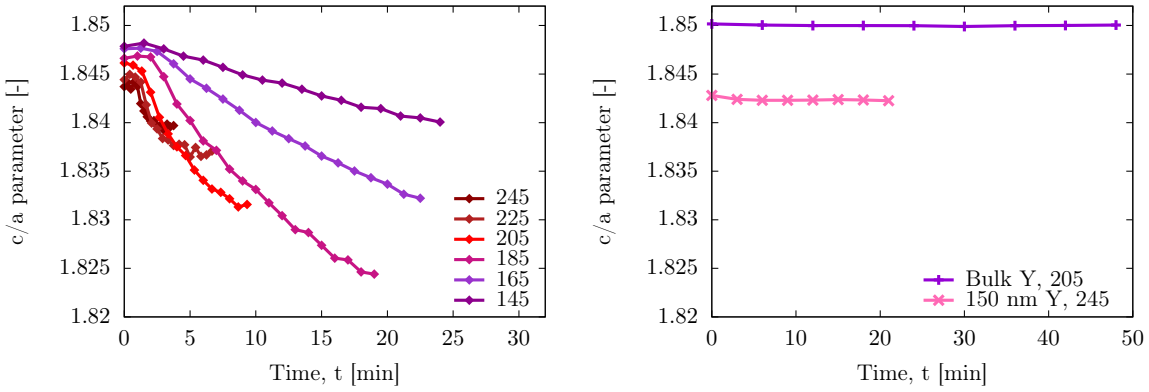

Figure 5.5: c/a parameter of nano-sized h−$YMnO_3$ (left) and bulk- and 150 nm-sized h−$YMnO_3$ (right) at various temperatures when switching from N_2 to O_2.

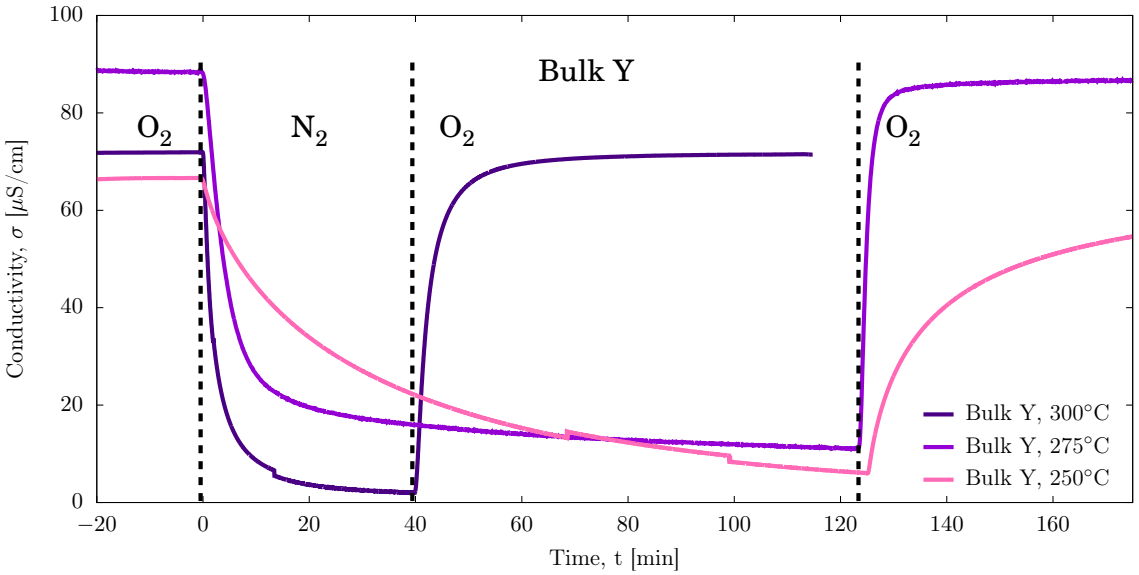

Figure 5.6: DC conductivity in bulk-sized h−$YMnO_3$ when switching atmosphere between O_2 and N_2. The measurements for h−$YMnO_3$ at 250 °C and 300 °C are performed by Nesdal [11].

Independent on the HT-XRD measurements of bulk-sized and 150 nm-sized powders, faster kinetics are observed for the nano-sized powder of h−$YMnO_3$. These results suggests surface exchange to be the rate determining step when oxidizing h−$RMnO_3$, as the nano-sized powders have a much larger surface area.

5.3 Effect of R-cation in h−$RMnO_3$

Two different R-cations were analyzed in this study; yttrium (Y) and dysprosium (Dy). Dy^{3+} has a slightly larger ionic radius than Y^{3+} when 7 coordinated, i.e. 0.97 Å for Dy^{3+} compared with 0.96 Å for Y^{3+}, see Figure 5.7. Their electronegativity, χ, is equal, namely 1.22 by the Pauling scale. Dy^{3+} is a $5d$ element with empty $5d$ orbitals, while Y^{3+} is a $4d$ element with empty $4d$ orbitals. Despite the similarities between Y^{3+} and Dy^{3+}, the results in this study and other studies [21, 22] indicate a clear difference in oxygen absorption capacities and absorption rate between the manganites of the two.

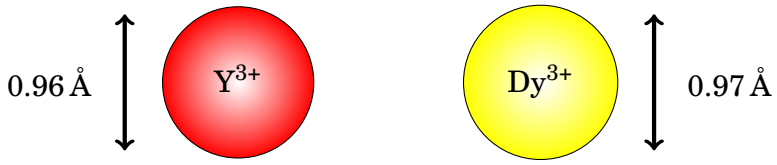

Figure 5.7: Ionic sizes of h−$YMnO_3$ (blue) and h−$DyMnO_3$ (red) relative to each other. Although the size difference appears to be small, it might have a big effect on the properties in the material.

The difference in oxygen absorption capacities for h−$YMnO_3$ and h−$DyMnO_3$ is illustrated in Figure 5.4. The temperature region of oxygen absorption and desorption is found to be slightly shifted to higher values for h−$DyMnO_3$ compared to h−$YMnO_3$ in the TGA and HT-XRD measurements, see Figure 5.1.

Both the TGA measurements and the HT-XRD measurements prove h−$DyMnO_3$ to have a faster absorption/desorption rate than h−$YMnO_3$. The difference in oxygen absorption/desorption rate can be seen in Figure 5.3, resulting in a large difference in calculated activation energy of diffusion, E_a, see Table 5.2.

The differences in absorption capacities for h−$YMnO_3$ and h−$DyMnO_3$ is supported by other studies [22, 27], although Østmoe [9] reported no difference between the nano-sized powders of the compounds. A comparison of absorption rate for nano-sized h−$YMnO_3$ and h−$DyMnO_3$ is not reported in literature.

A plausible explanation for the observed kinetic and thermal stabilization differences between h−$YMnO_3$ and h−$DyMnO_3$ is the size of the Dy^{3+}-cation. Since 7 coordinated Dy^{3+} has a larger ionic radius than 7 coordinated Y^{3+}, Dy^{3+} is expected to expand the crystal structure. This is confirmed in the XT-XRD measurements in inert atmosphere (N_2) in Figure 4.4, where both the a and c parameter of h−$DyMnO_3$ are larger than

the lattice parameters in h−$YMnO_3$, despite the h−$YMnO_3$ powder having smaller crystallite sizes. An expansion in the Dy^{3+} layer in the structure would also expand the MnO_5 layer, thus giving more room for the interstitial oxygen in the structure, see Figure 5.8. This could induce a faster diffusion rate within the crystals.

The structural HT-XRD measurements do not explain the observed increase in oxygen absorption capacity in h−$DyMnO_3$. A plausible explanation is the 5*d* orbitals of Dy^{3+}. The 5*d* orbitals of Dy^{3+} have a larger extent than the 4*d* orbitals of Y^{3+}, and could somehow help stabilizing higher amounts of interstitial oxygen and help charge stabilizing the interstitial oxygen during diffusion. However, studies have shown that mixed compounds of both Y and Dy, $Dy_{1-x}Y_xMnO_3$, improve the absorption capacity compared to the pure materials [22, 23], suggesting that the explanation is more complex than just orbital extension.

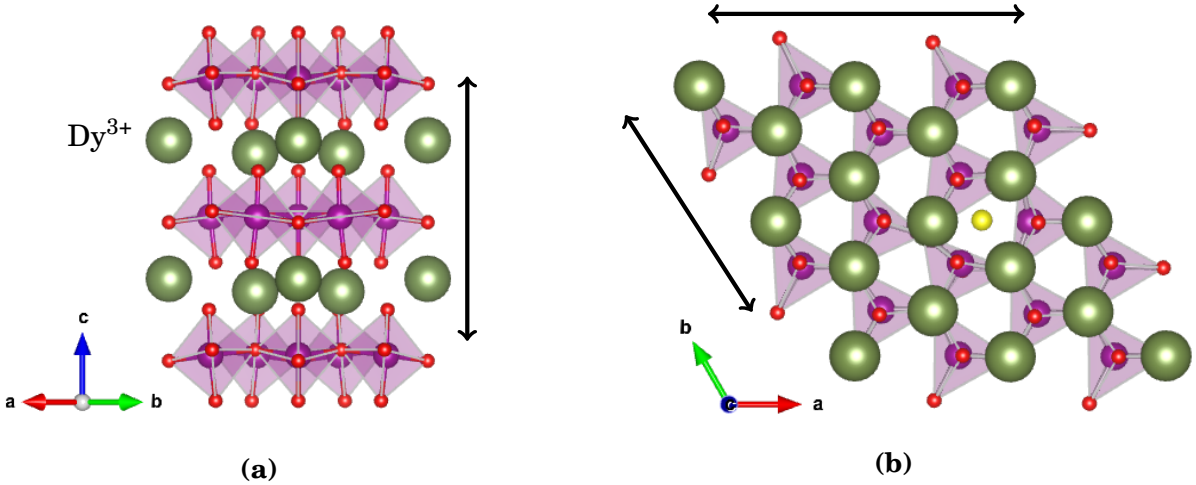

Figure 5.8: The crystal structure h−$DyMnO_3$ with proposed expansion (a) along the c-axis and (b) in the ab-plane compared to h−$YMnO_3$. The expansion of the crystal structure could explain the higher oxygen absorption capacity and the faster kinetics of h−$DyMnO_3$ relative to h−$YMnO_3$. The structures are created with the VESTA software [30].

5.4 Effect of Ti^{4+} Doping in h−$RMnO_3$

As seen from the results in this study, donor doping with Ti^{4+} in h−$YMnO_3$ affect several properties in the parent compound. Here, the evaluation of the effects of Ti-doping is divided into three subsections, i.e. the structural effects, the thermodynamic effects and the kinetic effects. Although the effects are different, the proposed explanations

overlap somehow. In short, the effects of Ti-doping is either due to simple charge doping or due to the Ti^{4+}-ions themselves. Separation of the two can be difficult, as no measurements with other donor dopants was performed. Suggestions to isolate which effects can be ascribed to the charge doping and the Ti^{4+} ions will be discussed in Section 5.7 Further Work.

As mentioned in the Literature Review, donor doping with Ti^{4+} can be charge compensated in two ways; reduction of Mn^{3+} to Mn^{2+} in low pO_2, or absorption of interstitial oxygen in high pO_2, see Equation 5.1 and 5.2, respectively.

$$TiO_2 + \frac{1}{2}Mn_2O_3 \xrightarrow{h-RMnO_3} Ti_{Mn}^{\bullet} + Mn_{Mn}^{'} + 3O_O^x + \frac{1}{4}O_{2(g)} \tag{5.1}$$

$$TiO_2 + \frac{1}{2}R_2O_3 \xrightarrow{h-RMnO_3} R_R^x + Ti_{Mn}^{\bullet} + 3O_O^x + \frac{1}{2}O_i^{''} \tag{5.2}$$

The mechanisms presented in Equation 5.1 and 5.2 directly or indirectly affect all of the effects from doping with Ti^{4+}. The mechanisms are confirmed through the Seebeck coefficient measurements, see Section 5.5 Conductivity Considerations.

5.4.1 Structural Effect

The Ti^{4+} ion is considerable smaller than the Mn^{3+} ion, with an ionic radius of 0.51 Å compared to 0.58 Å of Mn^{3+} when 5 coordinated, see Figure 5.9. Figure 5.10 summarize the lattice parameter changes in O_2 and N_2 from the HT-XRD measurements.

When Ti^{4+} is charge compensated with reduction of Mn^{3+} to Mn^{2+}, see Equation 5.1, the structural effect by the smaller size of the Ti^{4+} ion on the Mn^{3+} site can be considered canceled by the larger size of the accompanied Mn^{2+} ion. Since the Mn^{2+} ion has a larger deviation from the size of the Mn^{3+} ion than the Ti^{4+} ion, the structural parameters might even expand when Ti^{4+} is introduced. The HT-XRD measurements in N_2 confirms this, as the a and c paramter of the Ti-doped bulk- and nano-sized powders are not particularly different from the undoped compounds, see Figure 4.4 and

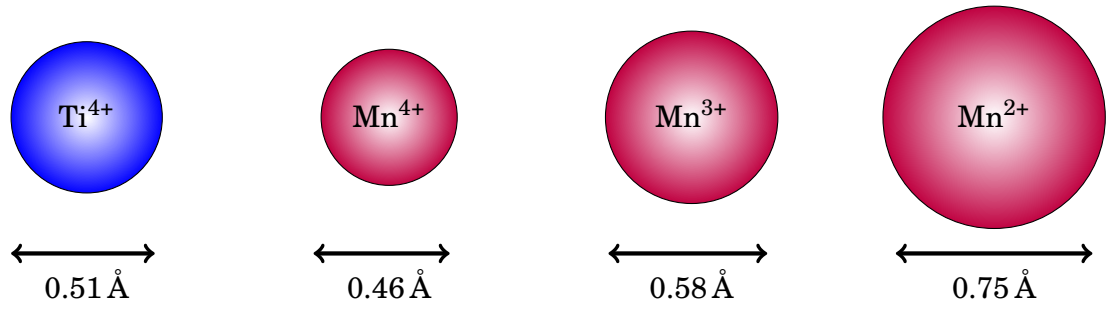

Figure 5.9: Relative sizes of Ti^{4+}, Mn^{4+}, Mn^{3+} and Mn^{2+}. The size of Mn^{4+} is an interpolation between coordination number 4 and 6.

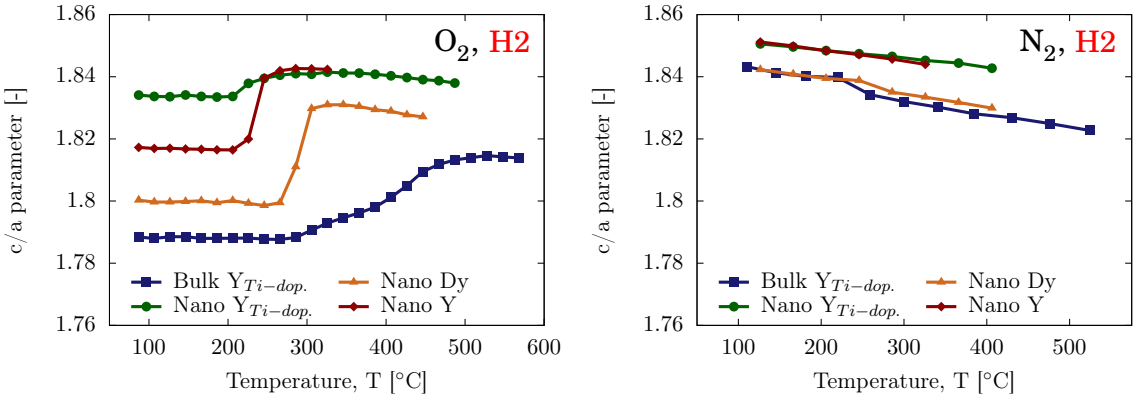

Figure 5.10: c/a parameter from the HT-XRD measurements in O_2 (left) and N_2 (right). Both plots show the lattice parameter from heating cycle 2.

5.10. The differences between the nano- and bulk-sized h−$YMn_{0.85}Ti_{0.15}O_3$ powders can be explained by lattice expansions when decreasing the crystallite size of an ionic compound [63].

When Ti^{4+} is charge compensated by interstitial oxygen, see Equation 5.2, there are no species to compensate the small Ti^{4+} ion on the Mn^{3+} site. Thus, the structure contracts along the c-axis, and expands in the ab-plane. This is seen for bulk-sized h−$YMn_{0.85}Ti_{0.15}O_3$ in Figure 4.3 and 5.10. The nano-sized h−$YMn_{0.85}Ti_{0.15}O_3$ powder deviates from this theory by having both the a and the c parameter larger than the undoped h−$YMnO_3$ powder. This can be explained by the smaller crystallites in the Ti-doped nano-powder compared with the nano-sized h−$YMnO_3$ powder, or that the Ti-doped nano-powder is not fully crystalline.

The HT-XRD measurements show that the thermal expansion rates are equal for all the materials tested, see N_2-plots in Figure 4.4 and 5.10. The linear thermal

expansion coefficients along the a parameter for the compounds is calculated to be $\sim 2.3 \times 10^{-5}\,K^{-1}$, using Equation 2.25. These thermal expansion coefficients are somewhat larger than reported values of $\sim 5 \times 10^{-6}\,K^{-1}$ for h$-YMnO_3$ [22]. The difference in lattice parameter size for these materials is due to two factors: A decrease in crystallite size gives an increase in lattice parameter size, and Ti-doping elongates the lattice parameters.

The HT-XRD measurements in Table 5.3 reveal that the structural changes in the a and c lattice parameter during reduction and oxidation is much lower in nano-sized h$-YMn_{0.85}Ti_{0.15}O_3$ than for undoped nano-sized $YMnO_3$. This difference is very clear in Figure 5.10 and C.1; at elevated temperatures, in the region with no interstitial oxygen, the values of c/a are the same. But when oxidized at lower temperatures the lattice parameters for $YMnO_3$ undergo a much larger change than the lattice parameters of h$-YMn_{0.85}Ti_{0.15}O_3$. Somehow Ti^{4+} stabilizes the structure to tolerate a shorter c parameter, since TGA measurements show that the Ti-doped nano-sized powder absorbs nearly equal the amount of oxygen than the undoped powder.

Bulk-sized h$-YMn_{0.85}Ti_{0.15}O_3$ has a relative large lattice parameter change during chemical expansion compared to nano-sized h$-YMn_{0.85}Ti_{0.15}O_3$. This is interesting, and may be due to the fact that the lattice parameters in the nano-sized crystals are under so much strain that they simply can not be pushed any further. No data on chemical expansion of undoped bulk-sized $YMnO_3$ was obtained due to the slow kinetics of these powders, but based on the aforementioned theory one would expect an enormous change in lattice parameter size for bulk-sized $YMnO_3$.

Annealing of the nano-sized h$-YMn_{0.85}Ti_{0.15}O_3$ was tried during the study, and at first it was believed that the coarsening was slowed down by the Ti-doping. After reference measurements on nano-sized $YMnO_3$, see Appendix F, this theory was ruled out.

5.4.2 Thermodynamic Effect

Based on Equation 5.1 and 5.2, donor doping with Ti^{4+} should increase the absorption capacity of the hexagonal rare-earth manganites, as charge compensation of O_i'' can happen in two steps (Mn^{2+} - Mn^{3+} - Mn^{4+}), see Equation 5.3. In theory, donor doping should increase the oxygen absorption capacity by half of the doping concentration, see Equation 5.4, as long as the crystal structure can tolerate it.

$$x\mathrm{TiO}_{2(s)} + \mathrm{h{-}YMnO}_{3(s)} = \mathrm{Y(Mn}^{3+}_{1-x}\mathrm{Mn}^{2+}_{x})(\mathrm{Ti}^{4+}_{x})\mathrm{O}_{3(s)} + x\mathrm{O}_{2(g)} \tag{5.3}$$

$$C_{\mathrm{O}''_i} = C_{\mathrm{O}''_i eq.\mathrm{YMnO}_3} + \frac{1}{2}C_{\mathrm{Ti}^{+}_{4}} \tag{5.4}$$

The TGA measurements in this study show no increase in oxygen absorption capacity for the Ti-doped bulk- and nano-sized powder compared to the undoped powders, see Table 4.3. There are several explanations for this. The unexpected behavior can be explained by the measuring technique, where a too fast temperature rate in the TGA measurements for the bulk-sized h−$YMn_{0.85}Ti_{0.15}O_3$ powder was used, hindering the powder to be saturated with oxygen. It might also be a problem with the nano-sized h−$YMn_{0.85}Ti_{0.15}O_3$ powder being somewhat amorphous. It might also be that donor doping with Ti^{4+} lower the structural tolerance for large amounts of excess oxygen.

The HT-XRD measurements show that Ti-doping in the *bulk*-sized powder stabilize an excess oxygen content to higher temperatures, see Figure 5.1, with an oxygen absorption peak around 100 °C higher for the bulk-sized h−$YMn_{0.85}Ti_{0.15}O_3$ powder compared to the nano-sized h−$YMnO_3$ powder, see Table 5.1. The temperature region of oxygen absorption and desorption also broadens with Ti-doping in the bulk-sized powder, suggesting that the interstitial oxygen is both entropy stabilized and to some degree entropy stabilized towards elevated temperatures. The temperature region was measured to shift 500 °C up in temperature for the bulk-sized Ti-doped powder compared to the undoped nano-sized h−$YMnO_3$ powder.

This temperature region for the Ti-doped *nano*-sized h−$YMnO_3$, however, seems to be more similar to that of pure nano-sized h−$YMnO_3$, although the trend of temperature region broadening is seen in both the HT-XRD and the TGA measurements. The oxygen absorption peak is fairly similar for nano-sized h−$YMn_{0.85}Ti_{0.15}O_3$ and h−$YMnO_3$, but the temperature region was measured to shift 300 °C up in temperature compared to the undoped nano-sized h−$YMnO_3$ powder.

The higher degree of entropy stabilization of interstitial oxygen in the Ti-doped powders can be explained by the larger a parameter in these compounds, see Figure 5.11.

Both the bulk- and nano-sized h−$YMn_{0.85}Ti_{0.15}O_3$ powder have larger a parameters than nano-sized $YMnO_3$, resulting in an expanded ab-plane where the oxygen interstitials are located. This seems to be favorable for the interstitial oxygen, as the distance to the other oxygen ions in the structure increases, causing less electrostatic repulsion. Since Ti^{4+} seems to affect the lattice parameters in the *bulk*-sized h−$YMn_{0.85}Ti_{0.15}O_3$ powder more than the lattice parameters in the *nano*-sized powder, the stabilization effect is thus stronger in the *bulk*-sized powder.

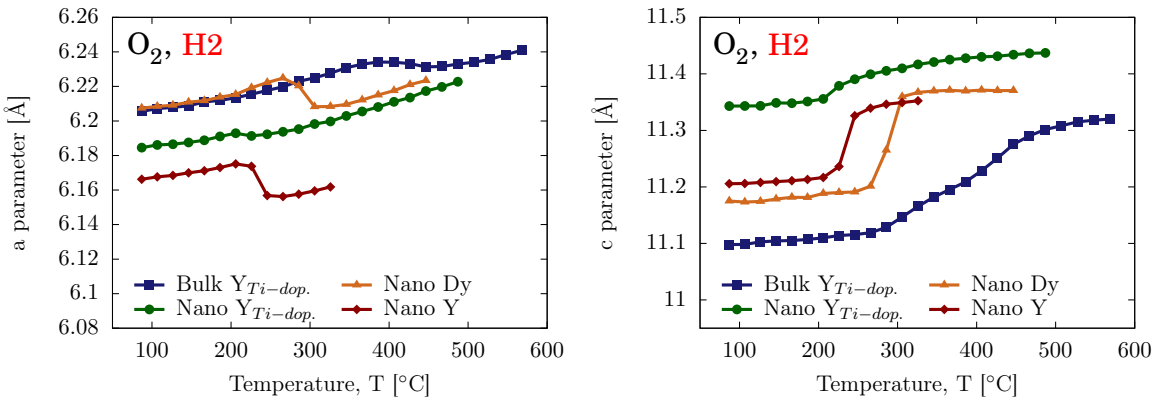

Figure 5.11: HT-XRD measurements of the a (left) and c () parameter from heating cycle 2 in O_2.

As seen in Figure 5.11, nano-sized $DyMnO_3$ and the bulk-sized h−$YMn_{0.85}Ti_{0.15}O_3$ have a parameters of equal length. However, the bulk-sized h−$YMn_{0.85}Ti_{0.15}O_3$ powder have shorter c parameters, suggesting extra stabilization of the negatively charged oxygen interstitials by the positively charged Y^{3+}-ions along the c-axis. The expansion in the ab-plane and the contraction along the c-axis for h−$YMn_{0.85}Ti_{0.15}O_3$ is visualized in Figure 5.12.

The higher degree of entropy stabilization of interstitial oxygen in the Ti-doped powders can also be explained by the general strong bonds between Ti^{4+} and O^{2-}. Since the interstitial oxygen in stabilized by one Ti^{4+} ion and one Mn^{4+} in the Ti-doped powders, see Figure 5.13, the oxygen ion can be stabilized by forming a strong ionic bond.

The observed stabilization of excess oxygen by Ti^{4+} is confirmed in unpublished DFT-calculations on the department [64].

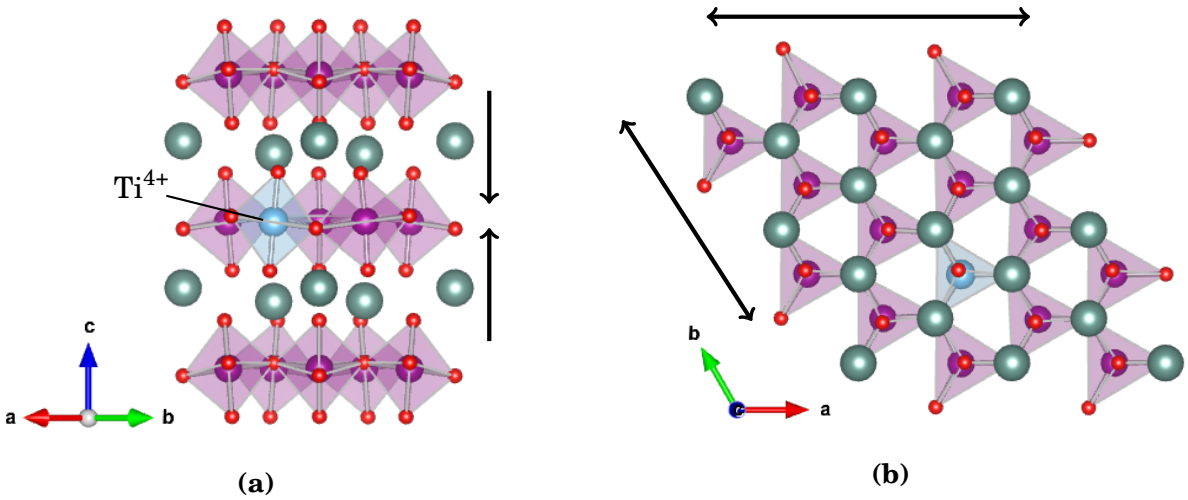

Figure 5.12: The crystal structure h−$YMn_{0.85}Ti_{0.15}O_3$ with proposed contraction (a) along the c-axis and expansion (b) in the ab-plane when oxidized compared to h−$YMnO_3$. The expansion of the crystal structure could explain the stabilization of interstitial oxygen and the faster kinetics in h−$YMn_{0.85}Ti_{0.15}O_3$ relative to h−$YMnO_3$. The structures are created with the VESTA software [30].

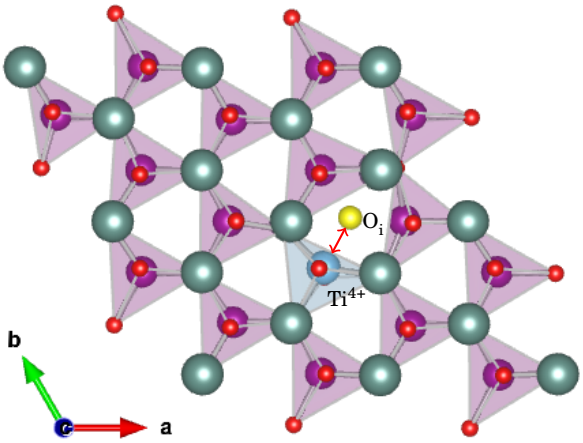

Figure 5.13: h−$YMn_{0.85}Ti_{0.15}O_3$ with interstitial oxygen (yellow) viewed along the c-axis. The TiO_5 polyhedron is marked with blue. The stabilizing bond between Ti^{4+} and O_i^{2-} is marked with a red arrow.

5.4.3 Kinetic Effect

The HT-XRD measurements with switching atmosphere show excellent kinetics for the Ti-doped bulk-powder compared to the undoped bulk-powder of h−$YMnO_3$, see Figure 5.14. Also compared with the nano-sized powders analyzed, the bulk-sized

h−$YMn_{0.85}Ti_{0.15}O_3$ powder perform well, as seen in Figure 5.3.

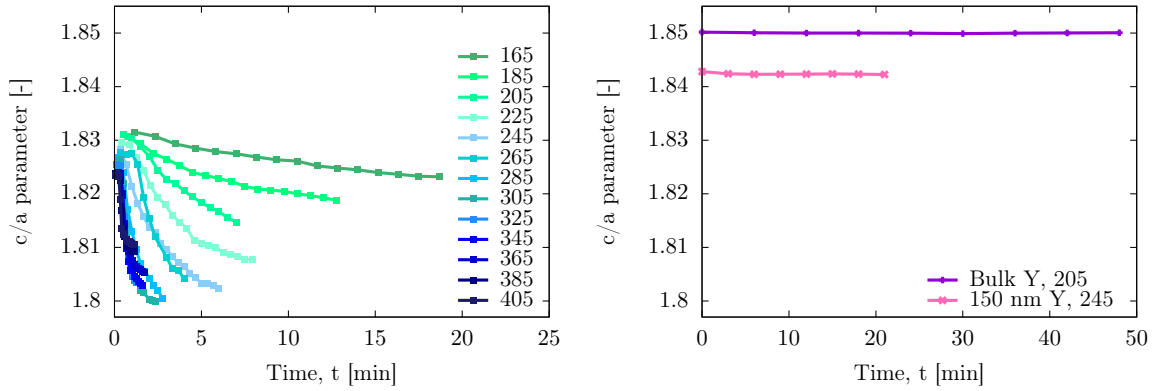

Figure 5.14: c/a parameter of bulk-sized h−$YMn_{0.85}Ti_{0.15}O_3$ (left) and bulk- and 150 nm-sized h−$YMnO_3$ (right) at various temperatures when switching from N_2 to O_2.

The calculated activation energy for diffusion for the Ti-doped powders are relatively low, and lies between the values of the nano-sized undoped powders, see Table 5.2. The calculated activation energies in Table 5.2 probably underestimate the real values, as equilibrium was not reached for all temperatures during the HT-XRD measurements with switching atmosphere, but the values give a relative indication between the powders analyzed. Thus, Ti-doping seems to lower the activation energy for diffusion in the h−$YMnO_3$ system, resulting in enhanced kinetics for the h−$YMn_{0.85}Ti_{0.15}O_3$ powders.

The explanation for the enhanced kinetics in the Ti-doped bulk-powder is similar to that of the thermodynamic behavior described earlier. Since Ti-doping expands the ab-plane in the crystal structure, there is more space for the oxygen interstitials to diffuse to new interstitial sites. The additional contraction along the c-axis enables the Y^{3+} ions to stabilize the interstitial oxygen as it moves to a new site in the structure.

In the DC conductivity relaxation measurements, however, the h−$YMn_{0.85}Ti_{0.15}O_3$ sample seems to have a slower oxidation rate than the bulk-sized h−$YMnO_3$ sample, see Figure 4.14. Although it seems like the DC conductivity relaxation measurements contradict the HT-XRD measurements, there is a simple explanation for the seemingly slow kinetics regarding the conductivity measurements of h−$YMn_{0.85}Ti_{0.15}O_3$: The DC conductivity relaxation measurements only show conductivity, not oxygen absorption. Since the absorption of oxygen in h−$YMn_{0.85}Ti_{0.15}O_3$ affect the conductivity in two steps, namely by first reducing Mn^{2+} to Mn^{3+} and then Mn^{3+} to Mn^{4+}, the kinetics seem slow.

5.5 Conductivity Considerations

As mentioned in the Literature Review, both a change in the temperature and oxidation of the manganese ions will affect the conductivity in the hexagonal rare-earth manganites. In addition to this, donor doping with Ti^{4+} will affect the conductivity. Some studies have looked at the conductivity in the h−$RMnO_3$ material class [8, 50–58], but none directly as both a function of oxygen absorption and donor doping.

As seen from the DC conductivity measurements in Figure D.1 and 4.12, the absorption and desorption of oxygen has an effect, but the impact is small compared to the thermal effect at elevated temperatures. In both $YMnO_3$ and h−$YMn_{0.85}Ti_{0.15}O_3$ an increase in conductivity is observed when the materials are oxidized, but as the Seebeck measurements show, the origin for the conductivities are not completely similar.

$YMnO_3$ is initially a semiconductor with low concentrations of Mn^{4+} due to impurities. As oxygen is absorbed, the manganese ions are oxidized from Mn^{3+} to Mn^{4+}, see Equation 2.10. The Mn^{4+} ions, or $Mn_{Mn}^{\bullet}$, then serve as positive charge carriers ($Mn_{Mn}^{\bullet}$ = Mn^{3+} + $h^{\bullet}$). This increases the number of mobile charge carriers, and thus increases the conductivity. For the temperature regions above the red-ox gap and small partial pressures of O_2 one would expect oxygen vacancies to form in $YMnO_3$, following Equation 2.12, thus giving $Mn_{Mn}^{'}$ ($Mn_{Mn}^{'}$ = Mn^{3+} + $e^{'}$) and electrons as the major charge carrier. However, the measured Seebeck coefficients, given in Figure 4.16, are always positive, suggesting these measurements to be inaccurate. Other measurements at the department have shown the transition from p- to n-type conductivity in $YMnO_3$ due to formation of oxygen vacancies [47], supporting that the measurements in this study is inaccurate.

h−$YMn_{0.85}Ti_{0.15}O_3$ is initially donor doped with Ti^{4+}, giving the material a high concentration of Mn^{2+} ($Mn_{Mn}^{'}$), see Equation 2.18. Before oxidized, h−$YMn_{0.85}Ti_{0.15}O_3$ is thus an n-type conductor with a negative Seebeck coefficient. When oxidizing this material, Mn^{2+} is gradually reduced back to Mn^{3+}. At a certain point, i.e. when the concentration of $O_i^{''}$ exceeds the doping concentration, Mn^{3+} will be oxidized further to Mn^{4+}. Here, the h−$YMn_{0.85}Ti_{0.15}O_3$ will go from a negative to a positive Seebeck coefficient and be a p-type conductor. This shift from n- to p-type semiconductor is clearly seen in Figure 4.17. Thus, it is shown that h−$YMn_{0.85}Ti_{0.15}O_3$ can both be a p-type and an n-type conductor, depending on the thermal and atmospheric history. A combined

plot of the DC conductivity and the Seebeck coefficient as a function of temperature is given in Figure 5.15. A Brouwer diagram illustrating the shift into the p-type region is given in Figure 5.16.

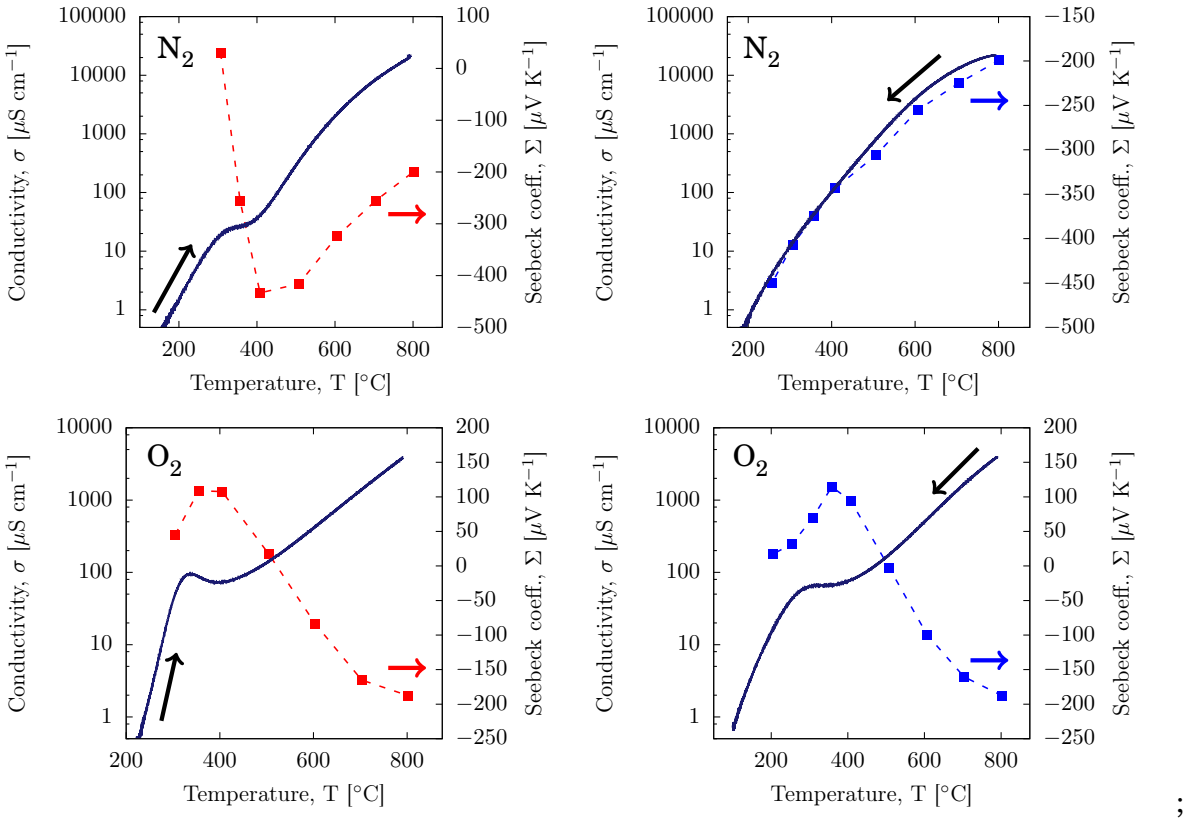

Figure 5.15: DC and Seebeck coefficient as a function of temperature in bulk-sized h−$YMn_{0.85}Ti_{0.15}O_3$. The top plots are measurements conducted in N_2, and the bottom plots are measurements conducted in O_2. The left plots are measurements during heating, and the right plots are measurements during cooling.

The correlation between the DC conductivity and the Seebeck coefficient in Figure 5.15 match perfectly; the Seebeck coefficient is inversely proportional to the DC conductivity, and the switch from positive to negative values of the Seebeck coefficient match exactly with the measured DC conductivity changes at oxygen absorption and desorption.

Unpublished DOS calculations on pure h−$YMnO_3$ and h−$Y_{1-x}A_xMn_{1-y}B_yO_3$ with various dopants (A, B) have been conducted at the department [64]. The calculations include donor doping with Ti^{4+}, and the calculated densities of states for h−$YMnO_3$ and 4.167% Ti-doped h−$YMnO_3$ are given in Figure G.1-G.3 in Appendix G. The DOS cal-

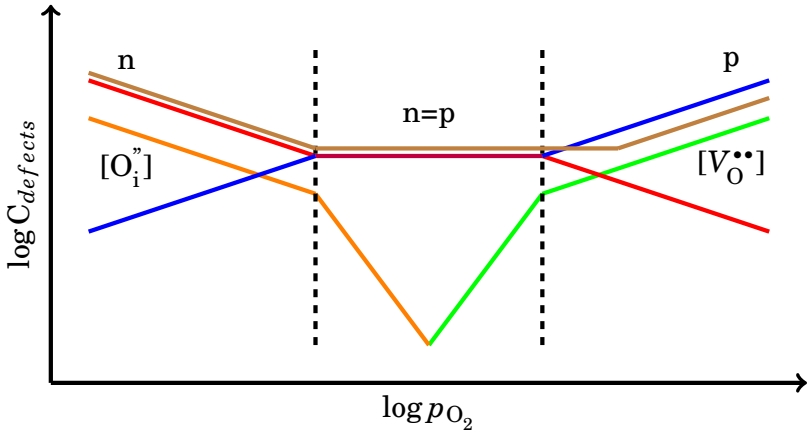

Figure 5.16: A schematic Brouwer diagram illustrating the effect of donor doping with Ti^{4+}, following the brown line. At low partial pressures of oxygen the doped material is an n-type conductor, while at high partial pressures it is a p-type conductor. The region of mixed n- and p-type conductivity (n=p) is elongated into the p-type region due to the doping.

culations in Figure G.1 confirms the relatively large band gap in stoichiometric $YMnO_3$ of 1.6 eV. In addition to this, the calculations reveal that the $3d$ orbitals of Ti^{4+} are too high in energy to contribute to the pure electric conductivity in the material, see Figure G.2 and G.3.

The conductivities observed at 500 °C, given in Table 4.4, can be explained by the doping with Ti^{4+}. In N_2, h−$YMn_{0.85}Ti_{0.15}O_3$ will have a much higher conductivity than $YMnO_3$ due to the high concentration of Mn^{2+} from the donor doping compared with the low concentration of Mn^{4+} from impurities in $YMnO_3$.

In O_2 at the given temperature, h−$YMn_{0.85}Ti_{0.15}O_3$ is partly oxidized by O_i, giving a net concentration of Mn^{2+} or Mn^{4+} around 0. This is confirmed from the Seebeck measurements, as the Seebeck coefficient has a turning point from positive to negative value around this temperature. $YMnO_3$, however, has a small concentration of Mn^{4+} from impurities and some oxidation, resulting in a slightly higher conductivity than h−$YMn_{0.85}Ti_{0.15}O_3$.

5.6 h−$RMnO_3$ in Oxygen Permeable Membranes

The main motivation for this study is to evaluate the performance of Ti-doped hexagonal rare-earth manganites for use in oxygen permeable membranes. From the findings

in this study, h$-YMn_{0.85}Ti_{0.15}O_3$ is in many ways better suited as a membrane material for oxygen separation than stoichiometric h$-YMnO_3$.

The broad temperature region of oxygen absorption and desorption enables a membrane of h$-YMn_{0.85}Ti_{0.15}O_3$ to work at a wide interval, rather than just a narrow temperature gap. The excellent kinetics of the bulk-sized h$-YMn_{0.85}Ti_{0.15}O_3$ powder also suggest that the need for nano-sized crystals in the membrane is less relevant, as the bulk-sized crystals can yield a high O_2 flux at rates close to the nano-sized crystals.

The shift in oxygen absorption peak to a higher temperature, however, means that a higher operating temperature for the membrane is required compared to the nano-sized, stoichiometric alternatives. It might as well be a problem with oxygen interstitials being too stable in the h$-YMn_{0.85}Ti_{0.15}O_3$ membrane structure, requiring a higher pressure difference across the membrane to move oxygen through. This will have to be investigated by preparing and testing of membranes with and without Ti-doping.

5.7 Further Work

Although the findings in this study is interesting, further work is required on the hexagonal rare-earth manganites to be able to explain their behavior during oxidation and reduction by O_2, and to pin point which effects of Ti-doping are due to charge doping and which effects are due to the titanium ions themselves.

The measurements used in this study should be revisited with a nano-sized Ti-doped powder with larger crystallite sizes. New results here could answer if the findings in this study are due to somewhat amorphous powder or if the observed trends are correct. It is suspected that the performance of the nano-crystalline h$-YMn_{0.85}Ti_{0.15}O_3$ in this study is not representative to the behavior to the completely crystalline powders of the compound. This suspicion is supported by the steeper growth rate at the first annealing of the powder compared to annealing of stoichiometric h$-YMnO_3$, see Appendix F. If one can successfully combine the kinetic properties of the nano-sized powders with the thermodynamic properties of Ti-doping, the result would truly stand out as a remarkable substitute to the perovskite membranes on the marked.

To isolate which effects of Ti-doping are due to charge doping and which effects are

due to the titanium ions themselves can be determined by donor doping with another element, e.g. Zr^{4+} on the Y-site (A-site) in the structure. By doing so, one can isolate which effects are contributed to the titanium ions and which are just a result of charge doping. In so manner, acceptor doping with divalent ions is also interesting, potentially answering if the predicted doping mechanisms presented in Equation 2.17-2.24 are valid.

In addition to this, simultaneous doping on both the A and B site could be an interesting topic of exploration. This could answer if "double doping" will have a antagonistic, additive or even synergistic effect on the oxygen absorption properties in the hexagonal manganites. The effect of doping concentration should also be studied, to see how the thermodynamic and kinetic behavior of Ti-doping depend on the doping concentration.

In this study, nano-sized $h-DyMnO_3$ exhibited the best oxygen absorption properties, both in terms of oxygen absorption capacity and absorption rate. The oxygen absorption properties in a solid solution of $h-YMnO_3$ and $h-DyMnO_3$, $h-Dy_{1-x}Y_xMnO_3$, has been reported in literature [22, 23], showing promising results on oxygen capacity enhancement. However, donor doping in $h-DyMnO_3$ is not reported. Doping $h-DyMnO_3$ with Ti^{4+} could enhance the already superb properties in the compound.

A somewhat off-topic property of the $h-RMnO_3$ observed in this study, the conductivity, is also an area that should be looked further into. In this study, Ti-doping has proved to change the p-type conductivity in $h-YMnO_3$ to a multi type conductor of both n and p depending on the thermal and atmospheric history. Again, donor doping on the A-site and acceptor doping is highly relevant when exploring these properties.

Chapter 6

Conclusion

The effect of donor doping with 15% Ti^{4+} in h$-YMnO_3$ on the oxygen absorption and desorption properties in the material was studied by HT-XRD, TGA, DC conductivity and Seebeck coefficient measurements. Nano- and bulk sized powders of h$-YMn_{0.85}Ti_{0.15}O_3$ were compared to nano-sized powders of undoped h$-YMnO_3$ and h$-DyMnO_3$ in the HT-XRD and TGA measurements. Bulk-sized h$-YMn_{0.85}Ti_{0.15}O_3$ was compared with bulk-sized h$-YMnO_3$ in the DC conductivity and Seebeck coefficient measurements.

Ti-doping proved to enhance the oxygen absorption rate in h$-YMnO_3$, and to stabilize the absorbed oxygen towards higher temperatures. The oxygen absorption capacities in the Ti-doped powders did not exceed the capacities in the undoped powders.

Although Ti-doping enhanced some of the oxygen absorption properties in h$-YMnO_3$, nano-sized h$-DyMnO_3$ was measured to have both a higher oxygen absorption capacity and a higher absorption rate than the Ti-doped powders.

In the DC conductivity and Seebeck coefficient measurements, transitions between n- and p-type conductivity was proven to depend on the thermal and atmospheric history of h$-YMn_{0.85}Ti_{0.15}O_3$.

Bibliography

[1] The Way Forward - Five Key Actions to Achieve a Low-Carbon Energy Sector. Technical report, International Energy Agency (IEA), 2014.

[2] J. Bugge, S. Kjær, and R. Blum. High-efficiency coal-fired power plants development and perspectives. *Energy*, 31:1437–1445, 2006.

[3] B. J. P. Buhre, L. K. Elliott, C. D. Sheng, R. P. Gupta, and T. F. Wall. Oxy-fuel combustion technology for coal-fired power generation. *Prog. Energy Combust. Sci.*, 31:283–307, 2005.

[4] Jr. Baukal and E. Charles. *Oxygen-enhanced combustion*. CRC Press, 2010.

[5] R. Welford and R. Starkey. *Business and the Environment: A Reader*. Earthscan Publications Limited, Washington DC, 1st edition, 1996.

[6] A. C. Rola and P. L. Pingali. *Pesticides, rice productivity, and farmers' health: an economic assessment*. IRRI CABI, Manila, 1993.

[7] J. M. Calm. Comparative efficiencies and implications for greenhouse gas emissions of chiller refrigerants. *Int. J. Refrig.*, 29:833–841, 2006.

[8] S. M. Selbach, A. N. Lovik, K. Bergum, J. R. Tolchard, M.-A. Einarsrud, and T. Grande. Crystal structure, chemical expansion and phase stability of $HoMnO_3$ at high temperature. *J. Solid State Chem.*, 196:528–535, 2012.

[9] T. Østmoe. Nanomaterials for chemical oxygenstorage (Master thesis). Technical report, 2014.

[10] E. R. Østli. Optimization of chemical composition of novel manganite oxides for oxygen permeable membranes (Master thesis). Technical Report August, 2015.

[11] S. K. Nesdal. Development of hexagonal manganites for use in oxygen permeable membranes (Master thesis). Technical Report June, 2013.

[12] M. M. Frydenlund. Development of a new class of oxygen ion mixed conductors (Master thesis). Technical Report June, 2014.

[13] C. Blom. Development of a New Class of Materials for Oxygen Storage and Oxygen Ion Conduction (Master thesis). Technical report, 2013.

[14] M. Reidulff. Phase Stability and Point Defects in $InMnO_3$ (Master thesis). Technical Report December, 2014.

[15] S. M. Hoggen. Development of oxygen-permeable membranes based on hexagonal manganites (project thesis). Technical report, 2016.

[16] R. K. Thakur, R. Thakur, S. Samatham, N. Kaurav, V. Ganesan, and N. K. Gaur. Dielectric, magnetic, and thermodynamic properties of $Y_{1-x}Sr_xMnO_3$ (x = 0.1 and 0.2). *J. Appl. Phys.*, 112:104115, 2012.

[17] H. Satoh, J.-i. Iwasaki, K. Kawase, and N. Kamegashira. High temperature enthalpies and heat capacities of $YbMnO_3$ and $YMnO_3$. *J. Alloys Compd.*, 268:42–46, 1998.

[18] J. A. Alonso, M. J. Martínez-Lope, M. T. Casais, and M. T. Fernández-Díaz. Evolution of the Jahn-Teller distortion of MnO_6 octahedra in $RMnO_3$ perovskites (R = Pr, Nd, Dy, Tb, Ho, Er, Y): A neutron diffraction study. *Inorg. Chem.*, 39:917–923, 2000.

[19] J. A. Alonso, M. J. Martínez-Lope, M. T. Casa, and M. T. Ferna. Evolution of the Magnetic Structure of Hexagonal $HoMnO_3$ from Neutron Powder Diffraction Data. *Chem. Mater.*, 13:1497–1505, 2001.

[20] K. Uusi-Esko and M. Karppinen. Extensive series of hexagonal and orthorhombic $RMnO_3$ (R = Y, La, Sm, Tb, Yb, Lu) thin films by atomic layer deposition. *Chem. Mater.*, 23:1835–1840, 2011.

[21] S. Remsen, B. Dabrowski, O. Chmaissem, J. Mais, and A. Szewczyk. Synthesis and oxygen content dependent properties of hexagonal $DyMnO_{3+\delta}$. *J. Solid State Chem.*, 184:2306–2314, 2011.

[22] S. Remsen and B. Dabrowski. Synthesis and oxygen storage capacities of hexagonal $Dy_{1-x}Y_xMnO_{3+\delta}$. *Chem. Mater.*, 23:3818–3827, 2011.

[23] C. Abughayada, B. Dabrowski, M. Avdeev, S. Kolesnik, S. Remsen, and O. Chmaissem. Structural, magnetic, and oxygen storage properties of hexagonal $Dy_{1-x}Y_xMnO_{3+\delta}$. *J. Solid State Chem.*, 217:127–135, 2014.

[24] O. Parkkima, S. Malo, M. Hervieu, E. Rautama, and M. Karppinen. New $RMnO_{3+\delta}$ (R=Y, Ho; $\delta \approx 0.35$) phases with modulated structure. *J. Solid State Chem.*, 221:109–115, 2015.

[25] K. Zhang, J. Sunarso, Z. Shao, W. Zhou, C. Sun, S. Wang, and S. Liu. Research progress and materials selection guidelines on mixed conducting perovskite-type ceramic membranes for oxygen production. *RSC Adv.*, 1:1661, 2011.

[26] J. Sunarso, S. Baumann, J. M. Serra, W. a. Meulenberg, S. Liu, Y. S. Lin, and J. C. Diniz da Costa. Mixed ionic-electronic conducting (MIEC) ceramic-based membranes for oxygen separation. *J. Memb. Sci.*, 320:13–41, 2008.

[27] C. Abughayada, B. Dabrowski, S. Kolesnik, D. E. Brown, and O. Chmaissem. Characterization of Oxygen Storage and Structural Properties of Oxygen-Loaded Hexagonal $RMnO_{3+\delta}$ (R = Ho, Er, and Y). *Chem. Mater.*, 27:6259–6267, 2015.

[28] H. Kitahata, K. Tadanaga, T. Minami, N. Fujimura, and T. Ito. Ferroelectricity of $YMnO_3$ thin films prepared via solution. *Appl. Phys. Lett.*, 75:719, 1999.

[29] I. Gelard, N. Jehanathan, H. Roussel, S. Gariglio, O. I. Lebedev, G. Van Tendeloo, and C. Dubourdieu. Off-stoichiometry effects on the crystalline and defect structure of hexagonal manganite $RMnO_3$ films (R = Y, Er, Dy). *Chem. Mater.*, 23:1232–1238, 2011.

[30] K. Momma and F. Izumi. VESTA: a three-dimensional visualization system for electronic and structural analysis. *J. Appl. Crystallogr.*, 41, 2008.

[31] A. S. Gibbs, K. S. Knight, and P. Lightfoot. High-temperature phase transitions of hexagonal $YMnO_3$. *Phys. Rev. B - Condens. Matter Mater. Phys.*, 83:1–9, 2011.

[32] K. Bergum, H. Okamoto, H. Fjellvaag, T. Grande, M.-A. Einarsrud, and S. M. Selbach. Synthesis, structure and magnetic properties of nanocrystalline $YMnO_3$. *Dalt. Trans.*, 40:7583–7589, 2011.

[33] B. B. Van Aken, T. T.M. Palstra, A. Filippetti, and N. a. Spaldin. The origin of

ferroelectricity in magnetoelectric $YMnO_3$. *Nat. Mater.*, 3:164–170, 2004.

[34] Kiran Singh, Marie-Bernadette Lepetit, Charles Simon, Natalia Bellido, Stéphane Pailhès, Julien Varignon, and Albin De Muer. Analysis of the multiferroicity in the hexagonal manganite $YMnO_3$. *J. Phys. Condens. Matter*, 25:416002, 2013.

[35] M. Lilienblum, T. Lottermoser, S. Manz, S. M. Selbach, A. Cano, and M. Fiebig. Ferroelectricity in the multiferroic hexagonal manganites. *Nat. Phys.*, (September), 2015.

[36] H. Yokokawa, N. Sakai, T. Kawada, and M. Dokiya. Thermodynamic stabilities of perovskite oxides for electrodes and other electrochemical materials. *Solid State Ionics*, 52:43–56, 1992.

[37] V. M. Goldschmidt. Die Gesetze der Krystallochemie. *Naturwissenschaften*, 14:477–485, 1926.

[38] D. M. Giaquinta and H.-C. zur Loye. Structural Predictions in the ABO_3 Phase Diagram. *Chem. Mater.*, 6:365–372, 1994.

[39] P. Ravindran, A. Kjekshus, H. Fjellvåg, A. Delin, and O. Eriksson. Ground-state and excited-state properties of $LaMnO_3$ from full-potential calculations. *Phys. Rev. B*, 65:064445, 2002.

[40] T. Goto, T. Kimura, G. Lawes, A. P. Ramirez, and Y. Tokura. Ferroelectricity and giant magnetocapacitance in perovskite rare-earth manganites. *Phys. Rev. Lett.*, 92:257201–1, 2004.

[41] Y. Wang, X. Lu, Y. Chen, F. Chi, S. Feng, and X. Liu. Hydrothermal synthesis of two perovskite rare-earth manganites, $HoMnO_3$ and $DyMnO_3$. *J. Solid State Chem.*, 178:1317–1320, 2005.

[42] P. Salvador and T. Doan. Stabilization of $YMnO_3$ in a perovskite structure as a thin film. *Chem. Mater.*, 10:2592–2595, 1998.

[43] A. R. West. *Basic Solid State Chemistry*. Wiley, Chichester, 2nd edition, 1999.

[44] P. W. Atkins and D. F. Shriver. *Shriver and Atkins' Inorganic Chemistry*. Oxford

University Press, Oxford, 5th edition, 2010.

[45] R. Tilley. *Understanding Solids: The Science of Materials*. Wiley, West Sussex, 2nd edition, 2013.

[46] T. Katsufuji, S. Mori, M. Masaki, Y. Moritomo, N. Yamamoto, and H. Takagi. Crystal structure and magnetic properties of hexagonal $R\mathrm{MnO_3}$ (R = Y, Lu, and Sc) and the effect of doping. *Phys. Rev. B*, 64:104419, 2001.

[47] S. H. Skjærvø, E. T. Wefring, S. K. Nesdal, N. H. Gaukås, G. H. Olsen, J. Glaum, T. Tybell, and S. M. Selbach. Interstitial Oxygen as a source of p-type Conductivity in Hexagonal Manganites. *Nat. Commun.*, In review, 2016.

[48] S. Lee, A. Pirogov, M. Kang, K.-H. Jang, M. Yonemura, T. Kamiyama, S.-W. Cheong, F. Gozzo, N. Shin, H. Kimura, Y. Noda, and J.-G. Park. Giant magnetoelastic coupling in multiferroic hexagonal manganites. *Nature*, 451:805–808, 2008.

[49] M. Tomczyk, A. M. Senos, P. M. Vilarinho, and I. M. Reaney. Origin of microcracking in $\mathrm{YMnO_3}$ ceramics. *Scr. Mater.*, 66:288–291, 2012.

[50] C. Moure, M. Villegas, J. F. Fernandez, J. Tartaj, and P. Duran. Phase transition and electrical conductivity in the system $\mathrm{YMnO_3}$-$\mathrm{CaMnO_3}$. *J. Mater. Sci.*, 34:2565–2568, 1999.

[51] O. Pen, D. Gutie, and P. Dura. Crystalline structure and electrical properties of $\mathrm{YCu}_x\mathrm{Mn}_{1-x}\ \mathrm{O_3}$ solid solutions. 22:2939–2944, 2002.

[52] S. C. Chae. Domain patterns and electric properties at domain walls in a surface normal to the direction of ferroelectric polarization in h-$\mathrm{ErMnO_3}$. *J. Korean Phys. Soc.*, 66:1381, 2015.

[53] Y. Du, X. L. Wang, D. P. Chen, S. X. Dou, Z. X. Cheng, M. Higgins, G. Wallace, and J. Y. Wang. Domain wall conductivity in oxygen deficient multiferroic $\mathrm{YMnO_3}$ single crystals. *Appl. Phys. Lett.*, 99, 2011.

[54] P. Ren, H. Fan, and X. Wang. Bulk conduction and nonlinear behaviour in multiferroic $\mathrm{YMnO_3}$. *Appl. Phys. Lett.*, 103, 2013.

[55] T. Choi, Y. Horibe, H. T. Yi, Y. J. Choi, W. Wu, and S.-W. Cheong. Insulating interlocked ferroelectric and structural antiphase domain walls in multiferroic $YMnO_3$. *Nat. Mater.*, 9:253–8, 2010.

[56] M. Tomczyk, P. M. Vilarinho, A. Moreira, and A. Almeida. High temperature dielectric properties of $YMnO_3$ ceramics. *J. Appl. Phys.*, 110:0–5, 2011.

[57] U. Adem, N. Mufti, A. A. Nugroho, G. Catalan, B. Noheda, and T. T. M. Palstra. Dielectric relaxation in $YMnO_3$ single crystals. *J. Alloys Compd.*, 638:228–232, 2015.

[58] C. Balamurugan and D.-W. Lee. Perovskite hexagonal $YMnO_3$ nanopowder as p-type semiconductor gas sensor for H_2S detection. *Sensors Actuators B Chem.*, 221:857–866, 2015.

[59] W. S. Choi, D. G. Kim, S. S. a. Seo, S. J. Moon, D. Lee, J. H. Lee, H. S. Lee, D.-Y. Cho, Y. S. Lee, P. Murugavel, J. Yu, and T. W. Noh. Electronic structures of hexagonal $RMnO_3$ (R = Gd, Tb, Dy, and Ho) thin films: Optical spectroscopy and first-principles calculations. *Phys. Rev. B*, 77:045137, 2008.

[60] J. E. Medvedeva, V. I. Anisimov, M. A. Korotin, O. N. Mryasov, and A. J. Freeman. The effect of Coulomb correlation and magnetic ordering on the electronic structure of two hexagonal phases of ferroelectromagnetic $YMnO_3$. *J. Phys. Condens. Matter*, 12:4947–4958, 2000.

[61] D. Richerson, D. W. Richerson, and W. E. Lee. *Modern ceramic engineering: properties, processing, and use in design*. CRC press, Boca Raton, 2005.

[62] G. S. Pawley. Unit-cell refinement from powder diffraction scans. *J. Appl. Crystallogr.*, 14(6):357–361, 1981.

[63] C. Bréchignac, P. Houdy, and M. Lahmani. *Nanomaterials and Nanochemistry*. Springer Science and Business Media, 2008.

[64] D. Småbråten, N. H. Gaukås, S. Skjærvø, S. P. Singh, D. Meyer, and S. M. Selbach. Tailoring n- and p-type conductivity in donor and acceptor doped $YMnO_3$ (unpublished). 2016.

Appendix A

Synthesis of 150 nm h−$YMnO_3$

The synthesis route for 150 nm-sized h−$YMnO_3$ by Bergum [32] is based on maleic acid as gelling agent instead of citric acid. The synthesis route also uses metal nitrates as cation precursors, forming an oxidizing environment upon heat treatment. The 150 nm h−$YMnO_3$ is only used once in this study, and the powder might as well be synthesized from the citric acid sol-gel route described in Experimental Work. This synthesis route is not emphasized in this study as it is not very important, hence the placement in the appendices.

The precursor solution was prepared by mixing stoichiometric amounts of $Mn(NO_3)_2$ in distilled water with Y_2O_3 (Hermann C. Starck) in 1 M nitric acid. The solution was then mixed with maleic acid (MA) and ethylene glycol (EG) in a molar ratio cations : MA : EG of 1 : 1.1 : 1.1. The solution was heated on a hotplate at 150 °C until gelling. The formed gel was dried at 250 °C for 3 hours, slowly heated to 400 °C and held for 6 hours until a raw powder was formed. The raw powders was finally annealed in air at 1100 °C for 12 hours, forming a crystalline powder with crystallite size around 150 nm.

A list of all the chemicals used is given in Table A.1, and the heat treatment is summarized in Table A.2. A schematic overview of the sol-gel synthesis is given in Figure A.1.

Table A.1: List with information of all the chemicals used to prepare 150 nm-sized h−$YMnO_3$ by the maleic acid sol-gel synthesis.

Chemical	Molecular formula	Purity	Manufactory
Ethylene glycol	$C_4H_6O_2$	99 vol%	Merck
Maleic acid	$C_4H_4O_4$	>99 wt%	Merck
Manganese(II) nitrate	$Mn(NO_3)_2$	>98.5 wt%	Merck
Nitric acid	HNO_3	1 M	Merck
Yttrium(III) oxide	Y_2O_3	-	Hermann C. Starck

Table A.2: Heat treatment of wet gel, dry gel and calcined raw powder to form 150 nm-sized h−$YMnO_3$.

h−$RMnO_3$	Drying of gel	Calcination of gel	Annealing
150 nm h−$YMnO_3$	250 °C, 3 h	400 °C, 6 h	1100 °C, 12 h

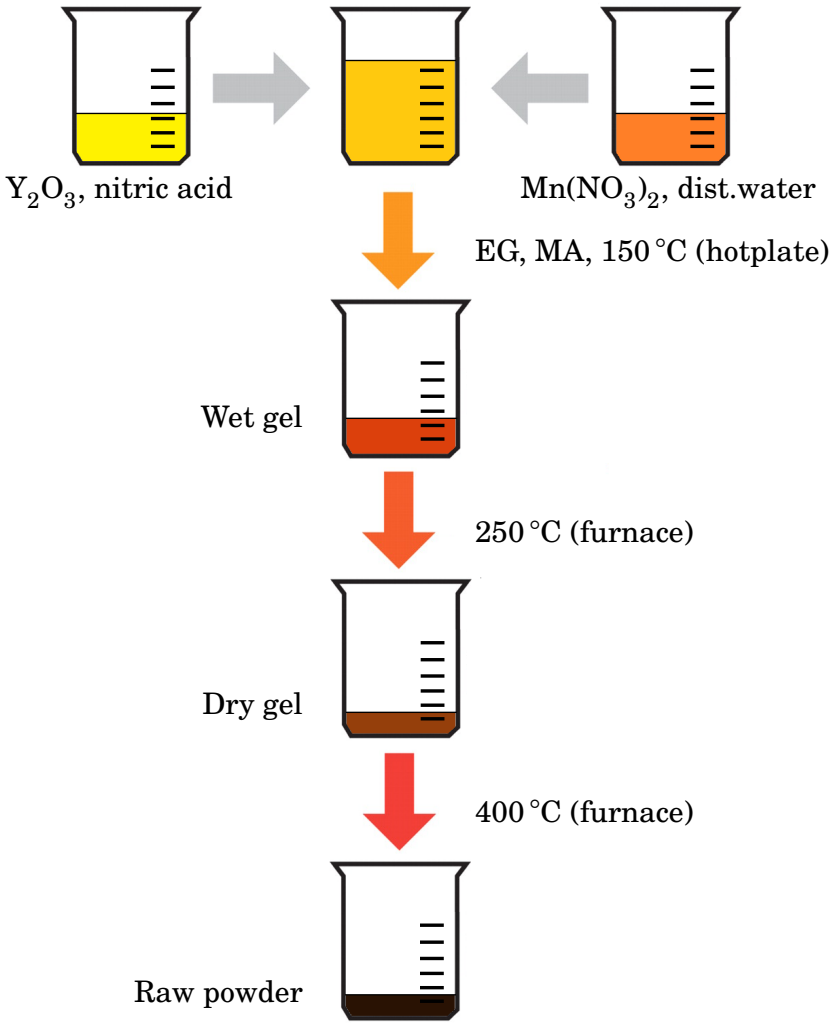

Figure A.1: Schematic overview of the maleic acid sol-gel synthesis route. Stoichiometric amounts of metal ion precursors dissolved with maleic acid in distilled water were mixed with ethylene glycol, and then heated on a hotplate at 150 °C until gelling. The gel was then dried at 250 °C, and further calcined at 400 °C to form an amorphous raw powder.

Appendix B

SEM Imaging of Bulk Powders

The crystallite sizes in bulk-sized h$-YMnO_3$ powder and bulk-sized h$-YMn_{0.85}Ti_{0.15}O_3$ powder was determined by SE-SEM imaging. Figure B.1 and B.2 show SEM images of h$-YMnO_3$ and h$-YMn_{0.85}Ti_{0.15}O_3$, respectively. Many images of each powder were evaluated, and the images in Figure B.1 and B.2 are chosen based on best possible representation of the powders. Table B.1 shows the parameters used in the imaging.

Table B.1: Parameters used in the SEM imaging.

Setting	h$-YMnO_3$	h$-YMn_{0.85}Ti_{0.15}O_3$
SEM type	Hitachi S-3400	Hitachi S-3400
Signal carrier	Secondary electrons (SE)	Secondary electrons (SE)
Sample base	Carbon tape	Carbon tape
Sputtering material	Carbon	Carbon
Acceleration voltage	15 kV	15 kV
Probe current	40 nA	40 nA
Magnification	x2.10k	x2.30k

Other than stating the crystallite sizes and crystallite size distribution for reproducibility, the information from the SEM imaging was used to determine sintering program for the square prisms prepared for the electrochemical measurements.

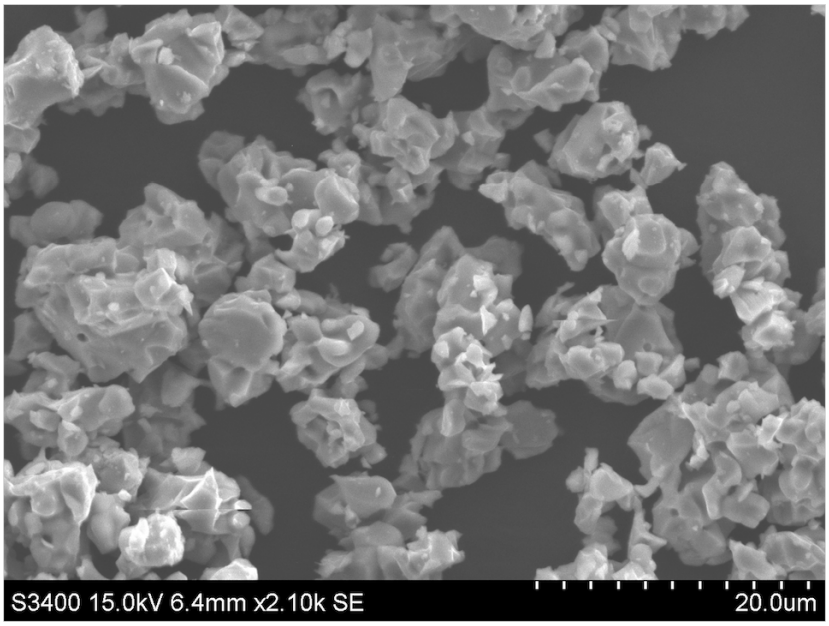

Figure B.1: SEM image of bulk-sized h−$YMnO_3$ powder. The crystallite size ranges from 2 µm to 14 µm. The image is captured using an acceleration voltage of 15 kV and a probe current of 40 µA.

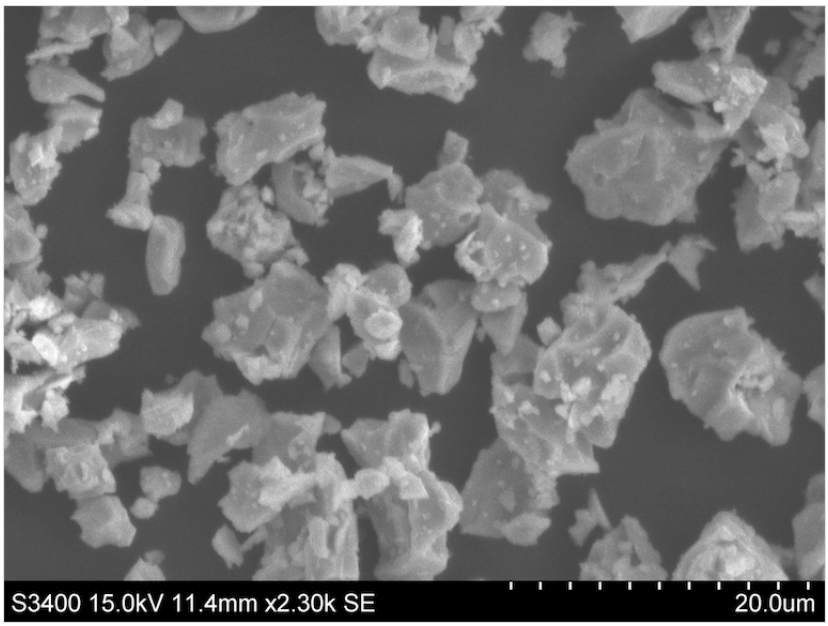

Figure B.2: SEM image of bulk-sized h−$YMn_{0.85}Ti_{0.15}O_3$ powder. The crystallite size ranges from 2 µm to 17 µm. The image is captured using an acceleration voltage of 15 kV and a probe current of 40 µA.

Appendix C

HT-XRD Plots

The calculated lattice parameters from the HT-XRD measurements are plotted as a function of temperature as c/a in Figure C.1 and as the unit cell volume in Figure C.2. Equation 2.1 was used to calculate the unit cell volume from the lattice parameters. Both figures includes values from measurements in O_2 and N_2. In the figures, H1 indicates the first heating, C1 the first cooling and H2 the second heating of the powders.

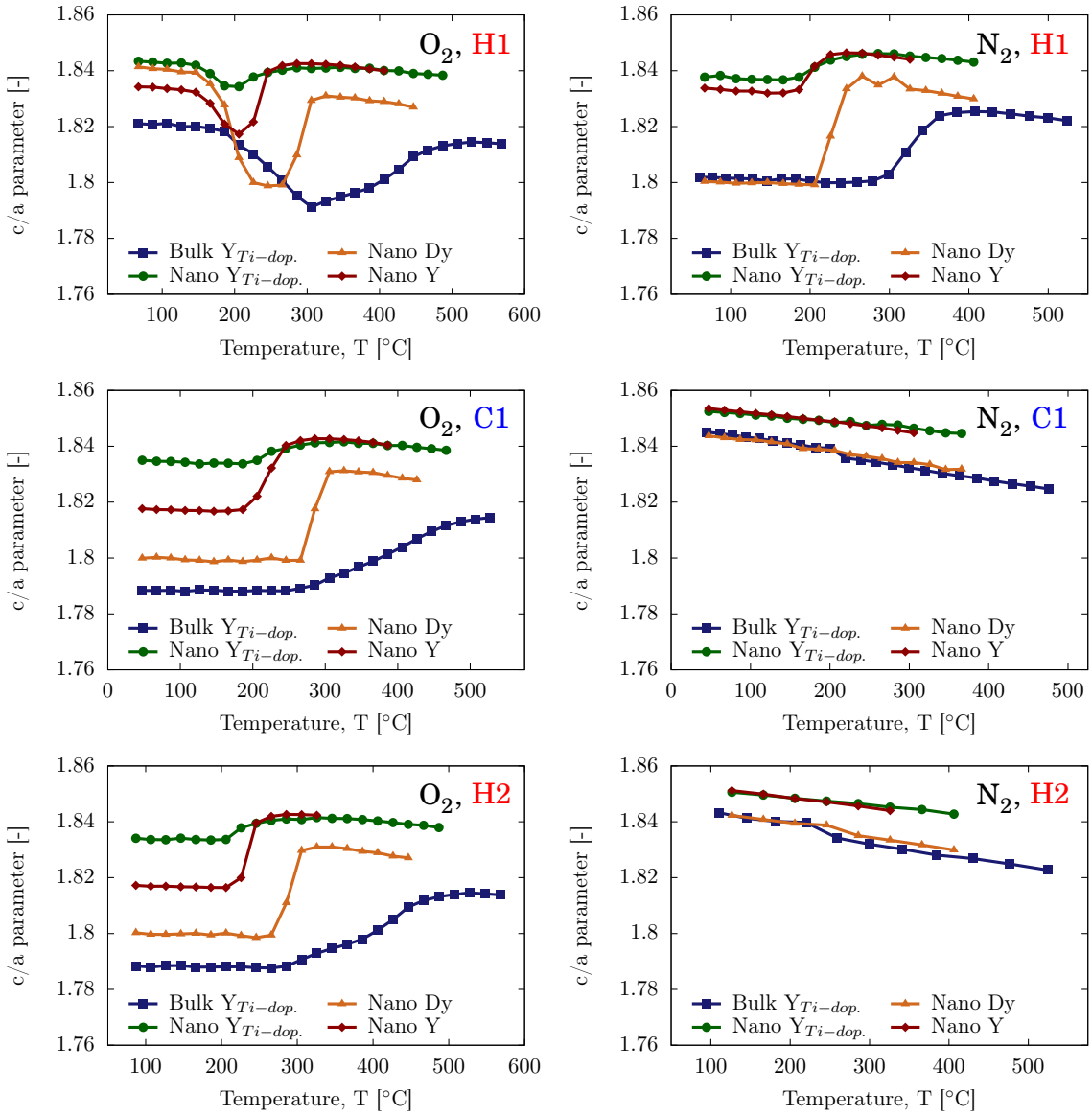

Figure C.1: HT-XRD measurements of c/a from heating and cooling in O_2 and N_2. The top row represents heating 1 (H1), the middle row cooling 1 (C1), and the bottom row is from heating 2 (H2). The left column includes values measured in O_2, while the right column includes values measured in N_2.

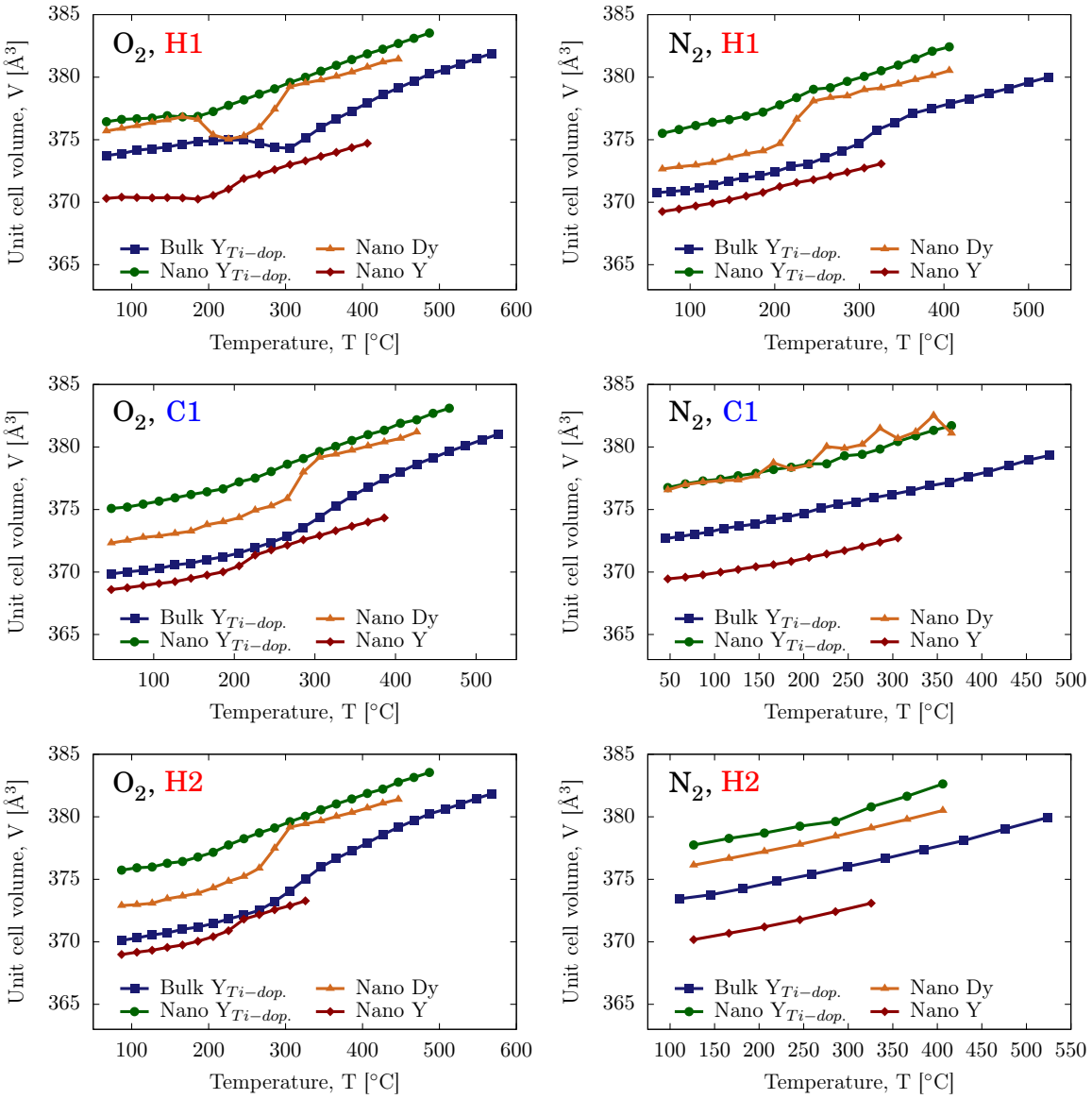

Figure C.2: HT-XRD measurements of unit cell volume, V, from heating and cooling in O_2 and N_2. The top row represents heating 1 (H1), the middle row cooling 1 (C1), and the bottom row is from heating 2 (H2). The left column includes values measured in O_2, while the right column includes values measured in N_2.

Appendix D

DC Conductivity Plots

Figure D.1-D.3 show the measured DC conductivity as a function of time and temperature, slightly different presented than in Figure 4.12.

In Figure D.1, the DC conductivity is plotted as a function of time. Since the heating and cooling rate were equal, this plot is an "unfolded" version of Figure 4.12, better differentiating the oxidation/reduction areas upon heating and cooling.

Figure D.2 and D.3 are the same plots as Figure 4.12 and D.1, respectively, with linear instead of logarithmic y-axes. From these figures it is clear the the effect of O_2 exchange on the conductivity is weak compared to the thermal effect. The data in these figures are also plotted with two y-axes, where the conductivity for $h-YMnO_3$ is scaled by the left y-axes, and the conductivity for $h-YMn_{0.85}Ti_{0.15}O_3$ is scaled by the right y-axes.

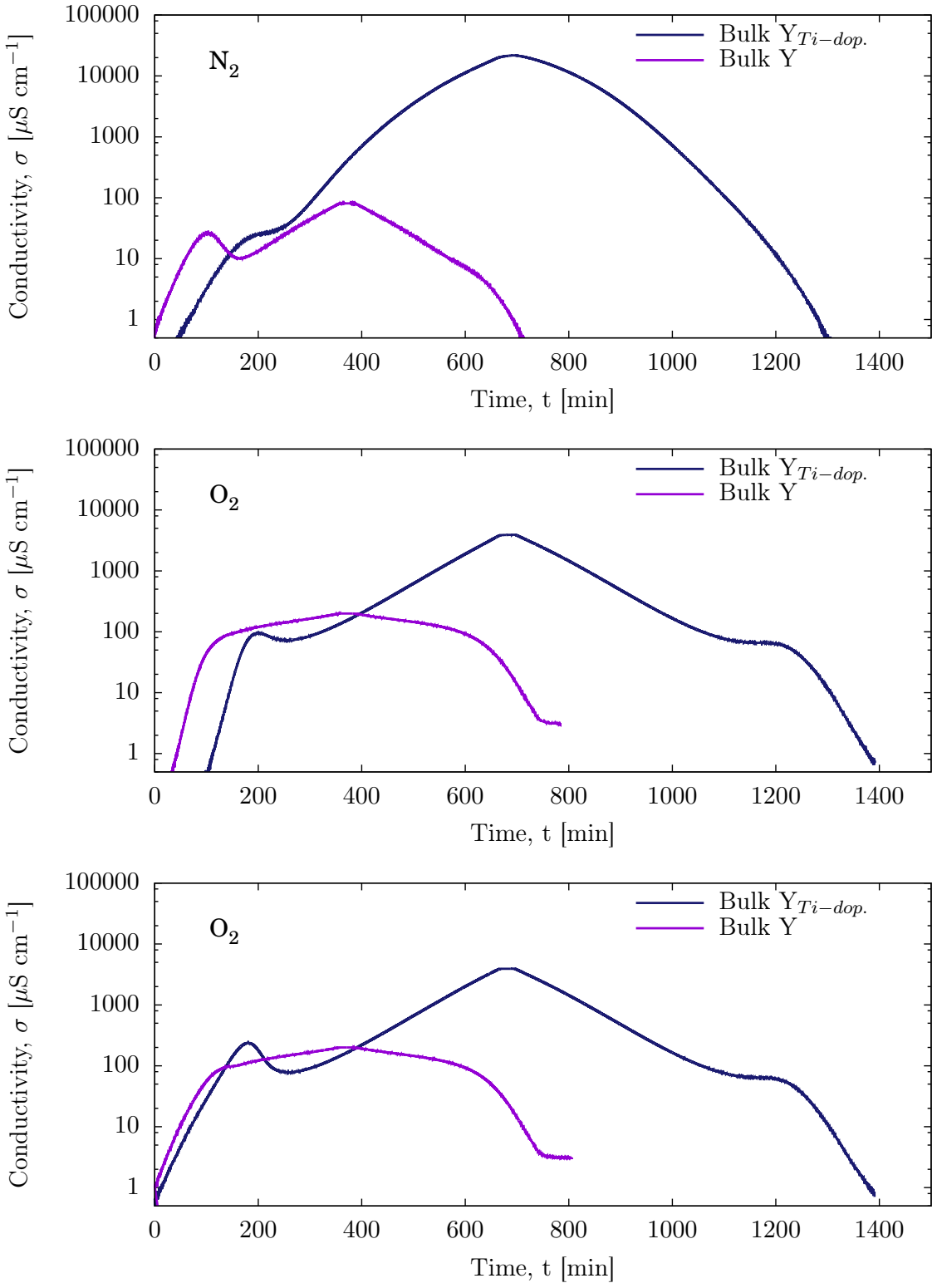

Figure D.1: Conductivity during heating and cooling in N_2 (top) and O_2 (center and bottom) as a function of time.

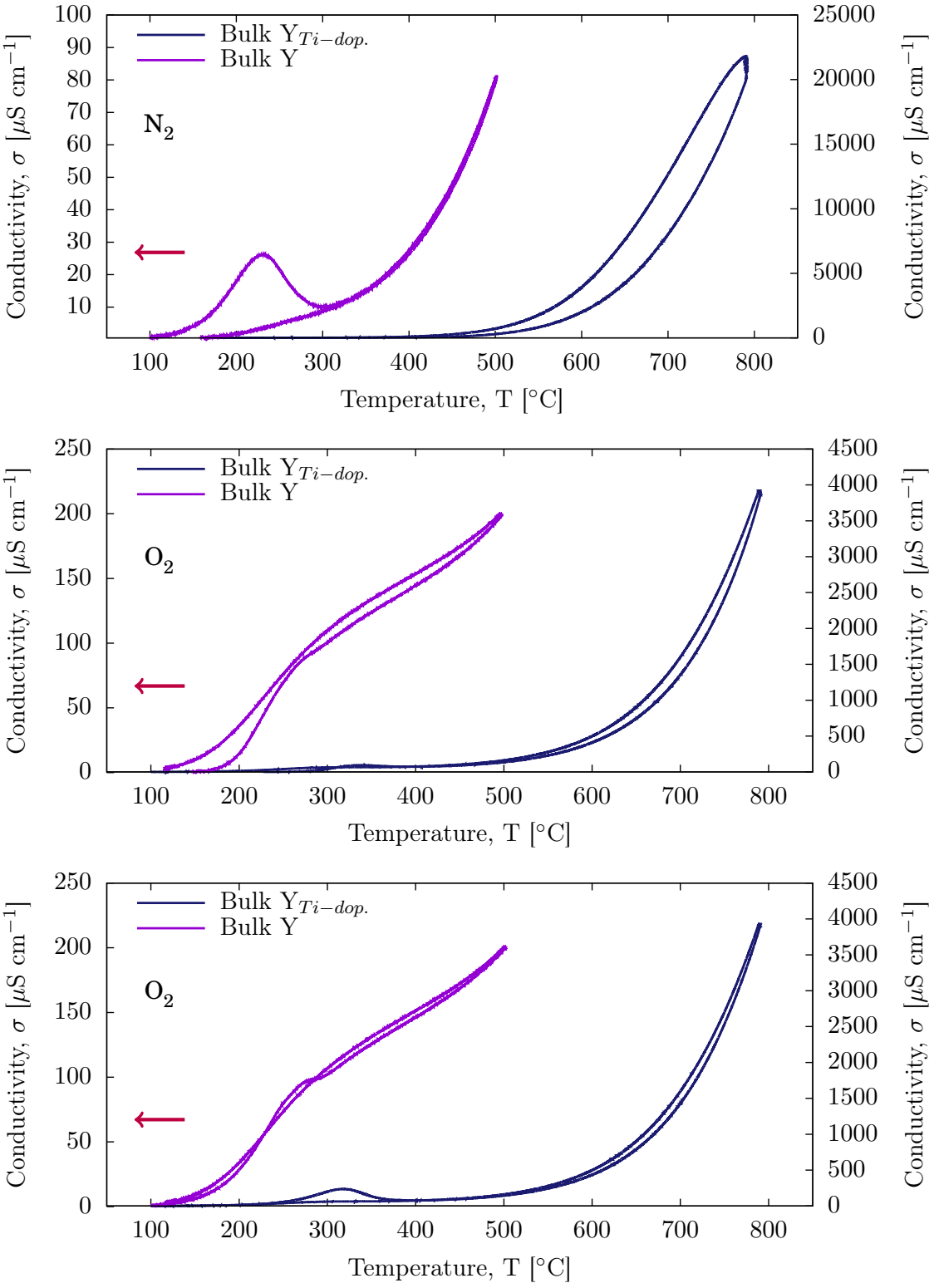

Figure D.2: Conductivity during heating and cooling in N_2 (top) and O_2 (center and bottom) as a function of temperature. The axes are linearly scaled. The measurements for Bulk Y scale with the left y-axes, while the measurements for Bulk Ti scale with the right y-axes.

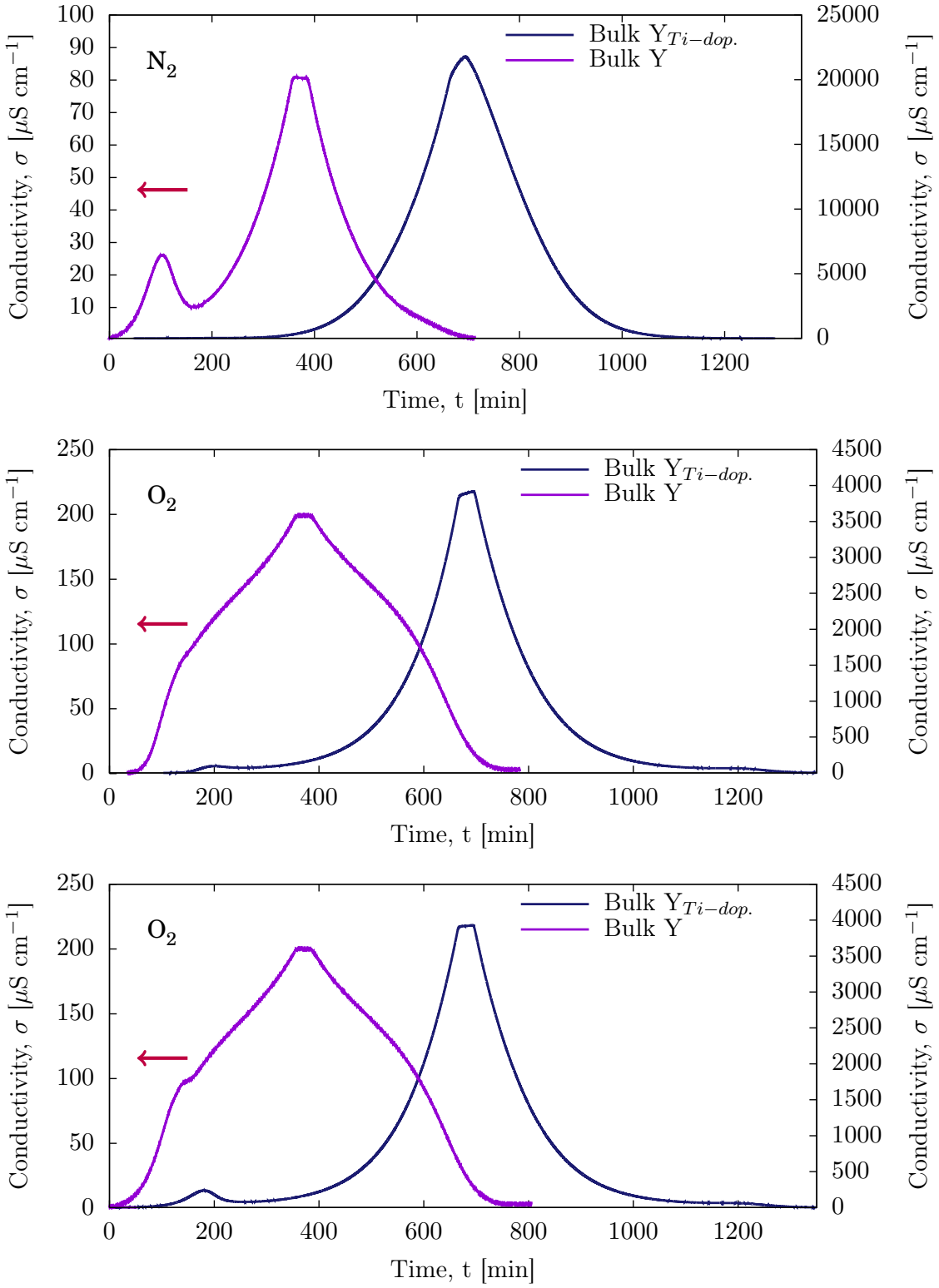

Figure D.3: Conductivity during heating and cooling in N_2 (top) and O_2 (center and bottom) as a function of time. The axes are linearly scaled. The measurements for Bulk Y scale with the left y-axes, while the measurements for Bulk Ti scale with the right y-axes.

Appendix E

Combinational Plots

The measuring techniques used in this study look at the change in different material properties, all caused by the same phenomenon, i.e. oxygen absorption/desorption. Thus, combining the measurements can reveal if the properties are changed simultaneously or not, and if any of the measurements have a broader temperature region of affection that can be seen from just one of the changing properties.

E.1 DC Conductivity and TGA

Both the DC-conductivity and the mass change during heating and cooling in O_2 were measured on bulk-sized h$-YMn_{0.85}Ti_{0.15}O_3$. Figure E.1 gives combinational plots for these properties during heating and cooling.

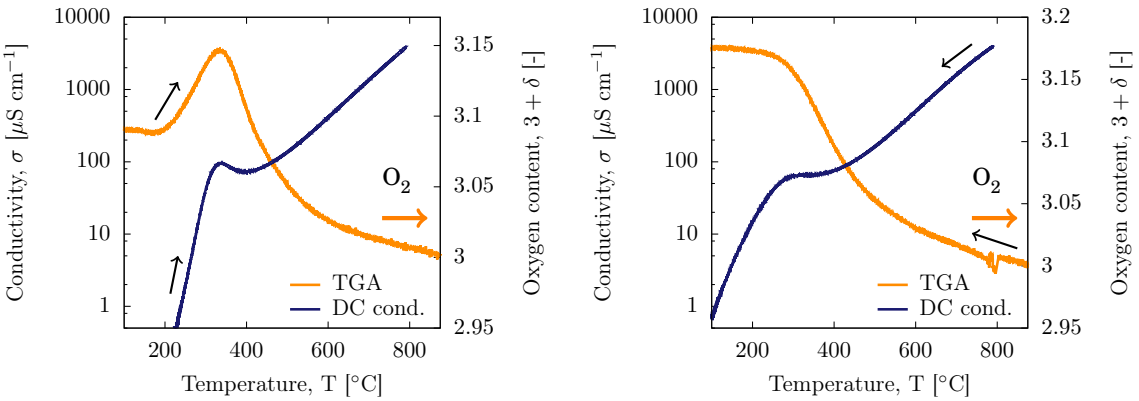

Figure E.1: Change in DC conductivity and mass during heating (left) and cooling (right) in O_2 for bulk-sized h$-YMn_{0.85}Ti_{0.15}O_3$. The TGA measurements (mass change) is plotted in orange and scale with the right y-axes, while the DC conductivity is plotted in dark blue.

The change in mass correspond well to the changes in DC conductivity, and both mea-

surements suggest an oxygen absorption peak at around 325 °C in O_2. The broad temperature region of absorption/desorption is much clearer in the TGA measurements than the DC conductivity measurements.

E.2 DC Conductivity and HT-XRD

DC conductivity measurements and HT-XRD measurements of the lattice parameters a and c were both conducted during heating and cooling in O_2 and N_2 of bulk-sized h−$YMn_{0.85}Ti_{0.15}O_3$. Figure E.2 gives combinational plots for these properties. An important thing to note is that the HT-XRD measurements were first conducted in O_2, then in N_2, while the order was opposite in the DC conductivity measurements.

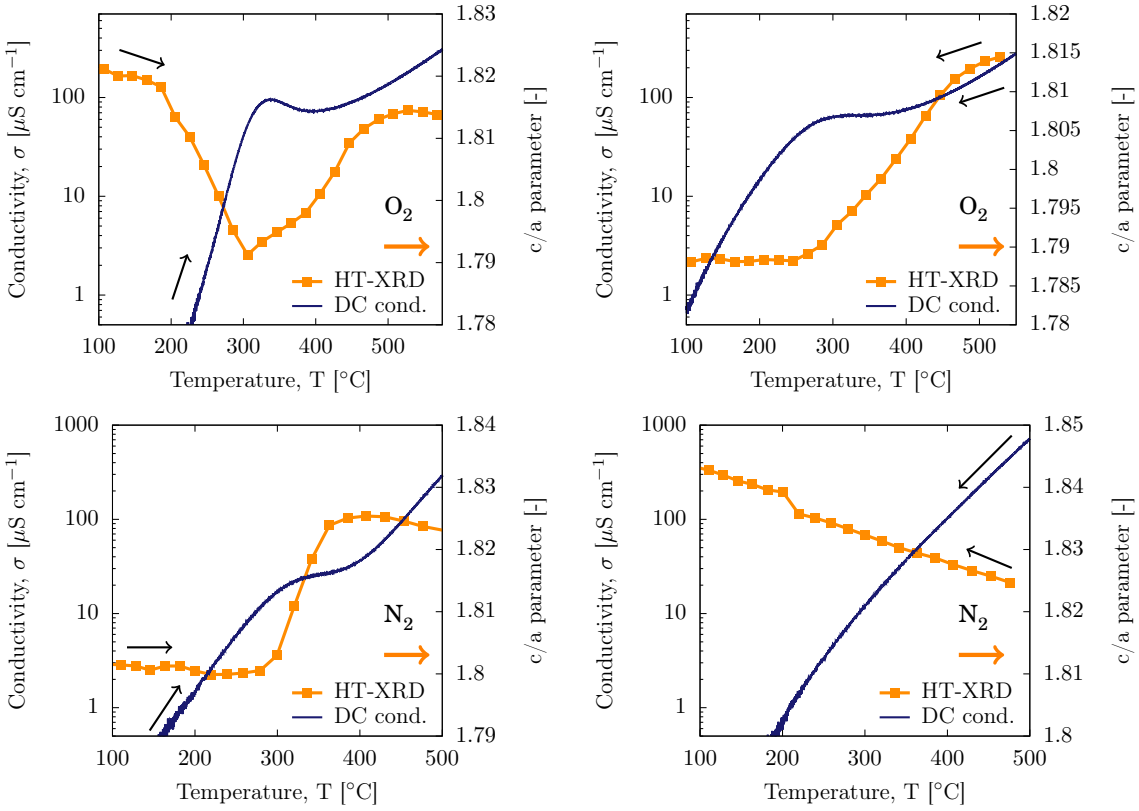

Figure E.2: Change in DC conductivity and lattice parameter ratio c/a during heating (left) and cooling (right) in O_2 (top) and N_2 (bottom) for bulk-sized h−$YMn_{0.85}Ti_{0.15}O_3$. The HT-XRD measurements (c/a ratio) is plotted in orange and scale with the right y-axes, while the DC conductivity is plotted in dark blue.

E.3 HT-XRD and TGA

HT-XRD measurements and TGA measurements for bulk- and nano-sized Ti-doped h−$YMnO_3$ (h−$YMn_{0.85}Ti_{0.15}O_3$), nano-sized $DyMnO_3$ and nano-sized $YMnO_3$ during heating and cooling in O_2 are given in Figure E.3 and E.4. Figure E.3 shows plots of these measurements during heating, and Figure E.4 shows plots of the measurements during cooling. The change in the two properties does not match very well in terms of temperature, suggesting that either one of the measurements are not temperature corrected properly, or that there is a delay for one of these properties in terms of onset temperature.

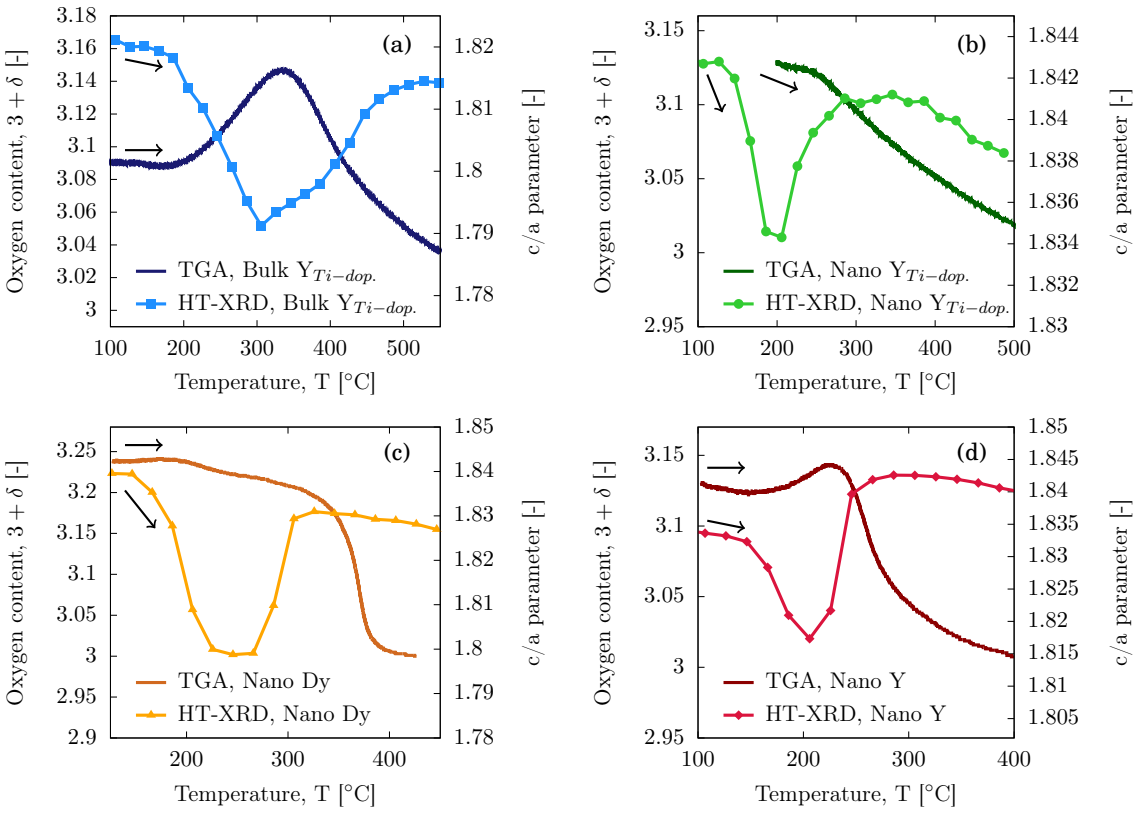

Figure E.3: Change in mass and lattice parameter ratio c/a during heating in O_2 for (a) bulk-sized h−$YMn_{0.85}Ti_{0.15}O_3$, (b) nano-sized h−$YMn_{0.85}Ti_{0.15}O_3$, (c) nano-sized $DyMnO_3$ and (d) nano-sized $YMnO_3$. The HT-XRD data (c/a ratio) scale with the right y-axes.

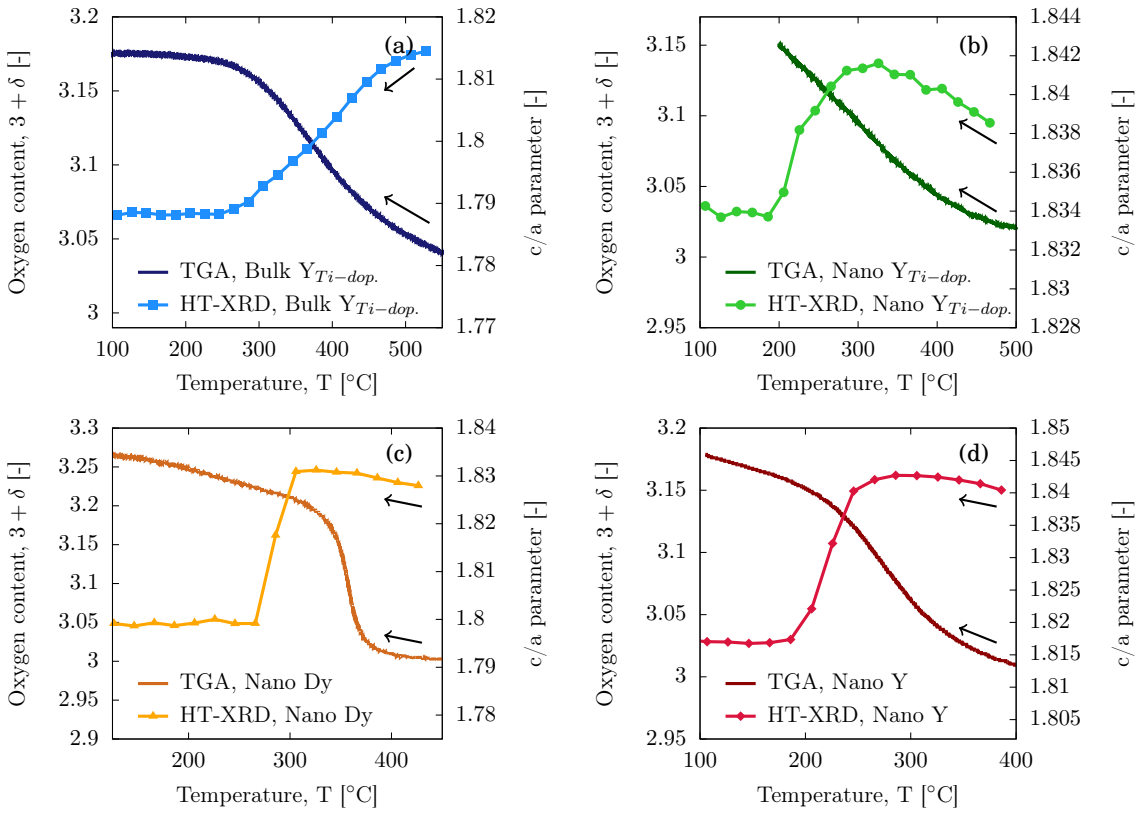

Figure E.4: Change in mass and lattice parameter ratio c/a during cooling in O_2 for (a) bulk-sized h−$YMn_{0.85}Ti_{0.15}O_3$, (b) nano-sized h−$YMn_{0.85}Ti_{0.15}O_3$, (c) nano-sized $DyMnO_3$ and (d) nano-sized $YMnO_3$. The HT-XRD data (c/a ratio) scale with the right y-axes.

Appendix F

Annealing of Nano-sized h−$RMnO_3$

The nano-sized h−$YMn_{0.85}Ti_{0.15}O_3$ and h−$YMnO_3$ powders used in the study was annealed in two sequences to coarsen the crystallites. In the first treatment, 1 hour at 900 °C was tried. For the second treatment, 3 hours at 900 °C was used to initiate further growth. Both annealing programs were carried out in air. Figure F.1 shows the two temperature programs.

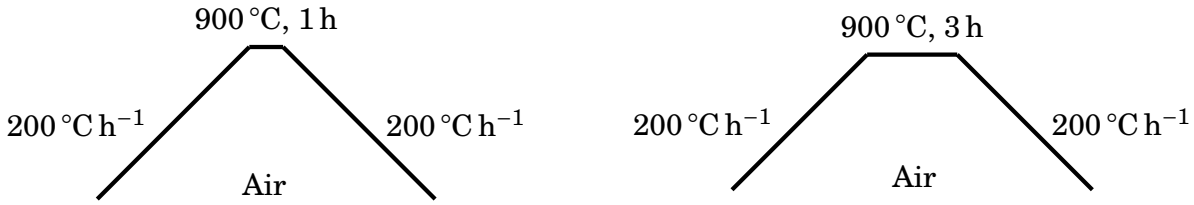

(a) First annealing.

(b) Second annealing.

Figure F.1: (a) The first temperature program for annealing nano-sized h−$YMn_{0.85}Ti_{0.15}O_3$ and h−$YMnO_3$. (b) The second temperature program for annealing nano-sized h−$YMn_{0.85}Ti_{0.15}O_3$ and h−$YMnO_3$. The programs were subsequently used on the same powder, i.e. the same powders were annealed twice.

The coarsening of the heat treated powders were studied using XRD, see Figure F.2. Rietveld refinement were then used to find the crystallite sizes of the powders, see Table F.1. Plots showing the crystallite size development in nanometers for each material are also included in Figure F.2.

Table F.1: Crystallite sizes of nano-sized h−$YMn_{0.85}Ti_{0.15}O_3$ and nano-sized h−$YMnO_3$.

Treatment	Cryst.size nano Ti [nm]	Cryst.size nano Y [nm]
Initially	18.7	25.5
First annealing	30.4	32.7
Second annealing	33.8	35.9

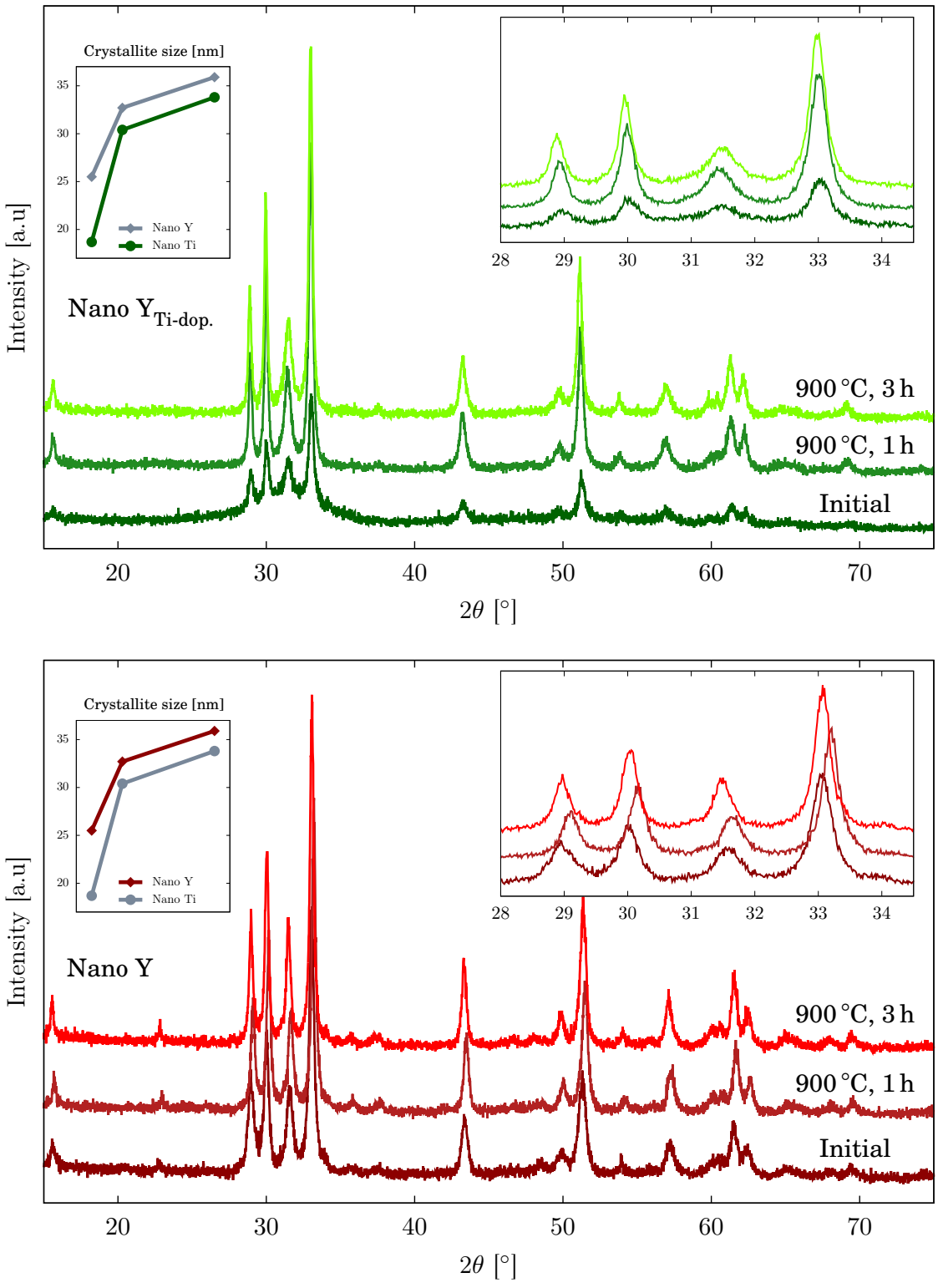

Figure F.2: X-ray diffractogram of nano-sized h−$YMn_{0.85}Ti_{0.15}O_3$ (top) and h−$YMnO_3$ (bottom) after consecutive annealing programs. The plots in the upper, right corners show a narrower 2θ region. The plots in the upper, left corners show the crystallite size development in nanometers.

Appendix G

DFT Calculations

Unpublished DFT calculations on h$-YMnO_3$ and 4.167% Ti-doped h$-YMnO_3$ were conducted at the department by Småbråten *et. al* [64], using the PAW method implemented with VASP. In the calculations a 2x2x1 supercell was used with 120 atoms. In the case of Ti-doped h$-YMnO_3$, 1/24 (4.167%) of Mn ions were substituted with Ti. Among the calculations, the DOS of the aforementioned materials were calculated, see Figure G.1-G.3.

In Figure G.1 the DOS of stoichiometric h$-YMnO_3$ are given. No states overlap with the Fermi level, E_F, giving pure h$-YMnO_3$ the semiconducting properties with a band gap of 1.6 eV.

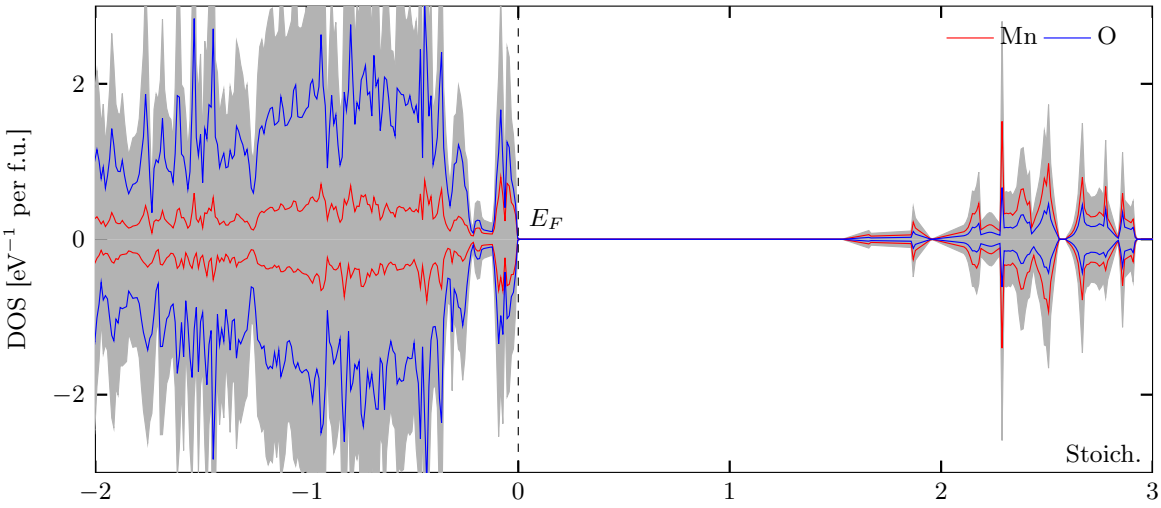

Figure G.1: Density of states (DOS) of stoichiometric h$-YMnO_3$. The dotted line marks the Fermi level. The calculations are done with VASP, using the implemented PAW method, and are conducted by Småbråten *et. al* [64].

In Figure G.2 the DOS of pure h−$YMnO_3$ with 4.167% Ti-doping are given. In addition to a lowering of the states relative to the Fermi level, E_F, compared with stoichiometric h−$YMnO_3$, some contributions from the $3d$ orbitals of Ti^{4+} is observed. However, the states of the $3d$ orbitals from Ti^{4+} are too high in energy to affect the Fermi level and thus the conductivity.

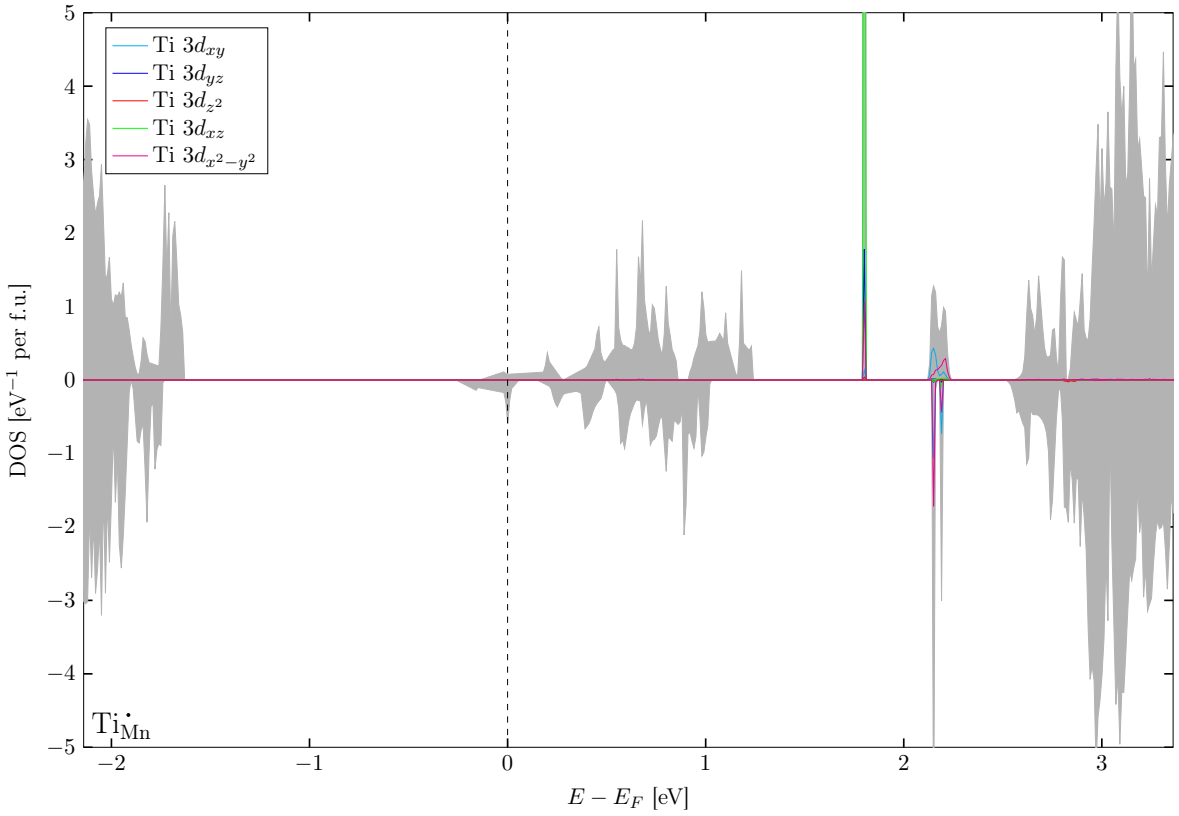

Figure G.2: Density of states (DOS) of pure h−$YMnO_3$ with 4.167% Ti-doping. The dotted line marks the Fermi level. The calculations are done with VASP, using the implemented PAW method, and are conducted by Småbråten *et. al* [64].

In Figure G.3 the DOS of h−$YMnO_{73/24}$ with 4.167% Ti-doping and one interstitial oxygen are given. Compared with the pure Ti-doped h−$YMnO_3$, the states have increased relative to the Fermi level, E_F. The grey states at the Fermi level are contributions from the interstitial oxygen.

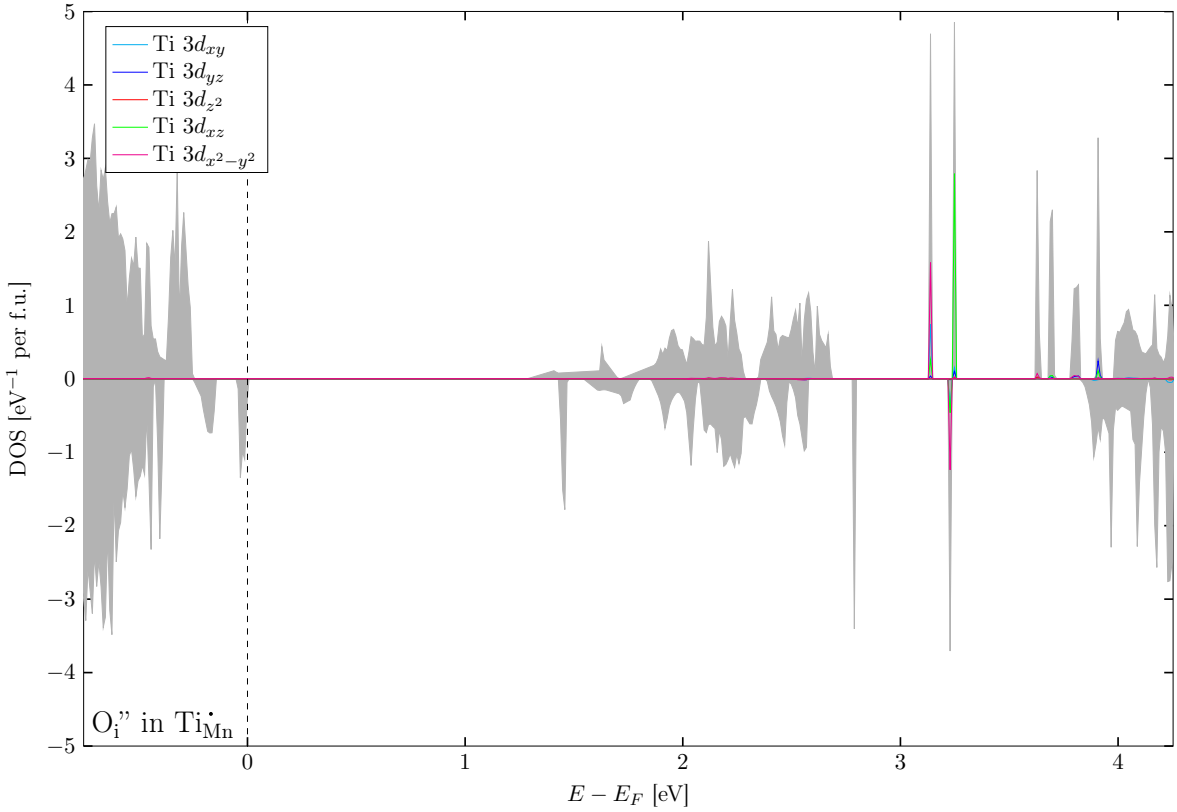

Figure G.3: Density of states (DOS) of h−$YMnO_3$ with 4.167% Ti-doping and one interstitial oxygen. The dotted line marks the Fermi level. The calculations are done with VASP, using the implemented PAW method, and are conducted by Småbråten *et. al* [64].